Norges miljø- og
biovitenskapelige
universitet

Master's Thesis 2016
30 credits
Department of Mathematical Sciences and Technology

Nordic Irradiance Conditions and the Effects on Solar Module Efficiency

Tobias Aasprong Brekke
Environmental Physics and Renewable Energy

Acknowledgments

I want to thank everybody who helped me during this exciting process.

First of all, I want to thank Dr. Josefine Helene Selj, my supervisor at IFE, for dedicated and excellent guidance throughout this semester. Josefine contributed with good advice and were always there to point me in the right direction. Her knowledge in physics, photovoltaic technologies and measurement techniques was invaluable. Further I want to thank Dr. Espen Olsen, my supervisor at NMBU, for valuable advice.

I also want to thank Dr. Anne Gerd Imenes at TEKNOVA, for guidance concerning the modelling of the solar spectrum and her knowledge in atmospherical physics. Dr. Georgi Hristov Yordanov and Dr. Anne Gerd Imenes are to be thanked for aiding me in the measurements performed in Grimstad.

I want to thank Arne Auen Grimnes and Signe Kroken at NMBU for their contribution concerning the data collected from the measurement site at Ås.

I want to thank Lenny Enstrom at IFE for contributing with his experience and practical knowledge in the establishment and implementation of the measurement site at Kjeller. I am also grateful to Bent Thomassen for several times helping me move the measurement equipment up and down from the measurement site.

I am also thankful for having the chance to work in the same building as the great scientists that work at IFE, and for getting to learn more about the different research fields within the photovoltaic industry.

At last I want to thank my girlfriend, family and friends for your support, and laughs, throughout this semester.

Kjeller, May 10 2016

Tobias Aasprong Brekke

Abstract

The purpose of this study is to characterize Nordic irradiance conditions and the effects on solar module efficiency. As of 2015, approximately 1.3 % of the world's electrical energy production is covered by photovoltaics, which is a technology that will play a large part in the future power market. The rapid growth of electrical solar energy is also taking place in the Nordics, and hence there is a growing interest in the performance of photovoltaic systems under Nordic climate and insolation conditions.

The high latitudes of the Nordic countries significantly affect both the intensity and the spectral distribution of the solar irradiation. Furthermore, it is well known that variations in the light intensity and solar spectrum give rise to technology dependent changes in the solar cell efficiency. This work aims to study the insolation conditions in the eastern and southern part of Norway and the resulting quantitative effects on two different solar cell technologies, p-Si and CIS.

Global horizontal irradiance data obtained from the measurement station at Ås (NMBU) in the period 2011-2015 was used to study the relative energy contribution at different intensity levels.

There is previously little precise data on the spectrally resolved irradiation data in Norway. Spectral irradiance is measured at some measuring stations in Norway, but only for specific wavelength intervals which results in a coarse spectral resolution. In this work measurements of spectral irradiance are performed using a spectroradiometer at two locations, Kjeller and Grimstad. The SMARTS modelling tool has been used to compliment the measured data.

The highest relative energy contribution occurs at 400-500 W/m^2, contributing with 14 % of the yearly irradiation. The relative energy contribution is homogeneously distributed at low and medium intensities, but is drastically decreased after 800 W/m^2. Irradiance levels ranging between 800-1100 W/m^2 only contribute with 4 % of the yearly irradiation. The average relative efficiencies of the CIS- and p-Si modules at light intensities 400-500 W/m^2, with respect to the STC efficiency of each module, are 0.9978 and 0.9987, respectively.

The measured sola spectra were characterized by a red richness, which was expected due to an overall high air mass. By analyzing the correlation between average photon energy and the spectral factor, it showed that the p-Si module performs better in red rich spectra compared to the CIS module which appears to perform better in blue rich spectra.

Finding data concerning the aerosol- and gaseous composition of the atmosphere around Kjeller and Grimstad was a key element in establishing accurate input values to implement in SMARTS. Due to lack of atmospheric data, several parameters in SMARTS were varied in order to be able to compare measured and modelled spectra.

Sammendrag

Formålet med denne masteroppgaven er å karakterisere innstrålingsforholdene i Norden og på hvilken måte disse forholdene påvirker effektiviteten til fotovoltaiske solcellemoduler. Omkring 1,3 % av verdens elektrisitetsproduksjon er produsert fra solcellemoduler, som er en teknologi som kommer til å spille en stor rolle i fremtidens kraftmarked. Den raske veksten av elektrisitet produsert fra fotovoltaiske teknologier skjer også i Norden, og det er derfor er økende interesse angående ytelsen til fotovoltaiske systemer i et nordisk klima, med varierende innstrålingsforhold.

De høye lengdegradene til de nordiske landene påvirker både intensiteten og den spektrale distribusjonen til den solinnstrålingen. Det er kjent at varierende lysintensitet og solspektrum påvirker effektiviteten til forskjellige solcelleteknologier. Dette prosjektet fokuserer på å undersøke innstrålingsforholdene i de sørlige og østlige delene av Norge, og hvordan disse forholdene påvirker effektiviteten til de to forskjellige solcelleteknologiene p-Si og CIS.

Global innstrålingsdata, på en horisontal flate, målt ved målestasjonen på Ås (NMBU) i perioden 2011-2015 ble benyttet til å analysere det relative energibidraget ved forskjellige lysintensiteter.

Det er tidligere blitt utøvd lite målinger på den spektrale innstrålingsdistribusjonen i Norge. Spektralt oppløste målinger utføres ved noen målestasjoner i Norge, men bare for spesifikke bølgelengdeintervaller, noe som resulterer i grove målinger. I denne oppgaven er solspektrumet målt med et spektroradiometer ved to lokasjoner, Kjeller og Grimstad. Modelleringsverktøyet SMARTS er også blitt benyttet for å komplementere de målte dataene.

Det høyeste relative energibidraget oppnås ved innstrålingsnivåer mellom 400-500 W/m^2, som bidrar med 14 % av den innstrålte energien. Det relative energibidraget er homogent fordelt ved lave og middels intensiteter, men det relative bidraget er drastisk redusert etter 800 W/m^2. Innstråling med intensiteter mellom 800-1100 W/m^2 bidrar bare med 4 % av den årlig innstrålte energien. De gjennomsnittlige relative virkningsgradene til CIS- og p-Si modulene, ved lysintensitetene 400-500 W/m^2 og sett i forhold til STC effektiviteten til hver modul, er henholdsvis 0,9978 og 0,9987.

De målte solspektrene var forskjøvet mot den røde delen av spekteret, noe som var forventet på grunn av en generelt høye luftmassen. Ved å analysere sammenhengen mellom gjennomsnittlig fotonenergi og spektral faktor, viste det seg at p-Si modulen yter bedre i rødforskjøvet spektra i forhold til CIS modulen som viste seg å yte bedre i blåforskjøvet spektra.

Innhenting av data vedrørende aerosol- og gass-sammensetningen av atmosfæren rundt Kjeller og Grimstad var en sentral del av arbeidet som måtte utføres for å etablere nøyaktige inngangsverdier til å brukes i SMARTS. På grunn av mangel på atmosfæriske data, ble flere parametere i SMARTS variert for å kunne sammenligne målte og modellerte spektra.

Contents

1 Introduction

1.1 Background and motivation

Human kind's large consumption of fossil based energy has resulted in the climate changes [1]. In order to decrease the effects of climate change, other energy sources have to replace fossil energy. Producing electrical energy directly from solar radiation is an example of renewable energy production that contributes with minimum emissions. This technology is referred to as photovoltaics, and it plays an important role in the present and future power market.

As of 2015, photovoltaics covered 1.3 % of the world's yearly generation of electricity [2]. For the past decade Europe has seen an exponential growth in installed photovoltaic systems. In 2003 the total cumulative installed capacity in Europe was 1 GW, and at the end of 2015 it was approximately 95 GW, which was 42 % of the world's total installed capacity [2]. This increase is due to the new energy policies of several countries, the introduction of feed-in-tariffs and subsidies, which has given more incentives to invest in photovoltaic systems [3]. The Nordic countries have also experienced a growth in photovoltaic installations the past years [4]. Denmark, Sweden, Finland and Norway have respectively 789 MW, 130 MW, 20 MW and 15 MW installed capacity at the end of 2015 [2]. The Nordic countries are still a long way from reaching the levels of other European countries. One of the reasons for this large difference is the late introduction of subsidies and tenders, which were introduced much earlier in other European countries [3].

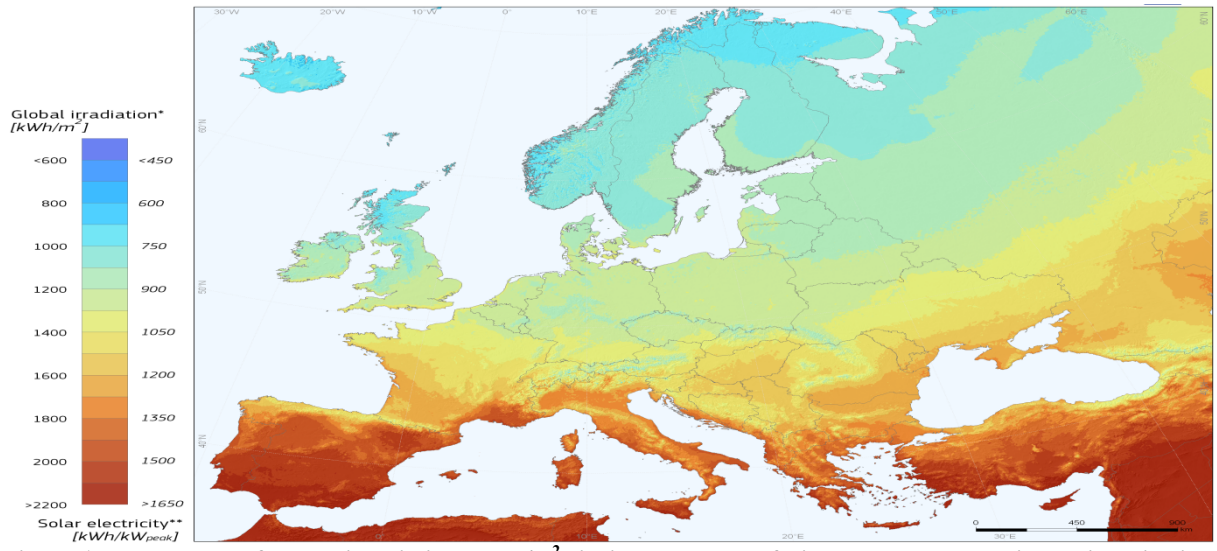

Figure 1: Yearly sum of global irradiation [kWh/m^2] incident on south-facing solar modules with optimal inclination angle. The numbers on the left side of the color bar indicate the global irradiation that each color corresponds to [5].

The low installed capacity is also due to the fact that Nordic countries yearly receive less solar energy than more southern European countries. Figure 1 displays the difference in annual global irradiation

incident on optimally inclined solar modules in Europe. It is possible to observe that some sections of the northern European countries receive as much solar irradiation as the central European countries, which have a significantly higher installed capacity. The Nordic countries may consequently have a relative good potential for producing electrical energy from solar radiation energy.

Solar cell operation is mainly affected by irradiance conditions, temperature and degradation [6-8]. Irradiation conditions are a combination of factors like shading, spectral irradiance distribution, angle of the incident light and light intensity. These factors are not just affecting the input- or output power, but also results in a change in efficiency. All these factors will vary in magnitude at different locations on Earth, where latitude and climate plays an important part. The performance of a solar module is for this reason highly dependent on its location. All manufactured solar modules are tested in the same conditions, referred to as standard test conditions (STC). The listed efficiencies of different photovoltaic technologies are based on measurements conducted under STC, and the efficiency of a solar module being placed in an environment under different conditions will consequently deviate from the STC efficiency.

The irradiance conditions and temperature in northern Europe changes severely during the course of the year and the installed photovoltaic system will have variable efficiency through the seasons. The relative low average temperatures have a positive effect on solar cell performance as the efficiency of most photovoltaic technologies tends to increase when temperature decreases [9]. The high latitudes of the Nordic countries significantly affect both the intensity and the spectral distribution of the solar irradiation. Furthermore, it is well known that variations in light intensity and solar spectrum give rise to technology dependent changes in the solar cell efficiency [10, 11].

The effects of low light intensity and variation in the solar spectrum have been thoroughly researched, but the magnitude of these variations differs with location and there is not much research material concerning the effects of irradiance conditions in the Nordic countries. It is important to test how different photovoltaic technologies perform under different irradiance conditions as there is a growing interest in the performance of photovoltaic systems under Nordic climate and insolation conditions.

1.2 Problem

This thesis aims to analyze Nordic irradiance conditions and its effects on solar module efficiency. Solar irradiation data will be collected, analyzed and presented, both global irradiance and spectral irradiance distribution.

- Global irradiance data will be collected from the FAGKLIM site at Ås.
- Spectral irradiance measurements will be conducted at Kjeller and in Grimstad by using a spectroradiometer.
- The measured spectral irradiance data will be compared with model output produced from the modelling software SMARTS.
- Light intensities and solar spectra will be compared with corresponding STC values.

The effects of the irradiance conditions will be calculated for the installed photovoltaic system at IFE, Kjeller.

- Information concerning the spectral response and low light performance will be extracted from datasheets and research material.
- The effect of varying light intensities will be calculated by comparing the efficiency under different irradiance levels with the STC efficiency.
- The spectral effects will be calculated by comparing performance under measured spectral irradiance distributions to the performance under the STC spectral irradiance distribution.

1.3 Thesis structure

Chapter 1: The background and problem is presented, and an overview of the methodology is defined.

Chapter 2: The general theory of solar energy and different measurement techniques. The operation of photovoltaic systems and the effects of light intensity and spectral distribution on solar module performance are further explained.

Chapter 3: The methodology and material implemented in performing the measurements and calculations are explained.

Chapter 4: The collected data and results are presented and discussed.

Chapter 5: Recommendations for further work is presented.

Chapter 6: The conclusion of the thesis is outlined.

2 Theory

This chapter explains solar radiation and how it attenuates when penetrating Earth's atmosphere. Different methods for measuring solar energy are also presented. In addition, the effects of varying irradiance conditions are explained.

2.1 Solar energy

The theory in the following section is in general based on the book *Understanding weather and climate* [12] with other references presented.

The Sun radiates a large amount of energy to outer space, and a fraction of this energy is supplied to Earth. Even though the Sun is located $1.5 \cdot 10^8$ km from Earth, the solar energy entering Earth's atmosphere has not been attenuated as it travels through space, but the intensity is decreased. This is based on the fact that the Sun is shaped as a sphere, and the solar energy is distributed outwards in all directions and energy is spread over a larger area as the distance from the Sun decreases. The solar intensity outside our atmosphere is not constant as the distance between the Sun and the Earth varies. The value of the solar irradiance on a surface normal to the Sun is approximately 1360.8±0.5 W/m^2 [13], and is defined as the solar constant.

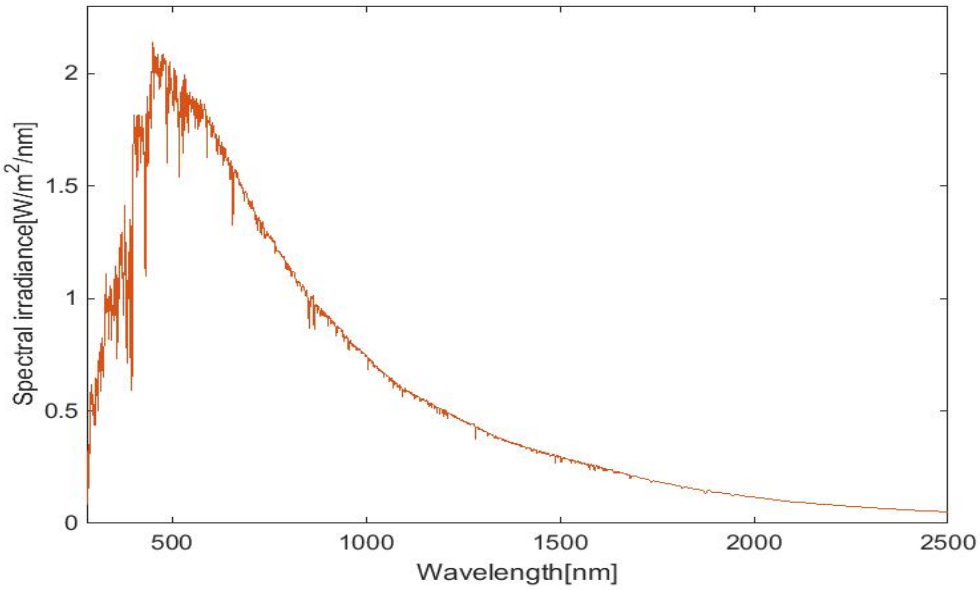

Figure 2: The solar spectrum outside the atmosphere of the Earth [14].

The wavelength distribution of the solar irradiation, before it enters the atmosphere, is shown in Figure 2. Sunlight consists of a large spectrum of electromagnetic waves, which is referred to as the solar spectrum.

2.1.1 Absorbance and scattering in the atmosphere

When the Sun light enters the atmosphere, the interaction with atmospheric gases and suspended particles known as aerosols will reduce the intensity and alter the spectral distribution. This is due to gases and other particles in the atmosphere absorbing and reflecting portions of the incoming light.

Approximately 25 % of the incoming solar radiation is absorbed in the atmosphere. The magnitude of absorbance varies between different gases and particles which may absorb different portions of the solar spectrum. Absorbance in the atmosphere decreases the intensity of the solar radiation. This is due to solar energy being transferred to the suspended molecules and the temperature of the molecules increase.

Gases, clouds and aerosols in the Earth's atmosphere reflect about 25 % of the incoming sun light back to space. Reflection in the atmosphere occurs when irradiation is not absorbed by the suspended molecules, but the radiation is redirected away from the molecule's surface. There are two types of reflection: Specular reflection and diffuse reflection. Specular reflection occurs when a single ray of light strikes a highly reflective flat surface and a single ray is reflected off the surface. The direction of the reflected ray follows the law of reflection, which states that the incident- and reflected ray creates the same angle with the normal of the surface.

Diffuse reflection, also referred to as scattering, is what usually occurs in the atmosphere. It differs from specular reflection in the way it redirects light. Scattering takes place when light that interacts with a surface is redirected as numerous weaker rays in different directions. This implies that a portion of the incoming light is also scattered towards Earth's surface. There are three types of scattering that occur in the atmosphere: Rayleigh- , Mie- and nonselective scattering.

2.1.1.1 Rayleigh scattering

This type of scattering takes place when solar radiation with short wavelengths interacts with single gas molecules. Rayleigh scattering can occur with particles that are up to one tenth of the wavelength of the light. The light is scattered both backwards and forwards, which means that some of the diffuse radiation reaches Earth's surface. The observed scattered light intensity $I_{scattered}$, which is attenuated from the incoming irradiance I_0, is dependent of the number of scattering agents N, polarizability α, wavelength of the light λ, distance from the scattering agent R and the angle of scattering θ.

$$I_{scattered} = I_0 \frac{8\pi^4 N\alpha^2}{\lambda^4 R^2}(1 - cos^2(\theta)) \quad (1)$$

Eq.(1) shows the strong wavelength dependence of Rayleigh scattering. The blue color of the sky is a product of this; short wavelengths are highly affected by Rayleigh scattering and the blue portion of the visible light is effectively scattered. The blue light is dispersed in all directions, and the human eye observes the clear sky as blue.

2.1.1.2 Mie scattering

Aerosols scatter light in a more downward manner. This type of scattering is referred to as Mie scattering, and affects a larger portion of visible light. This results in the greyish color of the sky in periods with a high concentration of aerosols in the air, which can be a result of pollution, volcanic eruptions or large fires.

2.1.1.3 Nonselective scattering

Clouds appear white or grey because the entire visible light spectrum is scattered equally. This type of scattering is called nonselective scattering because all the wavelengths of the incoming light is scattered equally. Mie scattering is a product of light that interacts with particles that are larger than aerosols, typically water droplets in clouds. Hence clouds have a big impact on the amount of light that reaches Earth's surface.

The total solar radiation that can be measured at Earth's surface is consequently approximately 50 % of the original solar energy that entered the atmosphere [15]. This solar radiation consists of both direct light and diffuse light. The direct light is the transmitted portion of the sunlight and the diffuse light is the downward component of the scattered light.

2.1.2 Air mass

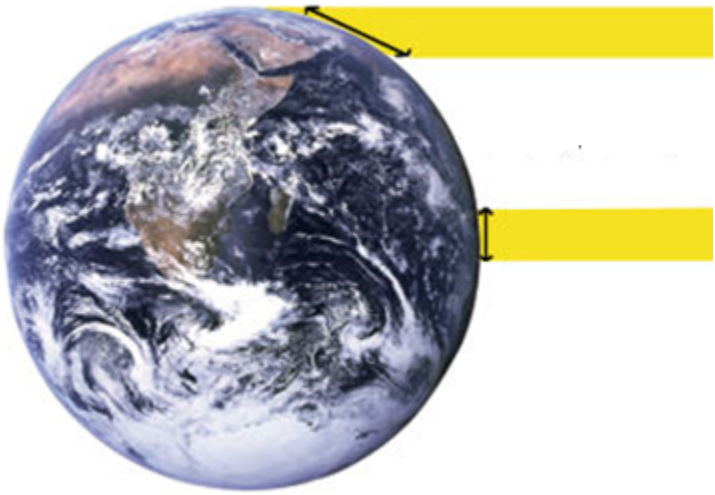

Figure 3: Light intensity at high and low latitudes [16].

Due to the curvature of Earth, the received solar intensity is not uniformly distributed. As the latitude increases, the elevation angle of the Sun decreases and the solar radiation is spread over a larger area. This effect of high latitudes is shown in Figure 3. The low elevation angle at high latitudes implies that sunlight has to travel a longer distance through the atmosphere and the incoming light will undergo more scattering and absorption. The proportion of atmosphere that the light has to penetrate is often referred to as the air mass (AM) and is estimated by the following equation:

$$AM = \frac{1}{\sin(e)} \tag{2}$$

with e being the elevation angle of the Sun.

The combination of latitude and declination angle of the Sun is the reason why the air mass is not constant through the year and hence why the light intensity varies between summer and winter. At summer solstice, when the declination angle is at its highest, the Nordic countries receive a much greater amount of sunlight compared to when the declination angle is at its lowest. The declination angle also affects the irradiation at the equator, but not in the same magnitude. Countries on the equator are hence not undergoing the same seasonal changes as high latitude countries.

2.1.2.1 Standard test conditions

In order to compare the performance of different photovoltaic technologies, with the same irradiance and temperature conditions, a set of standard conditions are defined. The standard test conditions (STC) consist of parameters that are known to affect solar cell operation. The performance of a solar cell is dependent of the temperature and a standard test temperature of 25 °C is defined. A constant incoming in-plane solar irradiance of 1000 W/m^2 is set as the standard intensity. The solar spectrum is also affected by the air mass, as spectral irradiance attenuates when the air mass increases. An air mass of 1.5 is defined as the standard air mass and hence a standardized AM 1.5 solar spectrum is created in order to compare photovoltaic technologies that respond differently to the spectral quality of the incoming light. Figure 3 illustrates the horizontal AM 1.5 solar spectrum.

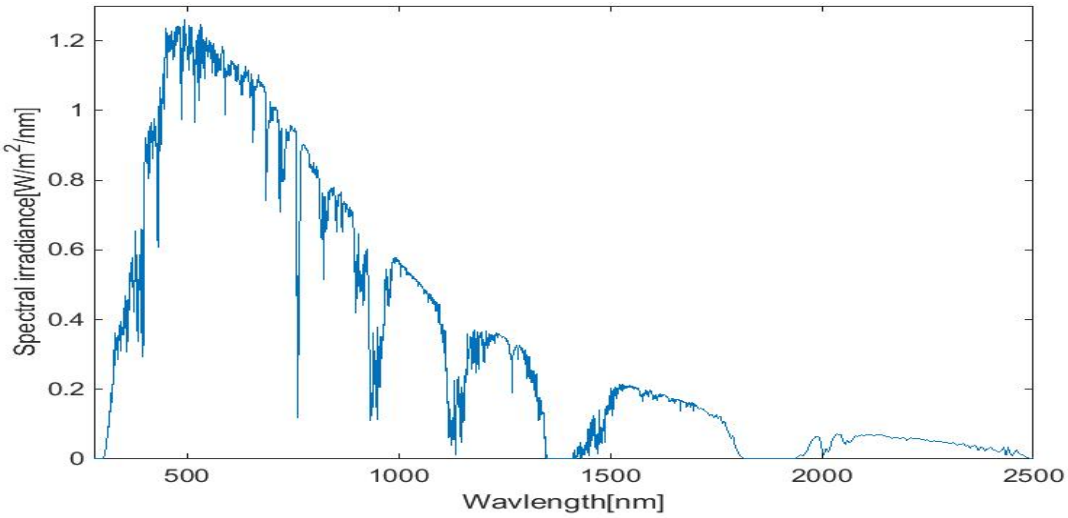

Figure 3: The AM 1.5 solar spectrum on a horizontal plane[14].

The AM 1.5 solar spectrum is significantly different than the solar spectrum outside the atmosphere. Not only is the overall intensity attenuated, but the general shape of the spectrum deviates at specific wavelengths. This is mostly due to the atmospheric gases scattering and absorbing light at different wavelengths, resulting in the observable sharp dips. The absorption bands of different gases in the ultraviolet-, visual- and near infrared region are presented in Table 4 and 5 in Appendix B.

2.1.3 Average photon energy

The average photon energy (APE) is an important factor used to characterize the shape of the solar spectra [17]. APE represents the average energy of all the incoming photons at a particular wavelength interval. APE is calculated with the following equation:

$$APE[eV] = \frac{1}{q}\left(\frac{\int E(\lambda)d\lambda}{\int \phi(\lambda)d\lambda}\right) \tag{3}$$

where q is the electron charge, $E(\lambda)$ is the spectral irradiance at wavelength λ and $\phi(\lambda)$ is the photon flux density at wavelength λ.

The photon flux density represents the number of photons impinging upon a surface at a specific wavelength:

$$\phi(\lambda)[photons\ m^{2-}\ s^{-1}\ nm^{-1}] = \frac{E(\lambda)}{hc/\lambda} \quad (4)$$

where $E(\lambda)$ is the spectral irradiance at wavelength λ, h is the Planck's constant and c is the speed of light.

APE is highly dependent of atmospheric conditions and season. High absorption or scattering of short waved light, results in a decrease of the spectral irradiance at short wavelengths. The spectral irradiance distribution in these conditions is often referred to as a "red rich" because the average energy of the photons is shifted towards the energy of photons with lower energy, which corresponds to light at longer wavelengths. The opposite occurs when the long waved portion of the incoming light is attenuated, resulting in a "blue rich" spectrum. The APE of the standard AM 1.5 spectrum, between specified upper and lower wavelength limits, is often the reference value used to determine if the spectral distribution is shifted towards blue or red wavelengths. APE smaller than this value indicates a red rich spectrum and vice versa.

Overcast and humid conditions increase APE. This blue shift is due to clouds absorbing in the long waved portion of the light and transmitting more light in the ultraviolet and blue region of the spectrum. Clear conditions decreases APE and causes a red shift in the solar spectrum, which is mostly due to a higher transmission of long wavelengths [18, 19].

Long wavelengths are enhanced in the winter period. As stated earlier, the relative high air mass in the winter time increases the scattering and absorption of the incoming light. Rayleigh scattering in the atmosphere increases especially when air mass increases, and the short waved portion of the incoming light decreases significantly in the winter time. APE values are hence low in the wintertime. In the summertime, the air mass is low, and a larger portion of short waved light is transmitted. Consequently, the summer season is characterized by high APE values [17].

2.2 Solar irradiance measurements

The theory in this section is gathered from *Quality control of solar radiation and sunshine measurements* [20], *Resource mapping of solar energy* [21] and *Spectroradiometry Methods* [22].

2.2.1 Global irradiance

Global irradiance [W/m^2] is often measured by a pyranometer, which converts thermal energy, generated from the solar radiation, into electrical signals. A typical pyranometer consists of a black disc with a dome shaped glass cover that has a 180 degree field of view. The solar energy absorbed in the black disc is transferred through a thermal resistance, and the temperature difference across the resistor creates a voltage. This voltage is detected by a computer and the voltage corresponds to a specific numerical value for global irradiance.

Pyranometers may be oriented with different tilt angles, which increases the reflected light component of the measured irradiance. This is due to the pyranometer also detecting the light reflected off the surface. The data from these measurements are therefore constrained to that specific location, for that constant position and tilt angle. The pyranometers used at irradiance measurement stations are hence placed horizontally in order to measure the more applicable horizontal global irradiance.

Figure 4: Yearly sum of global irradiation on a horizontal plane in Norway [5, 23].

Figure 4 shows that the average horizontal global irradiation in Norway varies between 900 W/m^2 in the south and 700 W/m^2 in the north. There are a large number of stations in Norway that measure solar irradiance. The majority of these stations are connected to large networks, operated by research institutes or private persons.

2.2.2 Spectral irradiance

Spectral irradiance [W/m^{2}nm] is measured by using a spectroradiometer, which measures the irradiance at a particular wavelength. The incoming light is collected through an optical lens and a monochromator disperses the light into several spectral components. The spectral components are then sensed by a detector array, a device which converts the light signals into electrical current. The output current is amplified in a signal detection system and stored in a data logging system which provides the spectral irradiance for every wavelength in a specific wavelength interval.

Spectrally resolved measurements have been performed over many decades at some measuring stations in Norway, but only for specific wavelength intervals. The station located at the FAGKLIM site at NMBU

(Norwegian University of Life Sciences) performs radiation measurements in 5 spectral bands: 295-385 nm, 400-700 nm, 495-2800 nm, 630 -2800 nm and 695-2800 nm. Similar measurements are conducted at NTNU (Norwegian University of Science and Technology) with irradiance measurements for the following wavelengths: 340 nm, 380 nm, 440 nm, 500 nm, 670 nm, 870 nm, 936 nm, 1020 nm and 1640 nm. Direct and global radiation in the interval 300 nm to 550 nm is also measured.

These measurements create good information about the energy received at certain wavelength intervals, but the data is too coarse to produce detailed information about the spectral irradiance distribution.

2.3 Photovoltaic solar cell technology

Photovoltaic solar cells convert solar radiation energy into electrical energy, based on the photovoltaic effect. Extensive research have been performed to improve the conversion efficiency of photovoltaic cells. This section addresses the basic theory of solar cell operation and the effects of varying irradiance conditions. The theory is based on the book *Photovoltaics - Fundamentals, Technology and Practice* [24], with the other references listed.

2.3.1 Photovoltaic effect

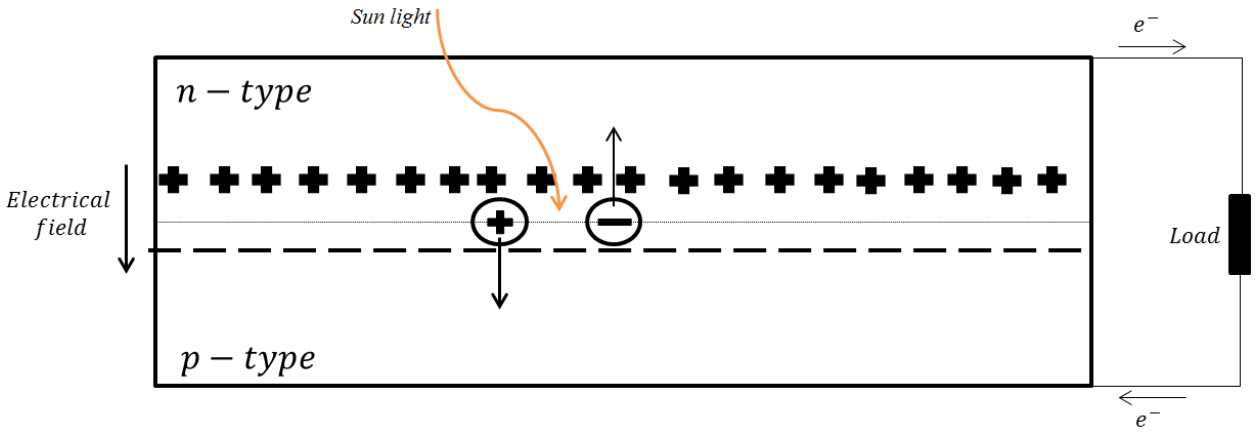

Figure 5: The generation of an electrical current in a solar cell. The light generated carriers are separated due to the electrical field and recombines as electrons move through the external circuit.

The general function of a solar cell is presented in Figure 5. If an incoming photon has energy equal or larger than the band gap of the solar cell material, the photon may be absorbed in the material and generate an electron-hole-pair. The electron represents a negative charge and the hole represents a positive charge. By connecting an external circuit to the cell the electron will flow through the external circuit, recombine with the hole on the p-side and an electrical current is created. The generation of an electron-hole-pair from solar radiation is not only creating a current, but it also builds up a voltage across the solar cell. This is referred to as the photovoltaic effect.

2.3.2 Characteristic curve

The relationship between the current and the voltage in a solar cell is often represented in a characteristic curve. The maximal power in which the solar cell can produce is specified by the maximum power point, MPP, which corresponds to a specific voltage V_{MPP}, and a specific current I_{MPP}. The maximum power produced by a solar cell is represented in the following formula:

$$P_{MPP} = V_{MPP} I_{MPP} \tag{5}$$

The characteristic curve, also called IV-curve, is essential in solar cell operation and is mainly used to give an overview of the performance of solar cells. The shape and size of an IV-curve, represented in Figure 5, are good indications of how effectively different types of solar cells absorb the incoming light and transform it to electrical energy.

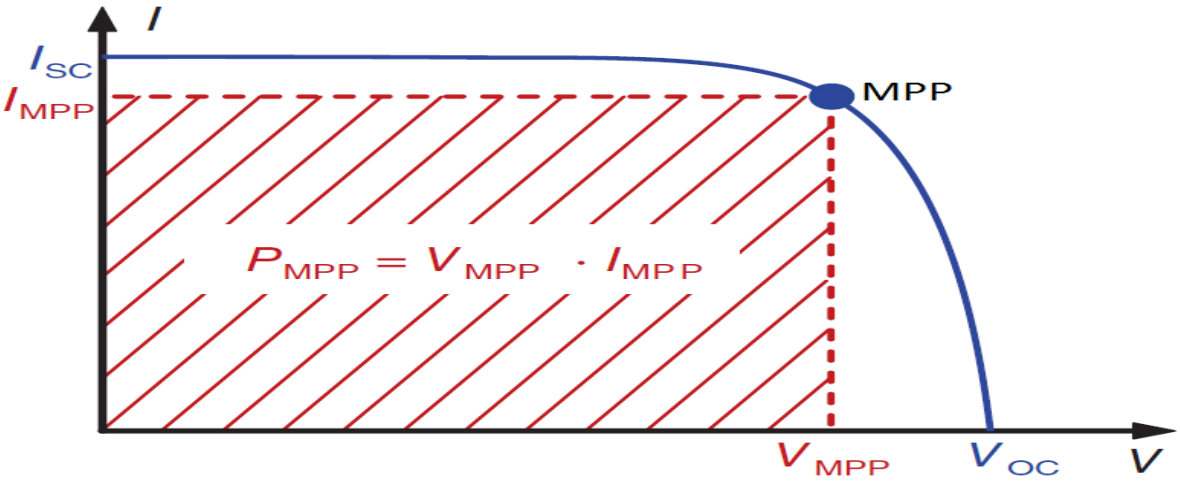

Figure 6: The IV-curve of a solar cell. V_{OC} and I_{SC} is the open circuit voltage and the short circuit current, respectively. The maximum power point MPP indicates at what voltage V_{MPP} and current I_{MPP} the maximum power is produced [24].

2.3.3 Single diode model

The characteristic curve is well suited to produce the output information of a solar cell, but the electrical losses within a solar cell are difficult to obtain from an IV-curve. An equivalent circuit, referred to as the single diode model, is one of the models that are defined to analyze the losses in a photovoltaic solar cell. Due to the simplicity of the single diode model, a more detailed and complex model, referred to as the two diode model, is often used in more sophisticated calculations.

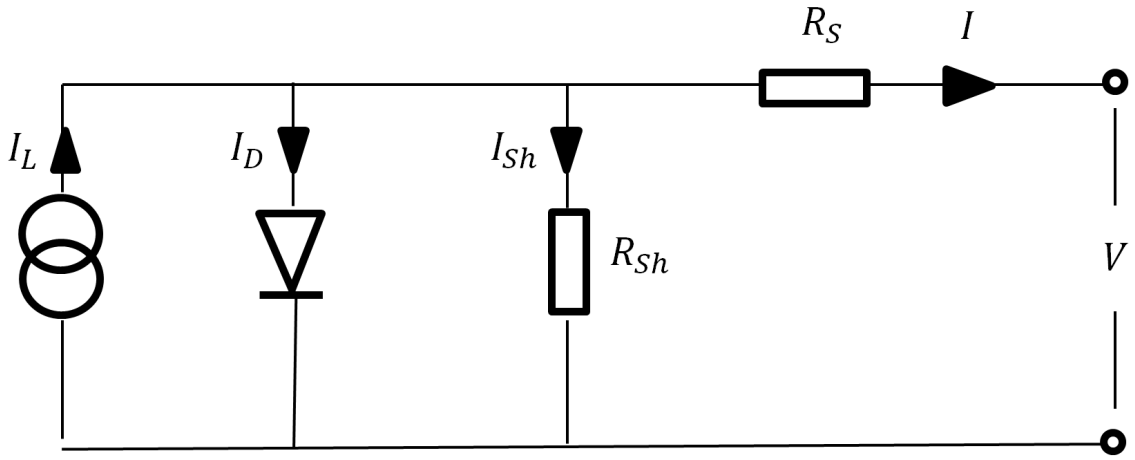

Figure 7: The single diode model of a solar cell. I_L is the light generated current and I_D is the diffusion current, also referred to as the diode current. I_{Sh} is the current through the shunt resistance R_{Sh} and I is the current through the series resistance R_S.

The single diode model, illustrated in Figure 7, replicates the ohmic losses in the solar cell, represented by the series resistance and the shunt resistance. The shunt resistance symbolizes the losses due to leakage currents in the solar cell. The series resistance represents the losses in the front and back contacts, which is the connection between the external circuit and the solar cell material. The ohmic losses in the connection between the metallic contacts and the semiconductor material are also represented by the series resistance. A solar module consists of solar cells connected in series, and the shunt and series resistance of a solar module differs consequently from that of solar cells. An effective solar has a high shunt resistance and a low series resistance. The electrical losses in a solar cell are affected by the intensity of the incoming light, and will be further described in section 2.4.

2.3.4 Quantum efficiency

The ratio between the usable light generated electron-hole-pairs and incoming photons is referred to as external quantum efficiency (EQE) and is calculated with the following equation:

$$EQE = \frac{number\ of\ usable\ electron{-}hole{-}pairs}{number\ of\ incoming\ photons} = \frac{N_{EHP}}{N_{Ph}} \tag{6}$$

The quantum efficiency is unity when all the incoming photons are absorbed and creates electron-hole-pairs, but this is difficult to achieve because of reflection, transmission and unwanted recombination in the solar cell. The deviation between the ideal and actual external quantum efficiency of a silicon solar cell is illustrated in Figure 8. The deviation is mostly due to unwanted recombination in different portions of the solar cell. The quantum efficiency is also restricted to the wavelength corresponding to the band gap of the specific solar cell material.

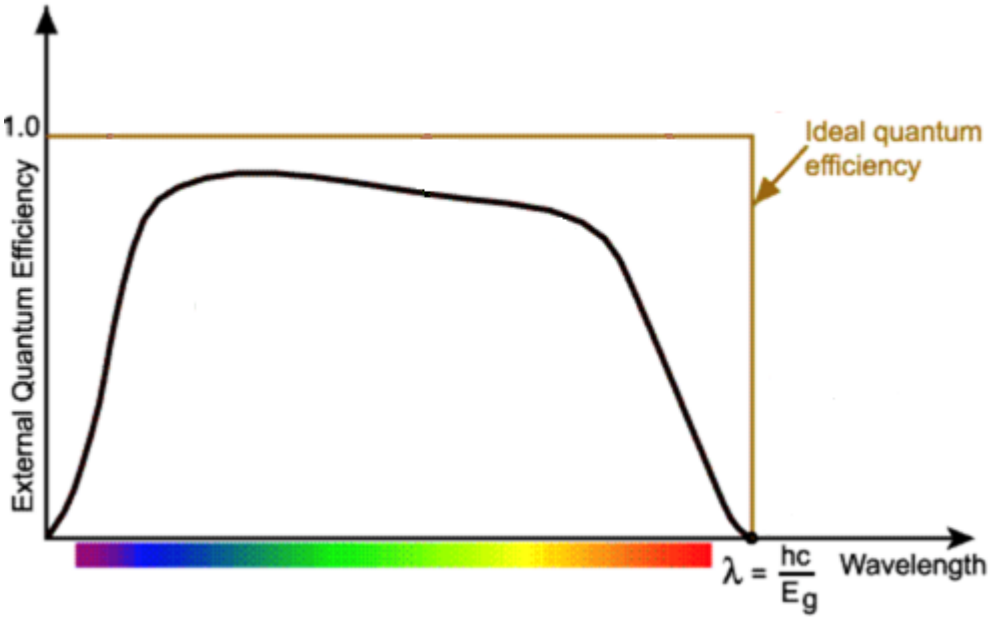

Figure 8: Ideal- (brown) and actual (black) EQE of a crystalline silicon solar cell [25].

2.3.5 Spectral response

A variation of EQE is the spectral response SR which gives the ratio of the light generated current and the power of the incoming light:

$$SR = \frac{N_{EHP} \cdot q_e}{N_{Ph} \cdot (f \cdot h)} = EQE \frac{q_e}{f \cdot h} = EQE \frac{q_e \cdot \lambda}{h \cdot c} \tag{7}$$

where q_e is the electron charge, f is the wave frequency, c is the speed of light, λ is the wavelength and h is the Planck's constant.

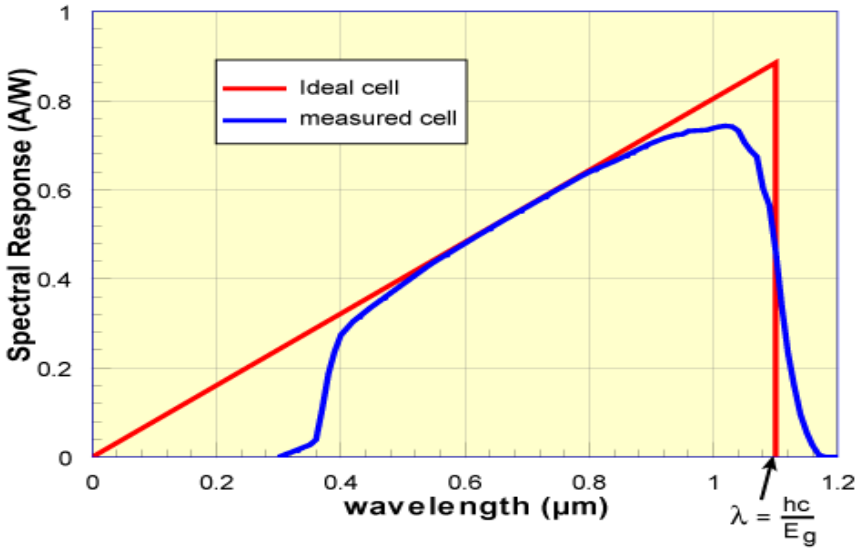

Figure 9: The deviation between the ideal and measured spectral response of a silicon solar cell under glass. The spectral response is limited at the wavelength corresponding to the band gap of silicon [26].

Each type of solar cell has a unique spectral response which is limited by the wavelength corresponding to the band gap of the solar cell material and recombination in the front and rear surface of the solar cell. This is observed in Figure 9, which shows the ideal and actual spectral response curve of a crystalline silicon solar cell. The deviation at short wavelengths is due to recombination at the front surface of the cell. This recombination occurs in the n-type material and is not contributing to the light generated current, which consequently decreases the spectral response. The same occurs at the rear surface of the solar cell. At long wavelengths the energy is only absorbed in the lower region of the p-side and unwanted recombination occurs.

The spectral response curve differs from the quantum efficiency curve due the fact that the power of incoming light increases with shorter wavelengths. Consequently, the ratio between light generated current and incoming power decreases with decreasing wavelength. The spectral response has therefore a more triangular shape compared with the squared shape of the quantum efficiency.

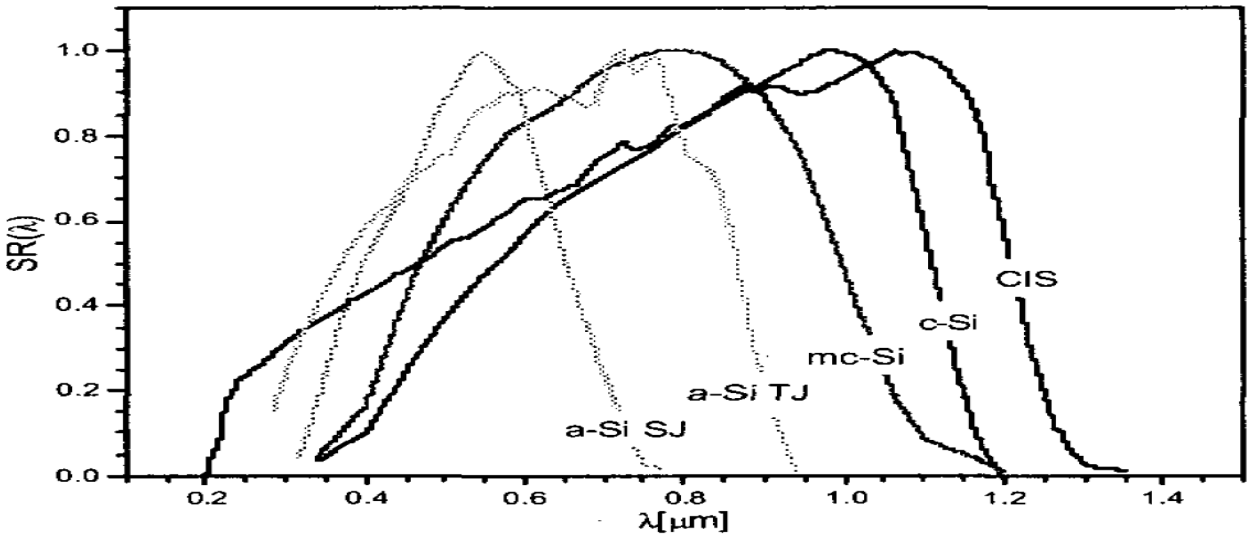

Figure 10: Spectral response of five different types of solar cells [27].

Figure 10 shows how the spectral responses of different solar cell technologies vary. The cutoff wavelength of a single junction a-Si (a-Si SJ) cell is 0.8 micrometers, while it is 1.2 micrometers for the polycrystalline silicon (mc-Si) cell. How the spectral response of different solar cell technologies affects performance in varying solar spectra is addressed in section 2.5.

2.3.6 Efficiency

One of the most important parameters in photovoltaics is how well a solar module converts the incoming solar irradiance into electrical power. The solar module efficiency η is hence the relationship between the maximum power output P_{MPP} and the irradiance G incident on a solar module with area A:

$$\eta = \frac{P_{MPP}}{G \cdot A} \tag{8}$$

In order to analyze the performance of an installed solar module, it is important to compare the actual efficiency with the efficiency stated by the producers. The relative efficiency η_{rel} is hence the ratio between the efficiency at standard test conditions η_{STC} and the actual efficiency η_{real}:

$$\eta_{rel} = \frac{\eta_{real}}{\eta_{STC}} \tag{9}$$

The separate effects of irradiance and spectral irradiance on performance are presented in section 2.4 and 2.5.

2.4 Effects of light intensity

The intensity of the incoming light is one of the most important parameters in the operation of a photovoltaic system. Not only is the energy output decreasing when the light intensity decreases, but the efficiency is also altered. The performance of different photovoltaic technologies varies differently in low light conditions, which is illustrated in Figure 11. The effect of varying light intensities is highly dependent on variations in shunt and series resistance, and recombination in the solar cell[28, 29].

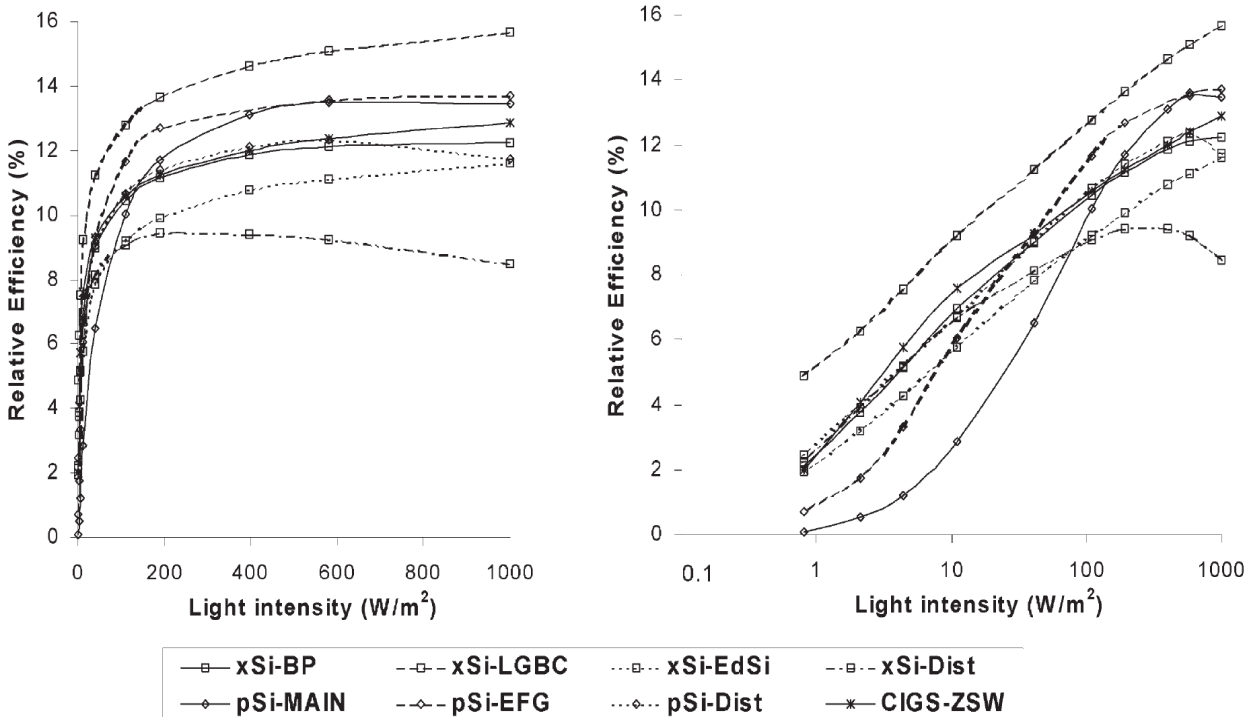

Figure 11: Relative efficiency of crystal silicon solar cells and CIS solar cells from different commercial producers. The graph on the right shows the relative efficiency vs the intensity on a logarithmic scale. The logarithmic scale is necessary in order to observe the difference between the technologies, which is difficult to observe at low intensities on the 10 scale based graph on the left [30].

2.4.1 Series resistance

High currents produced at high light intensities are mainly affected by the series resistance. The ohmic losses P_{loss}, a result of current I flowing through a series resistance R_S, is calculated with the use of the following equation:

$$P_{loss} = I^2 R_S \tag{10}$$

The relationship between current and power loss in Eq.(9) shows that an increase in current quadruples the power loss. Thus the magnitude of the light induced current is a highly important parameter in analyzing the power losses in a solar cell.

In Figure 11, it is possible to observe that some of the silicon based solar cells have a slightly higher efficiency at particular intensity values lower than the STC light intensity of 1000W/m^2. This is due to the fact that there is less current produced, and the ohmic loss through the series resistance decreases [31].

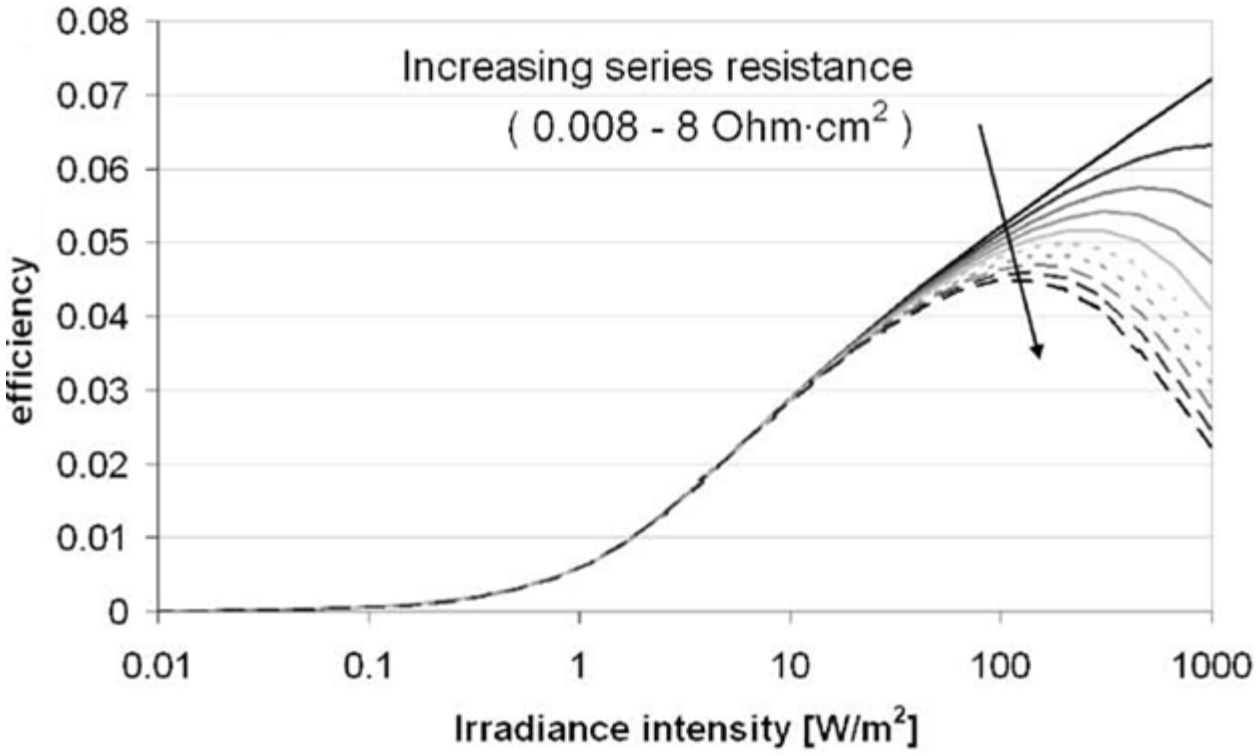

Figure 12: The modelled effect of low light on the efficiency of a solar cell with varying series resistance. The different line patterns symbolize the different values of resistance, with the bold filled line representing the lowest resistance and the bold dashed line representing the highest resistance [28].

The effect of series resistance is presented in more detail in Figure 12. Solar cells with low series resistance maintain higher efficiency as light intensity is reduced, compared to a solar cell with higher series resistance. Solar cells with high series resistance experience an increase in efficiency when the light intensity decreases. This explains the behavior observed in Figure 11. Commercial crystalline silicon solar cells have a maximum series sheet resistance of about 2Ωcm^2 [28].

2.4.2 Shunt resistance

In low light conditions, when the light generated current is low and the voltage is high, the shunt resistance has a large impact on efficiency. The shunt resistance is a result of manufacturing errors which may create alternative routes for the current to flow through the solar cell material.

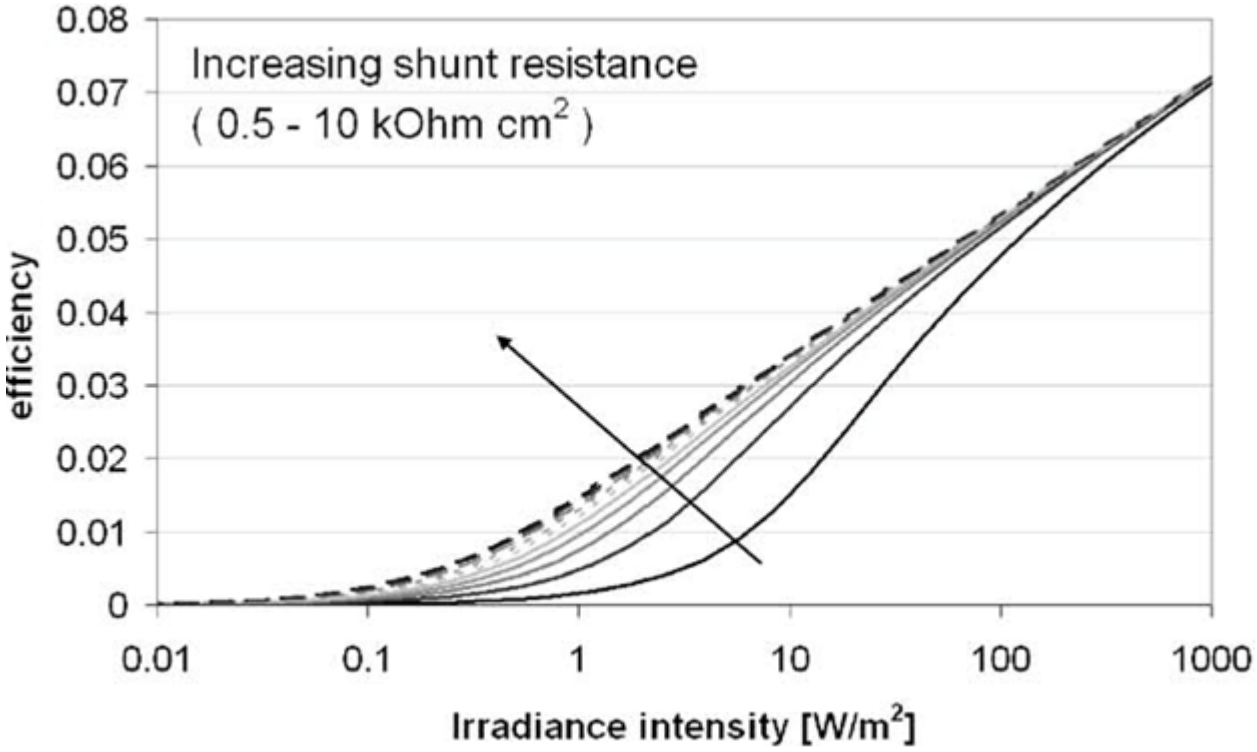

Figure 13: Modelled effect of low light on the efficiency of a solar cell with varying shunt resistance. The different line patterns symbolize the different values of resistance, with the bold filled line representing the lowest resistance and the bold dashed line representing the highest resistance [28].

In good light conditions, the leakage current is a small portion of the total current. As the light intensity decreases, the magnitude of leakage current is constant but the overall current has decreased in accordance with the irradiance. The current through the shunt resistance is hence very important to minimize in order to optimize the efficiency in low light conditions. The modeled values illustrated in Figure 13 represent the effect of low irradiance and shunt resistance. Shunt resistance values above 1000 Ωcm^2 are usually accepted values in solar cell production [8].

Information about the series and shunt resistance of different solar cells is valuable in order to predict the performance in different locations around the world. A solar module installed in a geographical location with an average high light intensity close to STC levels would preferably consist of solar cells with low series resistance. High shunt resistance is on the contrary more important at locations with low light conditions.

2.4.3 Relative efficiency with respect to light intensity

The impact of light intensity on solar module performance may be analyzed by calculating the ratio between STC efficiency and the efficiency at different irradiance levels. The relative efficiency η_{rel} with respect to varying light intensities G is calculated with the following equation:

$$\eta_{rel} = (P_{max}/G)/(P_{STCmax}/G_{STC}) \quad (11)$$

where P_{max} is the maximum power output produced at the specific irradiance G and $P_{\max STC}$ is the maximum power output at the STC light intensity G_{STC}.

2.5 Spectral effects

The efficiency of a solar module is also affected when there is a mismatch between the spectral distribution of the incoming light and the spectral response of the solar cell material [27, 32]. The mismatch results in a spectral loss as a portion of the incoming energy is not exploited.

2.5.1 Spectral factor

The spectral factor (SF), also referred to as the mismatch factor, indicates the performance of the considered solar module under the actual spectrum relative to the performance under the standard AM 1.5 spectrum. SF is calculated with the following equation:

$$SF = \frac{\int E(\lambda)SR(\lambda)d\lambda \cdot \int E_{AM1.5}(\lambda)d\lambda}{\int E_{AM1.5}(\lambda)SR(\lambda)d\lambda \cdot \int E(\lambda)d\lambda} \quad (12)$$

where $SR(\lambda)$ is the spectral response at wavelength λ, $E(\lambda)$ is the actual spectrum at wavelength λ and $E_{AM1.5}(\lambda)$ is the AM 1.5 spectrum at wavelength λ. SF less than 1 means the solar module performs worse under the actual spectrum compared to under the standard spectrum. SF greater than 1 implies better performance under the actual spectrum. Solar cell materials with a narrow band gap absorb less of the energy from the entire solar spectrum, compared to materials with a larger band gap. By observing the spectral responses in Figure 10 section 2.3.5, the band gap of an a-Si solar cell is for example narrower than the band gap of a thin film CIS solar cell, and will less efficiently absorb the energy of the incoming light. This is true for a situation when the intensity of the solar spectrum is high and there is a red shift in the spectrum. In conditions when the spectral composition of the light is shifted towards the shorter wavelengths, the material with the highest spectral response in the region with short wavelengths will perform better.

3 Methodology and experimental setup

This chapter addresses the methodology concerning the irradiance- and spectral irradiance measurements. Computer modelling of the solar spectrum will also be described in detail. In addition, the two solar modules implemented in the performance calculations will be presented.

3.1 Spectral irradiance measurements and calculations

This section explains the operation of the spectroradiometer and how spectral irradiance is measured at Kjeller and in Grimstad. In addition, the use of the modeling program SMARTS is described in detail.

3.1.1 Spectroradiometer

Figure 14: PSR-1100F Spectroradiometer [33].

The portable spectroradiometer PSR-1100F, produced by Spectral Evolution, is used to measure solar spectra at the two measurement locations. The instrument is presented in Figure 14. The spectroradiometer is also designed to measure radiation, reflectance and absorbance. The instrument's detector is a 512 element Si Photodiode Detector Array. The spectroradiometer measures spectral irradiance in the wavelength band 320-1100nm. The measurements uncertainty at wavelengths 350 nm, 654.6 nm and 900 nm is 3.2 %, 3.1 % and 3.2 %, respectively. The spectroradiometer is supplied with a 25 degree field of view fiber optic cable. The optical input of the fiber is possible to adjust, and a diffuser with a 180 degree field of view is used to measure spectral irradiance on a horizontal plane.

The spectroradiometer measurements may be stored in the instruments flash memory or on a separate computer. Communication between the instrument and computer is performed using USB or Bluetooth. Continuous measurements are possible to operate remotely when connected to a computer. The spectroradiometer is powered by a Li-Ion battery, which is stated to deliver enough power to measure spectral irradiance in standalone mode for 3 hours. The battery is only possible to recharge when removed

from the instrument. More information about performance-, physical- and environmental specifications is supplied in Appendix E.

It is possible to operate the PSR-1100F remotely when connected to a computer by USB or Bluetooth. The computer software DARWin SP allows the user to remotely control, save and analyze measurements performed by the spectroradiometer. The software is only applicable for Windows platforms. For each particular measurement DARWin SP creates two output files, a RAW file and a SED file. A graph showing spectral irradiance plotted vs the wavelength is stored in the RAW file. The SED file is a text file which consists of detailed information about the measurement, and a table presenting the spectral irradiance value at each wavelength. The SED file is possible to analyze further in more analytical software packages. An example of the information presented in a SED output file is shown in Appendix C.

3.1.2 Measuring station Kjeller

Figure 15: Location of the measurement site at Kjeller [34].

The measuring station at Kjeller is located on the roof of the Solar Energy Department building at IFE, with a latitude of 59° 58' N. The location is represented in Figure 15.

New equipment for measuring spectral irradiance was acquired by IFE before the start of this thesis and a significant outcome of this work has been the establishment of a measurement setup for measuring spectral and time-resolved solar irradiance at Kjeller.

Because shadows and reflections will alter the incoming irradiation, the location of the measurement site is critical. Several possible locations at IFE were inspected. Only the roof of the Solar Energy Department building was found suitable. The flat roof top of this building is located high above other large objects and is easily accessed. Due to significant HMS considerations with respect to the fumes from the solar lab, permission to use the roof of the Solar Energy Department building was first given on the 01.03.16. The work was conducted in collaboration with Lenny Enstrom, Josefine Selj and Sean Erik Foss.

Additional equipment was obtained and tested in order to maintain a practical and stable setup. An appropriate measurement procedure and data storage routine was defined in order to achieve consistent measurements. The first proper measurement sequence at Kjeller was performed on the 09.03.16.

The spectroradiometer is not built to endure long measurement periods in cold and wet conditions. The datasheet of the PSR-1100F states a minimum operation temperature of -10℃. The instrument is constructed for field work, but how it performs in snow and rain is not clearly stated in the datasheet. The computer connected to the spectroradiometer would also not function properly in wet or snowy conditions. The measurement equipment is hence always stored inside when measurements are not taking place and no measurements were performed in weather conditions with temperatures around -10℃ and precipitation.

Only horizontal measurements are performed at this measurement site. The measurement setup at Kjeller includes a tripod, which makes it possible to maximize the height of the diffuser. It is beneficial to position the diffuser as high as possible in order to minimize the effect of reflected light from surrounding object. The diffuser is connected to the tripod by using a handheld probe. The handheld probe and tripod head is connected with a screw. The diffuser is fastened to the probe by threading the fiber optic cable through two openings and then fastening the end of the cable with a perpendicular facing screw. The tripod also adds more stability, which results in more consistent measurements. The tripod head is possible to rotate in all three dimensions. Two integrated spirit levels are adjusted to obtain a horizontal position for the diffuser. Due to the length of the fiber optic cable the spectroradiometer is attached to the tripod with a carbine hook. A USB cable is connecting the spectroradiometer and portable computer. The short USB cable used at the test site in Grimstad is replaced with a longer cable. This makes it possible to place the computer at a dry platform two meters from the setup. Figure 16 shows the measurement setup at Kjeller and a more detailed overview of the diffuser-probe-connection.

Figure 16: The measurement setup at Kjeller (left) and the diffuser-probe-connection (right). The diffuser is fastened to the probe with the black screw located on the left side of the probe.

Due to the physical specifications of the spectroradiometer and computer, all of the measurement equipment is carried up to the roof for every measuring sequence. The diffuser is hence not placed at the exact same position and with the exact same tilt angle. For measurements performed on the 16.03.16 and 18.03.16, the measurement procedure was slightly altered by adding an additional spirit level in order to further reduce the uncertainty in the positioning of the diffuser. The handheld probe connecting the diffuser with the tripod does not have an optimal fastening system for the diffuser. The perpendicular screw is not adequate to maintain a stable connection. The poor fastening system may result in wind gusts moving the fiber optic, and slightly tilting the diffuser.

3.1.3 Measurement procedure

As stated earlier, the rechargeable battery pack supplies the instrument with enough power to operate for 3 hours. An extra battery pack is used in case the other battery runs out of power. Tests showed that it was possible to have the instrument operating at more than 3 hours, and still be able to keep a high measurement frequency. In order to achieve detailed data concerning the varying solar spectra, and still be able to operate the instrument for a long period, it was decided that a measurement frequency of 10 seconds would be sufficient. Every measurement sequence conducted at Kjeller and in Grimstad therefore consist of 10-second measurements.

As mentioned above, the measurement equipment has to be reassembled for every new measurement sequence. As a result of this, certain routines had to be defined in order to achieve consistent measurements. Before each new measurement sequence the following guidelines are to be followed:

- Insert a fully charged battery back, and charge the used battery pack.
- The diffuser is to be placed at the same position as in previous measurements. The tripod is hence supposed to be positioned at the same location for each measurement.
- It is important to make sure that the fiber optic, USB cable and charger is properly inserted.
- The output name is changed so the generated output files display the date of the current measurement day. This makes it easier to separate the measurement sequences.
- The diffuser has to be lined up horizontally. This is done by using the integrated spirit levels or preferably a separate spirit level.

Due to long measurement periods ranging between one to four hours, the use of the data storage service Google Drive (https://www.google.com/drive/) is implemented in the measurement procedure at Kjeller. Every 10-second measurement is instantly stored in the portable computer's Google Drive folder and uploaded to an online storage system. This makes it possible to observe the data being collected in real time. This also creates an online copy of each measurement. If the online upload stops, it will be an indication that the spectroradiometer is no longer taking measurements.

3.1.4 Measuring site in Grimstad

Figure 17: The location of the measurement station in Grimstad [35].

The measuring site in Grimstad is located on a roof at the University of Agder, with a latitude of 58° 20' N. Figure 17 shows the location of the test site. The site is used by the Faculty of Engineering and Science as a test station for outdoor I-V curve measurements of several different PV technologies [36].

Both tilted and horizontal spectral measurements are performed at this site. The spectral irradiance measurements were performed with help from Anne Gerd Imenes and Georgi Hristov Yordanov. The tilted spectral irradiance measurements are conducted in the plane of the installed solar modules, which are tilted with an angle of 39±1°. The tilted diffuser is fastened with tape, in the same position as the already installed measurement instruments.

The horizontal measurements are measured by connecting the diffuser to a rail. A spirit level is used to check that the diffuser is mounted horizontally. The rail is located a couple of meters from the rack. The diffuser is not placed at an optimal height, because the solar module rack, located to the North of the diffuser setup, is higher than the measuring point. The height of the measuring point is restricted by the length of the fiber optic cable connecting the diffuser and spectroradiometer. The horizontal diffuser is connected to the rail by taping the diffuser to a small plastic box, which is taped directly to the rail. The tape keeping the diffuser connected with the rail might lose some of its adhesiveness during the measurement sequences. The diffuser is aligned by using a spirit level, but it is only applied in the beginning of each measurement sequence. If, during the measurement sequence, the diffuser is tilted towards the Sun the measured spectral irradiance will increase, and vice versa. On the other hand, this variation might be limited by the diffuser's 180 degree field of view. Measurements performed with the diffuser are consequently not effected to the same extent as that of optics with smaller fields of view.

A USB cable connects the spectroradiometer with a portable computer. The set up for the tilted and horizontal measurements is shown in Figure 18.

Figure 18: Diffuser tilted 37 degrees with respect to the horizontal (left) and diffuser positioned horizontally (right).

3.2 Irradiance measurements and calculations

This section describes the measuring station at Ås, and how irradiance data is measured and analyzed.

3.2.1 Measuring station at Ås

Figure 19: The location of the measurement station at Ås [37].

The measuring station FAGKLIM is located on the Sørås field in Ås, Akershus. The location is shown in Figure 19. The station is located 93.3 meter above sea level with coordinates: 59° 39’ 37’’ N and 10° 46’ 54’’ N. The station is maintained by NMBU (Norwegian University of Life Sciences). The FAGKLIM site measures several meteorological parameters and have been doing this since 1859[38].

3.2.2 Global irradiance measurements

Figure 20: Eppley Precision Pyranometer used at the FAGKLIM site [39].

Global irradiance measurement at FAGKLIM started in 1972. Global irradiance is measured with an Eppley Precision Pyranometer, which operates as described in section 2.2.1. The pyranometer is presented in Figure 20. Irradiance is measured in a wavelength interval of 295-2800nm. The pyranometer has an approximate uncertainty of 10 % [39]. The pyranometer is cleaned every weekday, which minimizes the uncertainty related to soiling.

The log system connected to the pyranometer obtains irradiance values every 10 seconds and the middle value for every 10 minute is stored in a database. The database is controlled and corrected by Signe Kroken at NMBU.

3.2.3 Typical Meteorological Year at Ås

Typical Meteorological Year (TMY) is a dataset which describes the climate at a given location based on data collected over several years. This thesis will compare measured irradiance at Ås with the TMY for yearly global irradiation at Ås. TMY at Ås for the period 1991-2010 is shown in Table 1. The data included in the TMY is based on the monthly means of each month. Because the TMY values for Ås are only composed of monthly values, time-resolved irradiance measurements, conducted between 2011 and 2015 at Ås, are used in the further analyzes.

Table 1: TMY values for global irradiation at Ås for the period 1991-2010. Max, Min and Mid represents the maximum, minimum and middle irradiation values for each month. Std.av. is the standard deviation for the monthly value with respect to the monthly mean value. The letter n symbolizes the number of datasets obtained for each month [40].

1991-10	Max	Min	Mid	Std.av.	n
J	44	29	37	4	20
F	124	65	98	12	20
M	299	176	253	34	19
A	450	250	368	51	20
M	657	447	566	58	20
J	693	411	597	74	19
J	700	466	587	70	18
A	578	393	459	45	19
S	342	213	278	32	19
O	182	82	123	22	20
N	54	22	42	10	20
D	29	14	22	3	20
SUM	4150	2568	3431		

3.2.4 Total energy and relative energy contribution

The total yearly solar irradiation E_{tot} [kWh/m^2] is calculated with the following equation:

$$E_{tot} = \sum_{i=1}^{52560} G_i \frac{1}{6000} \tag{13}$$

where G_i [W/m^2] is the average measured global irradiance for every 10 minute interval, which corresponds to the energy received during 1/6 hour. Each of the 52560 measurements, symbolized by the letter i, were divided by 6000 in order to find the yearly irradiation presented in kWh/m^2.

Different light intensities contribute with different amounts of energy. It is relevant to analyze the relative energy contribution of different light intensities, which is an important factor in characterizing irradiance conditions. The relative energy contribution (REC) for light intensity intervals between 0 and 1000W/m^2, separated by 100W/m^2, is calculated with the following equation:

$$REC_{(j,j+100)} = \frac{\sum_{i=1}^{52560} \frac{j \leq G_i \leq (j+100)}{6000}}{E_{tot}} \tag{14}$$

where G_i is the average measured global irradiance for every 10 minute interval, E_{tot} is the total energy received during a year, j defines the light intensity interval and i symbolize ith measurement conducted through a year.

3.2.5 Standard deviation

Standard deviation represents the reliability of the measured data. In this thesis, standard deviation will be calculated in order to characterize how measurements x_i deviates with respect to a mean value $\bar{x}$:

$$SD = \sqrt{\frac{1}{N-1}\sum(x_i - \bar{x})^2} \quad (15)$$

where N is the number of measurements.

3.2.6 SMARTS

Due to the limited amount of spectrally resolved irradiation data concerning the solar spectrum in the Nordics the FORTRAN code SMARTS (Simple Model of the Atmospheric Radiative Transfer of Sunshine) will be used to simulate the solar spectrum at different times of the year [41]. Establishing an accurate SMARTS model will also give the opportunity to generalize the evaluation of spectral effects of different technologies to new locations, without performing spectral irradiance measurements at the given location. SMARTS is well accounted for in research material concerning spectral irradiance distribution and comparison between measured and simulated spectra [42]. The model is also used in photovoltaics applications for analyzing the effects of varying spectral irradiance distributions [43]. The model was developed by Dr. Christian Gueymard. The algorithms in the model gives similar output values as the complex radiative transfer code used in the band model MODTRAN[44]. This band model is based on dividing the atmosphere into different layers, and implementing vertical profiles of gases and particles. SMARTS is less complex and implements similar algorithms in combination with spectral albedo functions and input files containing atmospheric data[45]. SMARTS is free to download from the website of NREL (National Renewable Energy Laboratory) http://www.nrel.gov/rredc/smarts/download.html.

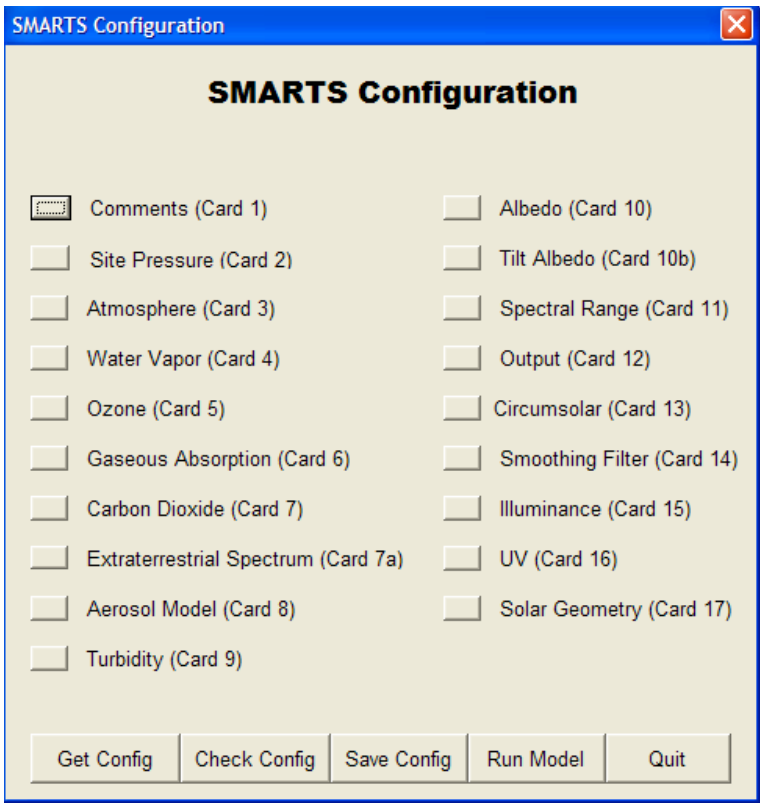

Figure 21: The different input parameters, represented as cards, in SMARTS [46].

The input parameters of the SMARTS model are based on a large variety of factors that in total defines the atmospheric composition and the model's output. Extraterrestrial spectra, gaseous composition, turbidity and albedo are examples of variables definable in SMARTS. Each parameter, represented as cards, is shown in Figure 21. The model is based on a FORTRAN program which is operated by running a user defined ASCII text input file. The input file is defined by directly creating a text file or by creating it in the user friendly Interface which is possible to use on a Windows platform. The FORTRAN code reads the input file and generates a set of output files. This code may be run in the system command line or in the interface. The output files are generated as ASCII text files. The output files contain the output data and the input arguments. The output data for the modelling performed in this thesis is horizontal spectral irradiance, but a large variety of output data is available. The input values for each parameter used to generate the AM 1.5 standard spectrum [14] are shown and partially described in Table 2. Examples of input- and output text files used in SMARTS are presented in Appendix D.

Table 2: General description of the values corresponding to each parameter card. The input file generates the AM 1.5 solar spectrum. Not all values are presented [43].

Card ID	VALUE	Parameter/Description/Variable Name
1	'ASTM_G173_Std_Spectra'	Comment line
2	1	Pressure input mode (1 = pressure and altitude): ISPR
2a	1013.25 0.	Station Pressure (mb) & altitude (km): SPR, ALT
3	1	Standard Atmosphere Profile Selection (1 = use default atmosphere): IATM1
3a	'USSA'	Default Standard Atmosphere Profile: ATM (one of eleven choices, including user defined)
4	1	Water Vapor Input (1 = default from Atmospheric Profile): IH2O (may be user specified)
5	1	Ozone Calculation (1 = default from Atmospheric Profile): IO3 (may be user specified)
6	1	Pollution level mode (1 = standard conditions/no pollution): IGAS (for 10 pollutant gases)
7	370	Carbon Monoxide volume mixing ratio (ppm): qCO2
7a	1	Extraterrestrial Spectrum (1 = SMARTS/Gueymard): ISPCTR (one of seven choices)
8	'S&F_RURAL'	Aerosol Profile to Use: AEROS (one of 10 choices, including user specified)
9	0	Specification for aerosol optical depth/turbidity input (0 = AOD at 500 nm): ITURB
9a	0.084	Aerosol Optical Depth @ 500 nm: TAU5
10	38	Far field Spectral Albedo file to use (38= Light Sandy Soil): IALBDX (on of 40 choices, including user defined)
10b	1	Specify tilt calculation (1 = yes): ITILT
10c	38 37 180	Albedo and Tilt variables—Albedo file to use for near field, Tilt, and Azimuth: IALBDG, TILT, WAZIM
11	280 4000 1.0 1367.0	Wavelength Range—start, stop, mean radius vector correction, integrated solar spectrum irradiance: WLMN, WLMX, SUNCOR, SOLARC
12	2	Separate spectral output file print mode (2 = yes): IPRT: Spectral & broadband files
12a	280 4000 .5	Output file wavelength—Print limits, start, stop, minimum step size: WPMN, WPMX, INTVL
12b	2	Number of output variables to print: IOTOT (up to 32)
12c	8 9	Code relating output variables to print (8 = Hemispherical tilt, 9 = direct normal + circumsolar): OUT(8), OUT(9) [up to 32 spectral parameters available for output]
13	1	Circumsolar calculation mode (1 = yes): ICIRC
13a	0 2.9 0	Receiver geometry—Slope, View, Limit half angles: SLOPE, APERT, LIMIT
14	0	Smooth function mode (0 = none): ISCAN (Gaussian and triangle filter shapes can be specified)
15	0	Illuminance calculation mode (0 = none): ILLUM (Luminance and efficacy may be selected)
16	0	UV calculation mode (0 = none): IUV (UVA, UVB, action weighed dosages available)
17	2	Solar Geometry mode (2 = Air Mass): IMASS (zenith and azimuth, date/time/lat/long available)
17a	1.5	Air mass value: AMASS

In this thesis, the majority of the parameter values used in the modelling are based on measurement data and simulations performed by different institutions:

- Data concerning temperature, precipitation and pressure is extracted from the climate database of the Norwegian Meteorological Institute, using the web portal eKlima (http://eklima.met.no).
- Turbidity and gaseous composition in the atmosphere is obtained from research material published by NILU (Norwegian Institute for Air Research).

- Elevation angles for different dates are obtained from the National Oceanic & Atmospheric Administration Solar Calculator. The data implemented in the calculator is provided by NOAA ESRL Global Monitoring Division, Boulder, Colorado, USA (http://esrl.noaa.gov/gmd/).

Not all parameters in SMARTS are possible to obtain for the given locations. Where data is not accessible, default estimations from SMARTS have been used. SMARTS is only applicable for clear sky modelling. SEDES1[18] is an example of a model that may be used to model the solar spectrum for cloudy skies, but it will not be implemented in this thesis due to a short time frame.

3.3 Matlab

The measurement data is imported and analyzed with the software package MATLAB R2014b [47]. The datasets produced from measuring irradiance and solar spectra are used in large scale calculations, which MATLAB executes efficiently. All calculations are performed in MATLAB, and the majority of the results are plotted with MATLAB. The code for all calculations in this thesis is available on request.

3.4 Plot Digitizer

The Java program Plot Digitizer [48] is used to extract data from different scanned plots. This program is used when relevant data concerning the solar modules is presented in a plot, but not with corresponding numerical table values.

3.5 Tested solar modules

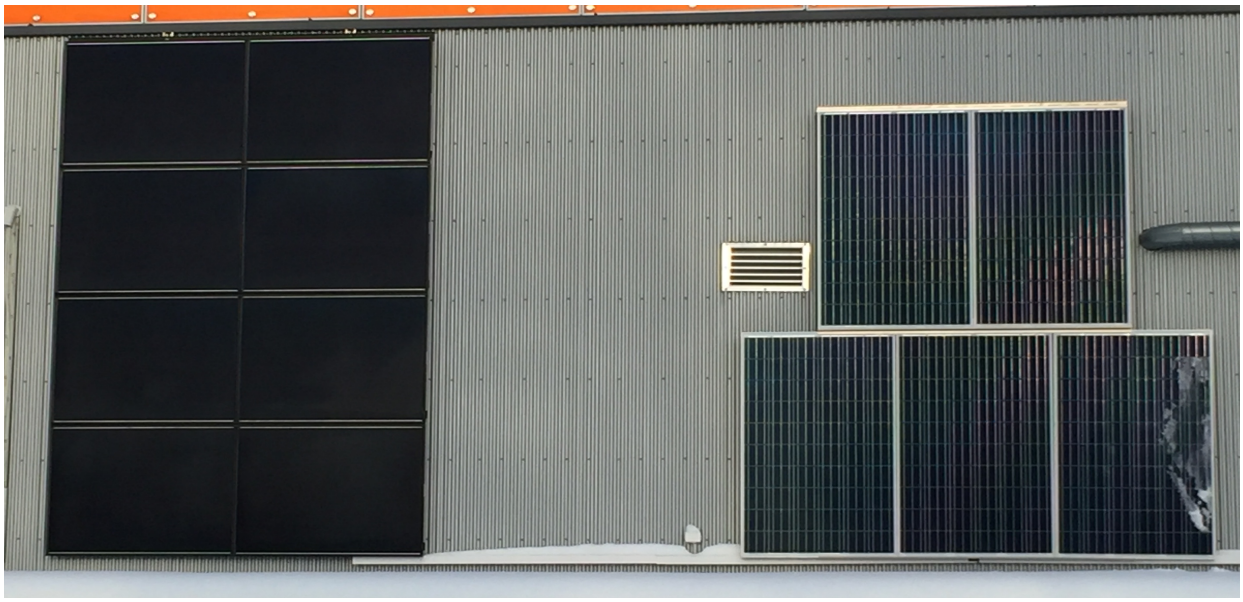

Figure 22: CIS modules (left) and p-Si modules (right) attached to the south facing wall of the Solar Energy Department building at Kjeller.

Two solar modules, based on different PV technologies, are analyzed in this thesis: p-Si (Polycrystalline silicon) and CIS (Copper-indium-disulfide). These solar modules are installed on the wall of the Solar Energy Department building at IFE, which are shown in Figure 22. The polycrystalline silicon solar

module IBC PolySol 260 CS is produced by IBC Solar, and has an STC efficiency of 15.9 %. The CIS thin film solar module SF165-S is produced by Solar Frontier, and has an STC efficiency of 13.4 %.

More information concerning electrical characteristics and other performance data is presented in the corresponding datasheets in Appendix A.

4 Results and discussion

4.1 Irradiance at Ås

This section presents and analyzes the global irradiance data collected for Ås. The performance of the CIS- and p-Si solar module in varying light intensities are also calculated and presented.

4.1.1 Total energy and relative energy contribution

The total energy and relative energy contribution in Ås is based on global horizontal irradiance measurements from Ås, collected in the period 2011-2015 [40]. The yearly total energy received was calculated with Eq.(13) section 3.2.4, and converted to MJ/m^2 in order to match the TME values. The standard deviation of the yearly energies with respect to TMY was calculated with Eq.(15) section 3.2.5. The yearly energy values and standard deviation are presented in Table 3. The relative energy contribution for 2011- 2015 is calculated with Eq.(14) section 3.2.4 and calculated values are presented in Figure 23.

Table 3: Yearly measured solar energy at Ås and standard deviation with respect to TMY (1991-2010).

Year	Total energy[MJ/m^2]	Standard deviation[MJ/m^2]
2011	3282	74.5
2012	3229	101
2013	3351	40.0
2014	3373	29.0
2015	3586	77.5

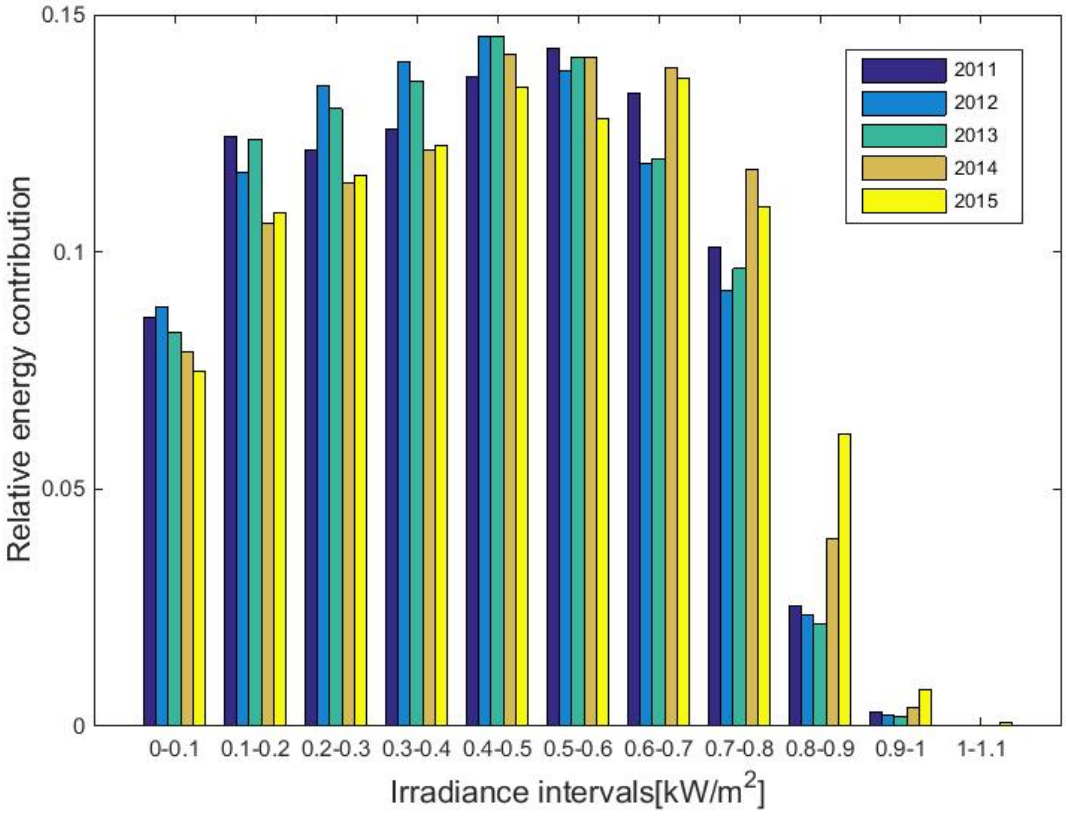

Figure 23: The relative energy contribution with respect to irradiance levels. Calculations are based on data collected from the measuring station at Ås, between year 2011 and 2015.

The standard deviation presented in Table 3 represents the deviation between total solar energy received each year and TMY based on the period 1991-2010, which is shown in Table 1 section 3.2.3. The standard deviation ranges between 29.0 MJ/m^2 and 101 MJ/m^2. The year 2015 was the only year in which the yearly irradiation was higher than TMY. The measured data for 2011-2015 is therefore a good indicator of the irradiance conditions at Ås.

By observing Figure 23, it is clear that the relative energy contribution varies from year to year. Compared to other years, during year 2015 the station measured significantly more solar energy at light intensities between 800 W/m^2 and 1100 W/m^2. Table 3 shows that the yearly irradiation in 2015 was relatively higher than that of the other years. The relative energy contribution at high irradiance levels may consequently be linked to high irradiation levels in 2015. The relative energy contributions at high irradiance levels were higher in 2014 and 2015, compared to the relative energy contribution at low- and medium light intensities, which were higher in 2011, 2012 and 2013.

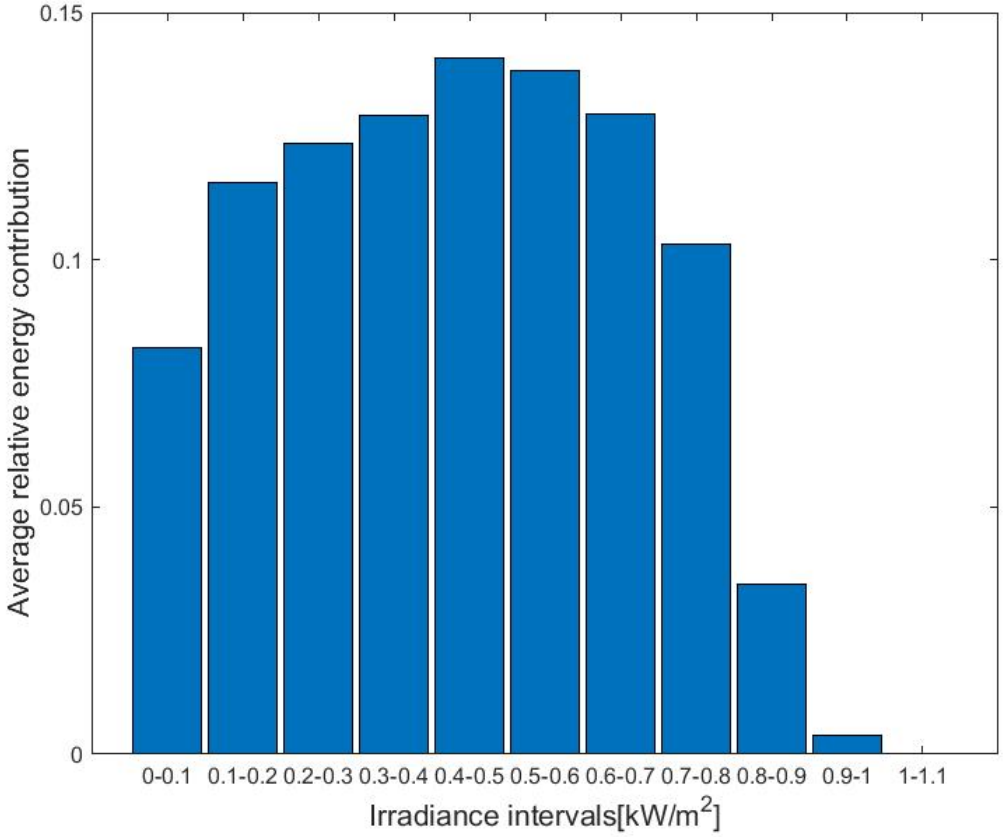

Figure 24: The average relative energy contribution with respect to irradiance levels.

The highest relative energy contribution is achieved at solar irradiance ranging between 400-500 W/m^2, contributing with 14 % of the average energy received during a year. The average relative energy contribution, illustrated in Figure 24, is relatively homogeneously distributed in the interval 0-800 W/m^2 contributing with a total of 96 % of the incoming solar energy. The energy contribution decreases drastically after 800 W/m^2, with only 4 % contribution from light intensities between 800-1100 W/m^2.

The presented data is based on horizontally measured irradiance, meaning the values are not directly applicable for inclined solar modules. By assuming a constant solar module tilt of 40° and the module facing true south, it may be assumed that horizontal light intensity in the interval 700-800 W/m^2 is approximately equivalent to 1000 W/m^2 incident on the tilted module. This value was calculated using the trigonometric relationship cos(40°), and validated with PVsyst [49]. The total average relative energy contribution for this light intensity interval is 14 %. By assuming the above calculation is realistic, the yearly energy production from solar modules installed at locations with similar irradiance conditions as Ås vary greatly from the energy production under STC conditions.

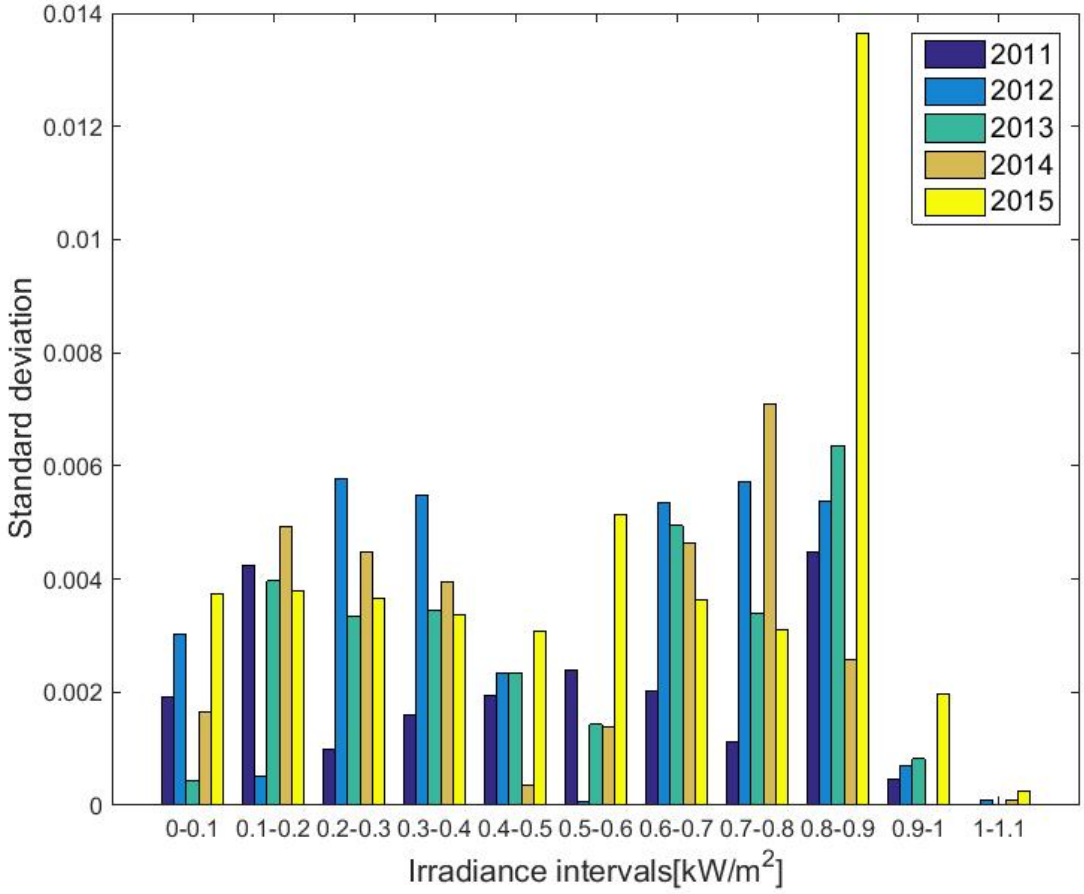

Figure 25: Standard deviation in relative energy contribution for each separate year with respect to the mean relative energy contribution.

The standard deviation, representing the deviation in relative energy contribution for each separate year with respect to the overall mean, is presented in Figure 25. The standard deviation in the irradiance interval 800-900 W/m^2 shows a significantly increased value for the year 2015. This large standard deviation may be a result of longer periods with light intensities in the interval 800-900 W/m^2. The standard deviation in the interval 400-500 W/m^2 is relatively low, which gives further validation of the suggestion that irradiance with this light intensity contributes with the largest share in solar energy.

4.1.2 Relative efficiency with respect to light intensity

The relative efficiencies with respect to irradiance levels for the CIS- and p-Si module were calculated by Eq.(11) section 2.4.3. The results are illustrated in Figure 26. The values implemented in Eq.(11) for the CIS module were obtained using Plot Digitizer to extract the maximum power at different irradiance levels from a plot in the datasheet of the CIS module, see Appendix A. The p-Si module efficiency at different irradiance levels were modelled by Halvard Haug, using the solar cell simulation tool PC1Dmod [50]. The values for both modules are obtained at 25 ℃ and AM 1.5.

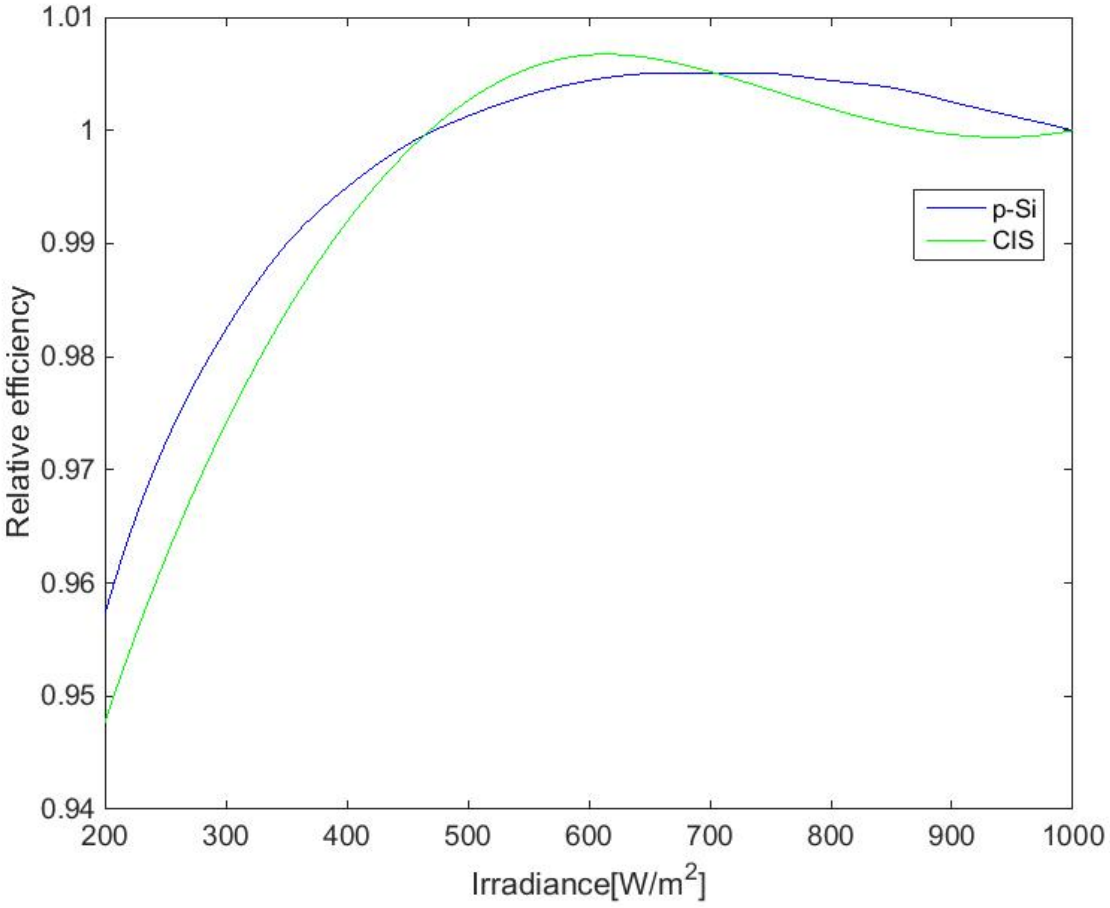

Figure 26: Relative efficiency with respect to irradiance levels, for both CIS- and p-Si module. The presented values are based on data collected at 25℃ and AM 1.5.

Compared to the relative efficiency of the p-Si module, the relative efficiency of the CIS module is higher between 464 W/m^2 and 705 W/m^2. The CIS module performs better at light intensities between 469 W/m^2 and 871 W/m^2, compared to performance at the STC intensity of 1000 W/m^2. Maximum gain occurs between 597 W/m^2 and 629 W/m^2, with a relative efficiency of 1.0067. The p-Si module achieves higher efficiencies than the STC efficiency between 473 W/m^2 and 997 W/m^2. A maximum relative efficiency of 1.0051 is achieved in the interval ranging between 655 W/m^2 and 745 W/m^2.

The gains may be due to relatively high series- and shunt resistance in both modules, which results in the efficiency increasing when light intensity decrease [28, 31]. By observing Figure 26 it may be suggested that the CIS module has a higher series resistance and smaller shunt resistance, compared to the p-Si module. This is based on the observation that the efficiency increases faster as the irradiance decreases, but the efficiency also decreases faster at lower intensities.

In section 4.1.1 it was shown that horizontal irradiance levels ranging in the interval 400-500 W/m^2 contribute with the highest portion of the yearly irradiation at Ås. The average efficiency in this interval is 13.37 % and 15.88 % for the CIS- and p-Si module, respectively. Consequently, the p-Si module

performs better in this light intensity interval, but the average efficiency of both modules is approximately the same as the STC efficiency of each module.

4.1.2.1 Uncertainties

There are uncertainties related to both of the calculated relative efficiencies. The relative efficiencies are not measured, but they are based on datasheet information and modelling. It would have been favorable to supplement the modeling and data sheet information with laboratory measurements. However, laboratory infrastructure suitable for measuring efficiency as a function of light intensity for full size modules was unfortunately not accessible.

The relative efficiencies of the CIS module are based on values obtained in the modules datasheet located in Appendix A. The datasheet presents the I-V and P-V curves at 1000 W/m^2, 800 W/m^2, 600 W/m^2, 400 W/m^2 and 200 W/m^2. Plot Digitizer was used to extract the maximum power output at these five irradiance levels. The maximum power output at every whole numbered irradiance value between 200 W/m^2 and 1000 W/m^2 was obtained by interpolation. Accurately finding the coordinates that match the maximum power is difficult, mostly due to the low resolution of the plot. Consequently, the interpolated values are also inaccurate. A similar curve to the one presented in Figure 26 is shown in Reich *et al*.(2005) [8] for a CIS solar cell, and shows a peak relative efficiency of about 104 % at 800 W/m^2. However, the measurements are performed on a single cell and plotted on a logarithmic scale, making proper comparisons difficult. The relative efficiencies of the p-Si module are based on empirical values implemented in PC1Dmod. A similar relative efficiency curve is presented in previous work [30].

4.1.3 Overall results and discussion

The relative energy contribution at Ås has a maximum value of 14 % in the irradiance interval 400-500 W/m^2. The energy contribution is relatively low in the interval 800-1100 W/m^2, contributing with only 4 % of the yearly solar energy.

The efficiency of both modules is higher than the STC efficiency between 500 W/m^2 and 1000 W/m^2. The reduction in performance is higher for the CIS module at low light intensities ranging between 0-500 W/m^2, which may be a result of a lower shunt resistance than that of the p-Si module. This difference in low light performance has been observed by other authors [8, 51]. The average efficiency in the region 400-500 W/m^2 is 13.37 % and 15.88 %, for the CIS- and p-Si module, respectively. The efficiencies at these light intensities are hence equal to the STC efficiencies of each module.

Implementing irradiance measurements from more than five years would be beneficial. Additional irradiance data would give a more detailed overview of the past irradiance conditions, and a more solid information base for predicting the light conditions in the future. Irradiance data for the period 2006-2010 has also been evaluated and analyzed, but portions of the data was not consistent with the data for the period 2011-2015. The 2006-2010 datasets did not consist of the same amount of measurement values as the 2011-2015 datasets. A total of 52560 irradiance measurements are expected for each year, but the yearly number of measurements concerning 2006-2010 was either lower or higher. The errors would be possible to investigate and correct, given sufficient time and relevant information. This thesis is focusing on the effects of irradiance, and not the verification of measurement data, which is why the data for 2006-2010 is not further investigated and consequently not implemented.

Another important aspect of this analysis is if the irradiance conditions at Ås are comparable to the irradiance conditions in the Nordics in general. By observing the Nordics in Figure 1 section 1.1, it is clear that locations closer to the ocean and further north experience a lower yearly irradiation. Figure 1 illustrates that a large portion of the inland parts of Norway, Sweden and Finland receive irradiation at levels similar to the location of Ås. Consequently, the irradiance conditions presented in this thesis may be a relative good estimation for the irradiance conditions in central regions of the Nordic countries.

4.2 Spectral irradiance data

Spectral irradiance was measured in Grimstad and at Kjeller, using the spectroradiometer described in section 3.1.1. The solar spectra were measured in different light conditions, and for different time periods. This section presents the measured solar spectra with the corresponding average photon energies and spectral factors. The solar spectra are divided into groups based on the light conditions in which the measurements were conducted. Due to a large number of spectral irradiance measurements, the figures presenting the solar spectra during each day contain specifically chosen spectra for different times of the day. A representative spectrum is shown and compared to the standard AM 1.5 spectrum in Figure 27.

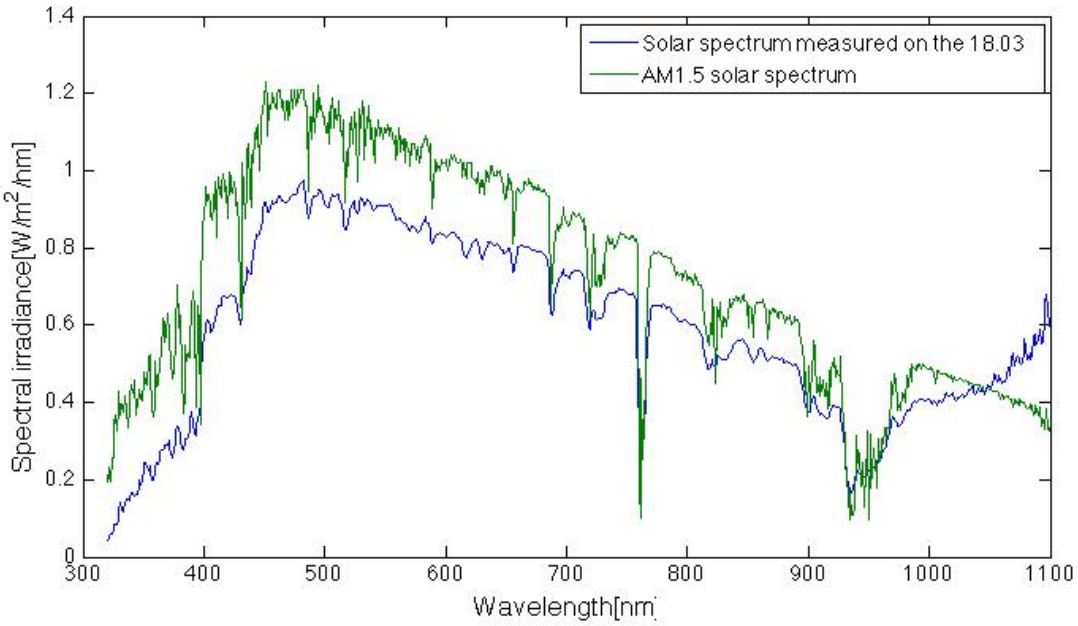

Figure 27: Comparison between a spectral irradiance measurement performed on the 18.03.16 and the standard AM 1.5 solar spectrum.

The two solar spectra mostly follow the same absorption patterns. As stated in section 2.1.2.1 the absorption pattern is dependent on the gaseous composition of the atmosphere. The observable absorption "dips" are sharper in the AM 1.5 spectrum, which is most likely due to the higher smoothing filter applied on measured values conducted with the spectroradiometer PSR-1100F. This is especially evident at short wavelengths where the amplitude of the absorption dips is clearly larger in the AM 1.5 spectrum. There is

also a large deviation in spectral irradiance in this region, which may be a result of higher ozone concentration in the actual atmosphere. The wide absorption dip between 900-1000 nm and the narrow dip between 700-800 nm are examples of absorbance due to water. It appears the concentration of water in the actual atmosphere, at this date, is similar to the modelled atmosphere used to define the AM 1.5 spectrum. The difference in absorbance of other gases is more difficult to observe, due to short absorbance bands and small amplitudes.

The measured spectral irradiance is in general lower than that of the AM 1.5 spectrum. This is most likely due to a high air mass larger than 1.5, which attenuates more of the incoming solar energy and hence the spectral irradiance.

The largest deviation is observable in the region 1000 nm to 1100 nm. There is a possibility that this abnormality is due to a calibration error. The measured spectral irradiance increases drastically at 1000 nm, while the spectral irradiance of the standard spectrum decreases. This abnormality was first discovered when performing measurements in Grimstad. Anne Gerd Imenes and Georgi Hristov Yordanov commented that the calibration in this region may not be sufficient and lead to erroneous measurements conducted with this spectroradiometer. The production company was contacted replied was that the silicon array loses responsivity very quickly above 1000 nm and is the region that greater variation in deviation would be expected to occur. The production company also replied that there is a possibility that the fiber optic may have a few broken cores from use, and that this may affect calibration at the extreme points.

4.2.1 Spectral irradiance in Grimstad

The solar spectra in Grimstad were measured for two separate days in February. Measurements from the 10.02.16 were performed with help from Anne Gerd Imenes and Georgi Hristov Yordanov. Measurements from the 12.02.16 were performed by Anne Gerd Imenes.

4.2.1.1 Overcast

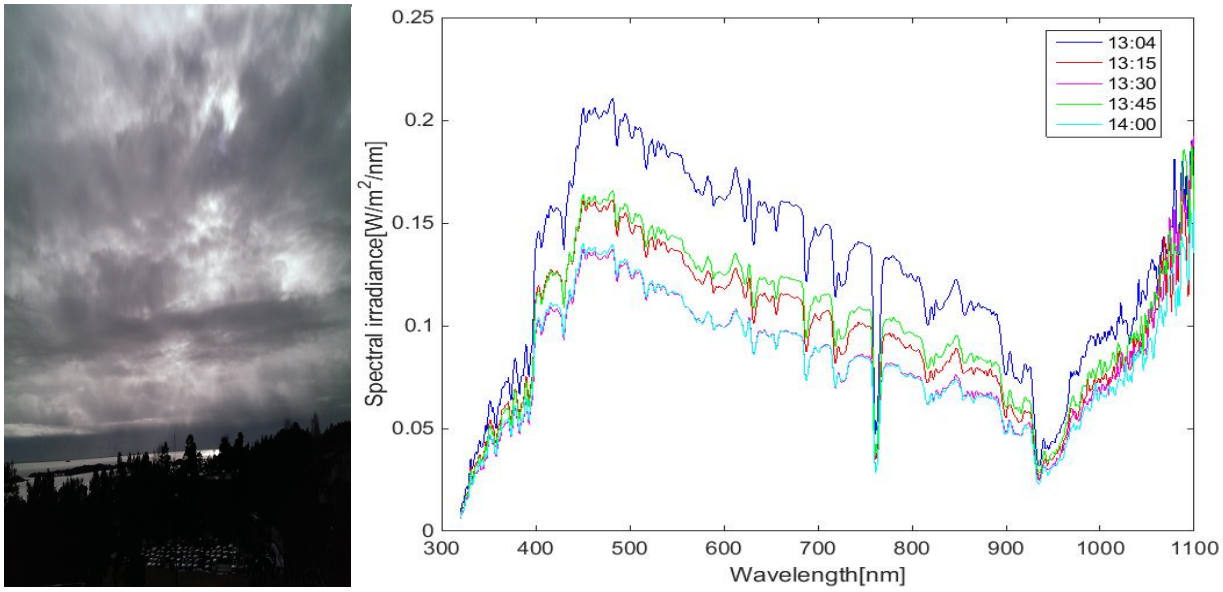

Figure 28: The light conditions (left) and solar spectra (right) in Grimstad on the 10.02.16. The measurements were taken between 13:04 and 14:04. A total of 392 horizontal measurements were conducted in this period.

The left part of Figure 28 shows the diffuse light conditions on the 10.02.16 which were constant during the measurement sequence. The solar spectra in Grimstad on the 10.02.16 are represented on the right side of Figure 28. The two main reasons for the relatively low spectral irradiance are most likely due to the low elevation angle and cloudy conditions. The measurements were only conducted between 13:04 and 14:03, but there is still a large variation between spectra during this time period. This may be a combination of the elevation angle decreasing during the measurement sequence and the varying light transmittance of the cloud cover.

4.2.1.2 Clear sky

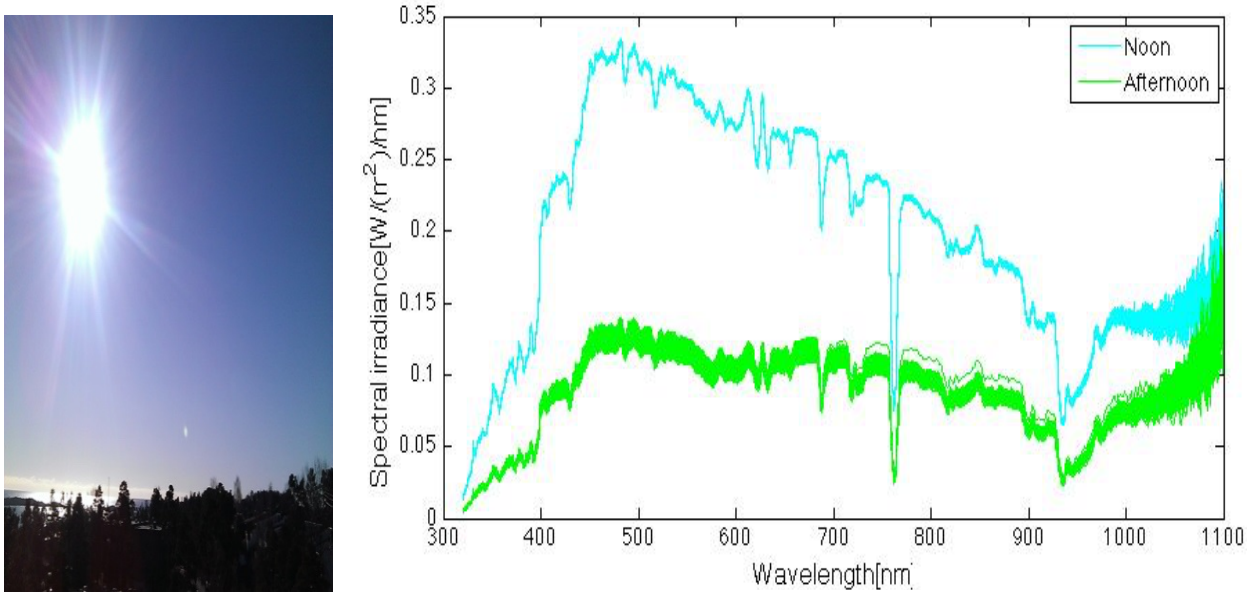

Graph 29: Light conditions (left) and solar spectra (right) in Grimstad on the 12.02.16. The measurements were performed at noon and in the afternoon. The solar spectra at noon were measured between 12:09 and 12:18. The solar spectra in the afternoon were measured between 15:46 and 15:56. A total of 195 horizontal measurements were conducted during these two periods.

The left part of Figure 29 shows the light conditions on the 10.02.16. The solar spectra measured in Grimstad on the 12.02.16 are presented on the right side of Figure 29. The measurements are divided in two time periods; at noon and in the afternoon. The measurements conducted between 12:18 and 15:46 were measured with a diffuser tilted at an angle of 39 degrees. These measurements are hence not included in Figure 29, which only contains horizontal measurements. The spectral irradiance is greater at noon than in the afternoon, which is a result of the elevation angle decreasing after noon.

4.2.2 Average photon energy

$$APE[eV] = \frac{1}{q}\left(\frac{\int E(\lambda)d\lambda}{\int \phi(\lambda)d\lambda}\right) \quad (3)$$

The APE for every spectral measurement was calculated by Eq.(3) section 2.1.3. The calculated APE value of the horizontal AM 1.5 solar spectrum, for the wavelength interval 320-1100 nm, is 1.725 eV.

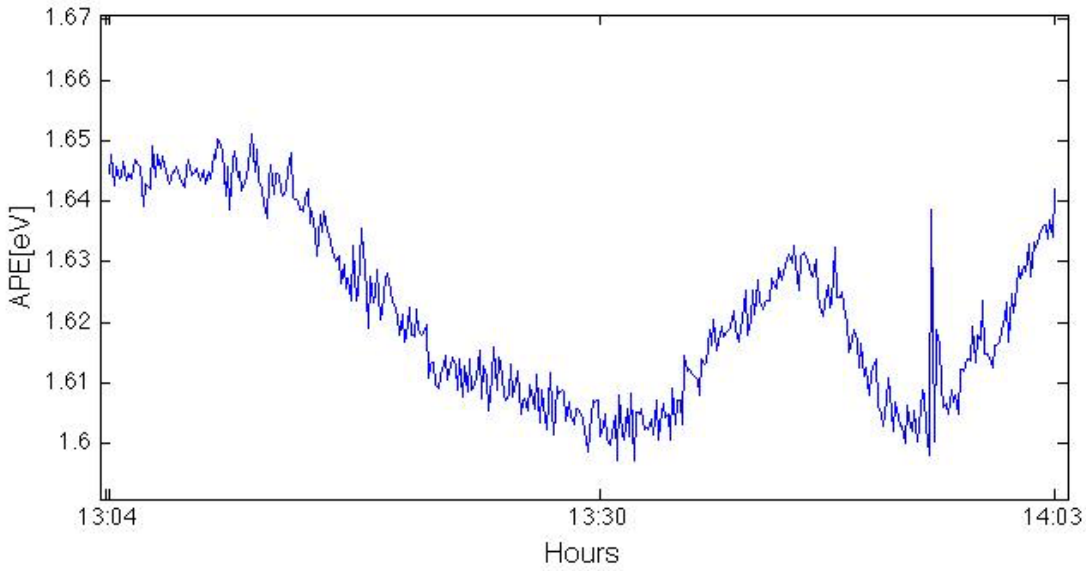

Figure 30: Average photon energy between 13:04 and 14:03 in Grimstad on the 10.02.16.

The average photon energy during the measurement sequence on the 10.02.16 is illustrated in Figure 30. The APE varies between 1.65eV and 1.60eV, which implies a red rich spectrum. A relatively low APE may be expected from the low elevation angle of the Sun and the correspondingly high air mass. As stated in section 2.1.3, the high air mass increases Rayleigh scattering of short wavelengths, which decreases APE.

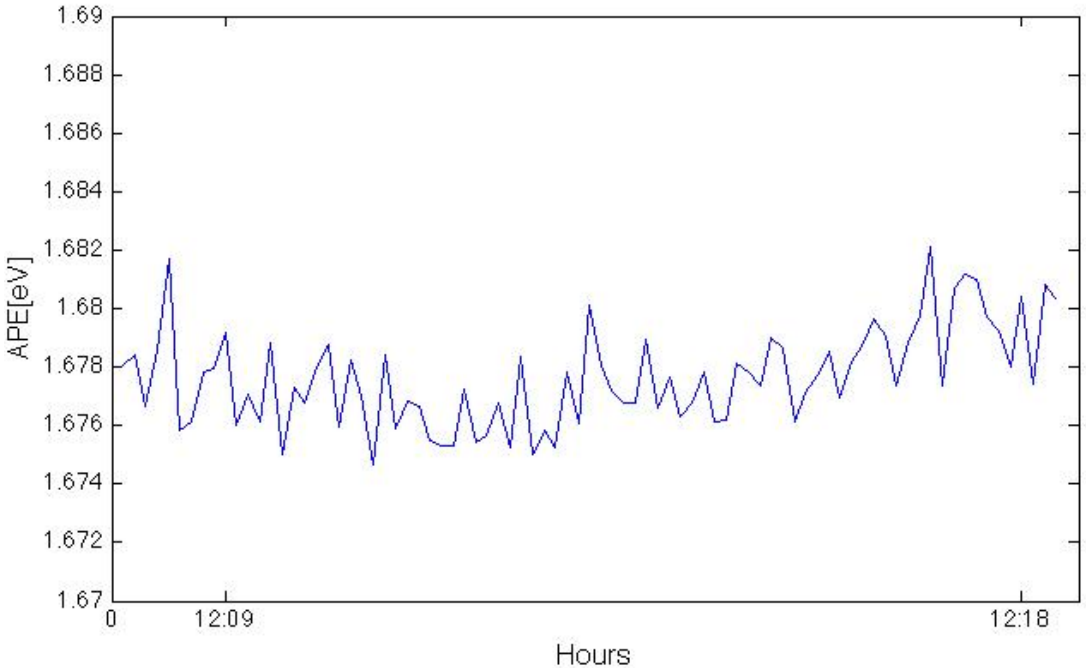

Figure 31: Average photon energy between 12:09 and 12:18 in Grimstad on the 12.02.16.

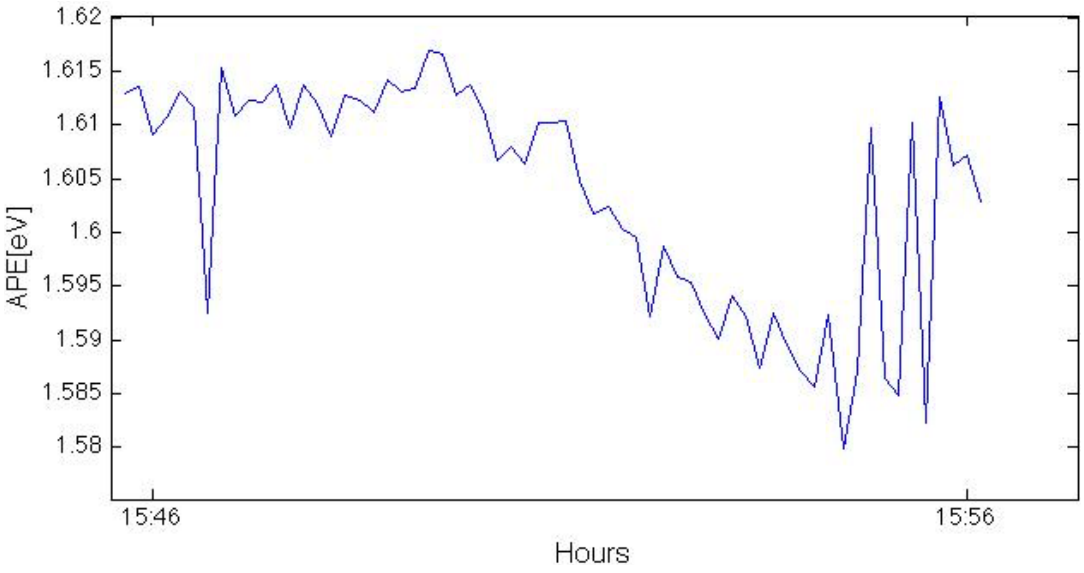

Figure 32: Average photon energy between 15:46 and 15:56 in Grimstad on the 12.02.16.

The average photon energy at noon and in the afternoon on the 12.02.16 is presented in Figure 31 and Figure 32, respectively. Around noon, APE varies between 1.682 eV and 1.675 eV, and is hence implying a stable red rich spectrum. The APE is even lower in the afternoon, varying between 1.617 eV and 1.580 eV. The difference in APE is most likely due to higher air mass in the afternoon, which causes a red shift in the spectral irradiance distribution.

The APE values at noon on the 12.02.16 are especially stable, but small variations are still observable. The light conditions were constant throughout the day, with no clouds on the sky. The variations in APE are hence not due to changing light conditions. The spectroradiometer uncertainty of 3.2 % at 350 nm and 900 nm, and 3.1 % at 654.6 nm, may be the reason for the noise observed in the presented APE values.

4.2.2.1 Uncertainties and measurement errors

As stated earlier, the measurement setup at Kjeller and Grimstad is different. The diffuser setup might result in inconsistent measurements. Both the tilted and horizontal setups were only to be applied for a short time period, and it was not enough time to design a stable fastening system in order to improve measurement repeatability.

4.2.3 Spectral irradiance at Kjeller

The spectral irradiance at Kjeller was measured for six days in March 2016. The majority of the measurements were conducted around noon. The measurements were conducted with help from Lenny Enstrom, Bent Thomassen and Josefine Selj. The measurements were performed in different light conditions and the measurement periods varied.

4.2.3.1 Overcast conditions

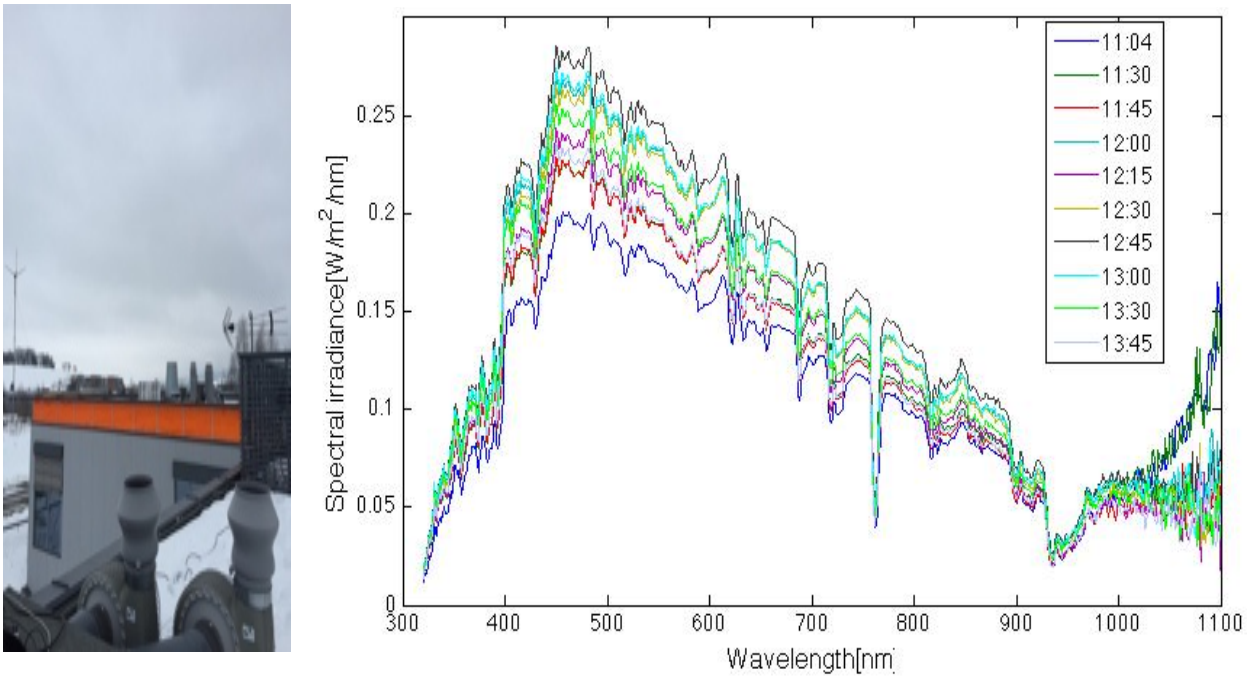

Figure 33: Light conditions (left) and solar spectra (right) on the 10.03.16. Spectral irradiance measurements were performed between 11:04 and 13:45. A total of 963 horizontal measurements were conducted in this period.

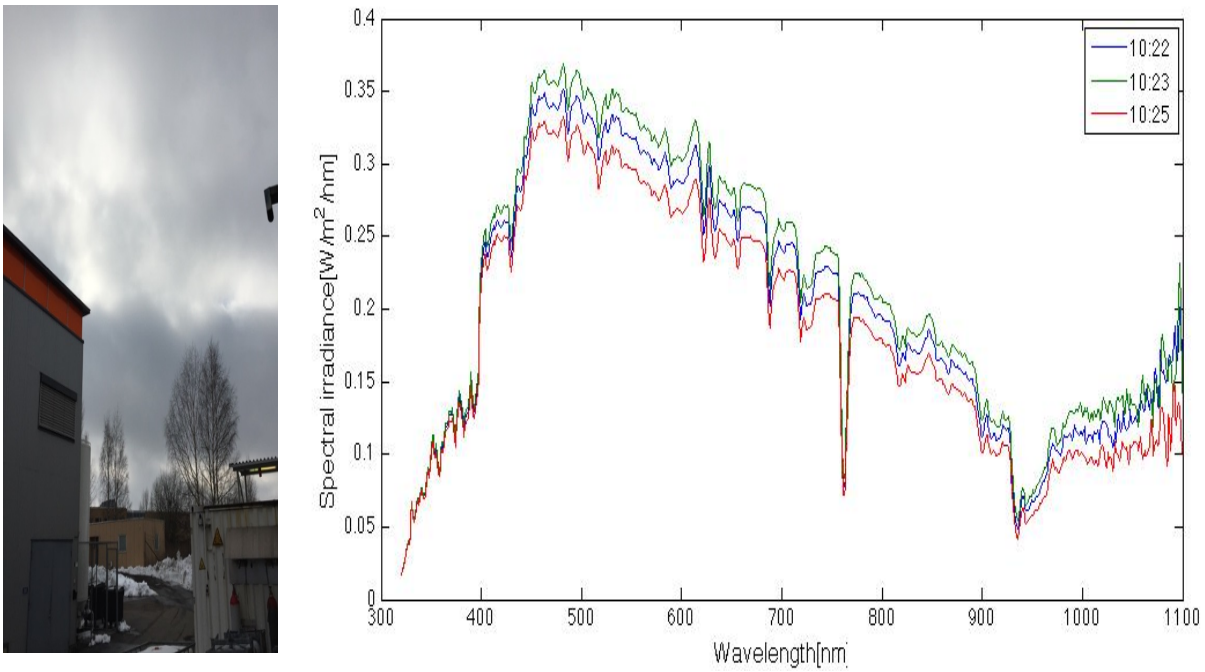

Figure 34: Light conditions (left) and solar spectra (right) on the 11.03.16. Spectral irradiance measurements were performed between 10:22 and 10:25. A total of 22 horizontal measurements were conducted in this period.

The solar spectra in overcast conditions were measured on the 10.03.16 and 11.03.16. The light conditions are represented on the left side of Figure 33 and Figure 34. The light conditions on the 10.03.16 were more constant, compared to the 11.03.16 which shifted during the day. Higher winds on the 11.03.16 resulted in periods with more direct sunlight.

The right side of Figure 33 and Figure 34 represents the solar spectra measured on the 10.03.16 and 11.03.16, respectively. The spectral irradiance measurements on the 10.03.16 were conducted over a longer time period, compared to the measurements from the following day. The measurements from 11.03.16 were collected between 10:22 and 10:25. This short measurement sequence was due to a measurement error. Hence, Figure 34 does not give information about the spectral irradiance around noon or in the afternoon. The spectral irradiance is still higher between 10:22 and 10:25, compared to the maximum spectral irradiance on the 10.03.16. This is probably due to variable light conditions on the 11.03.16.

4.2.3.2 Partly sunny

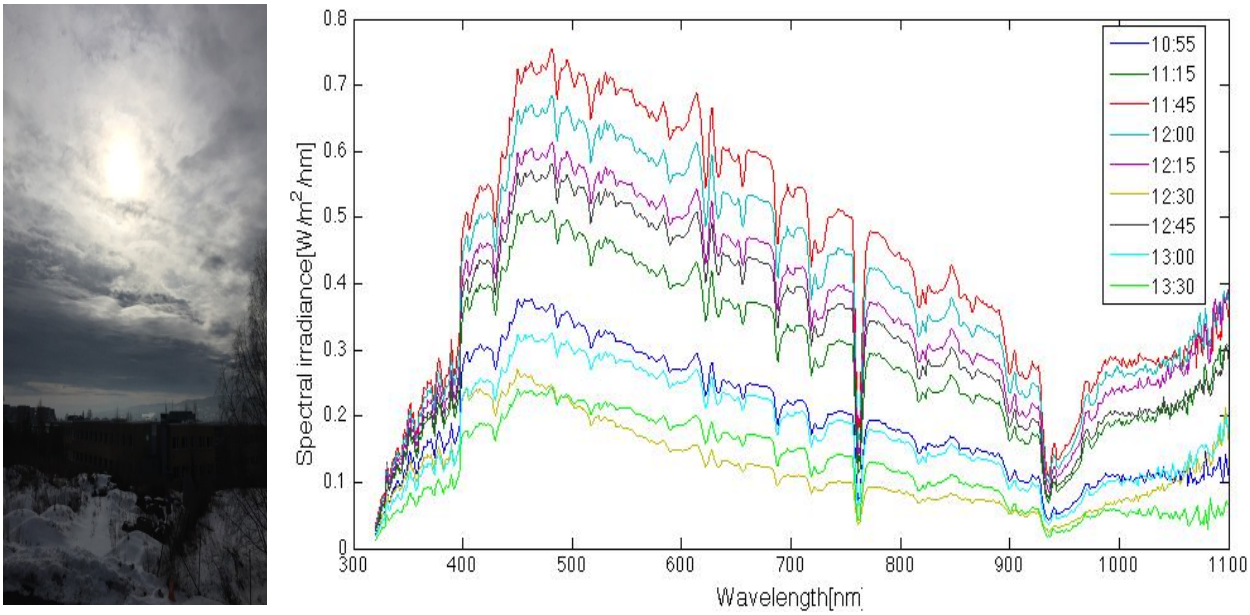

Figure 35: Light conditions (left) and solar spectra (right) on the 09.03.16. Spectral irradiance measurements were performed between 10:55 and 13:42. A total of 942 horizontal measurements were conducted in this period.

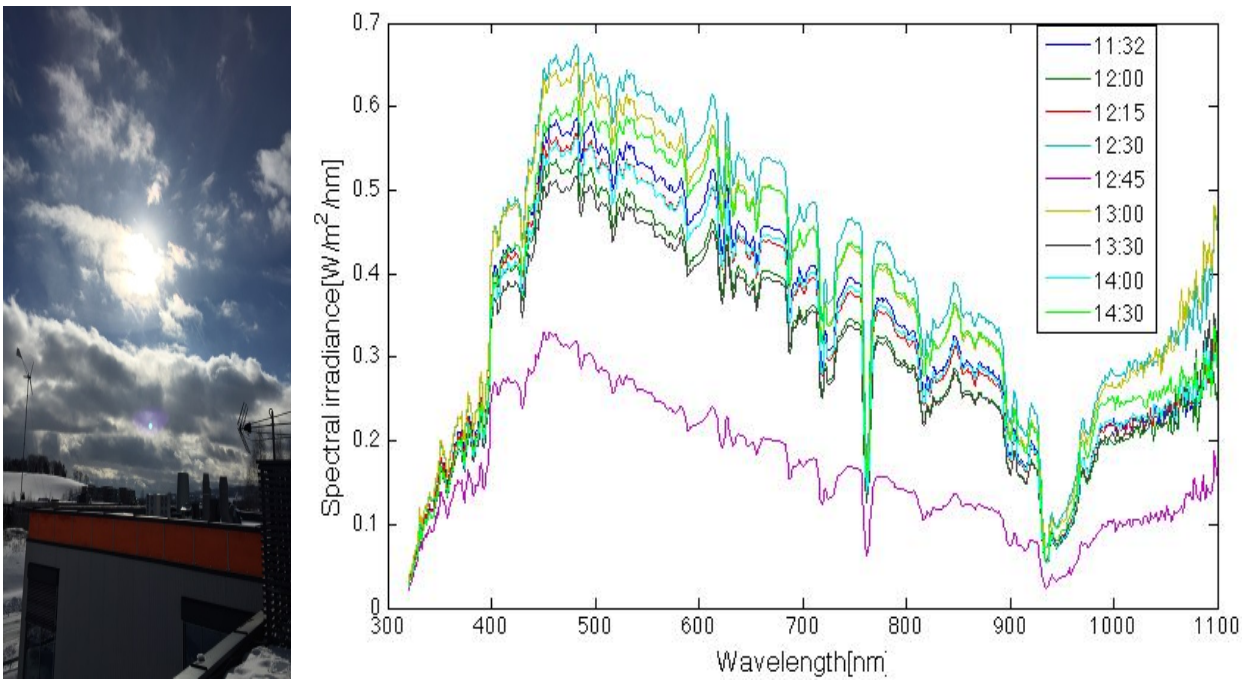

Figure 36: Light conditions (left) and solar spectra (right) on the 14.03.16. Spectral irradiance measurements were performed between 11:32 and 14:34. A total of 1089 horizontal measurements were conducted in this period.

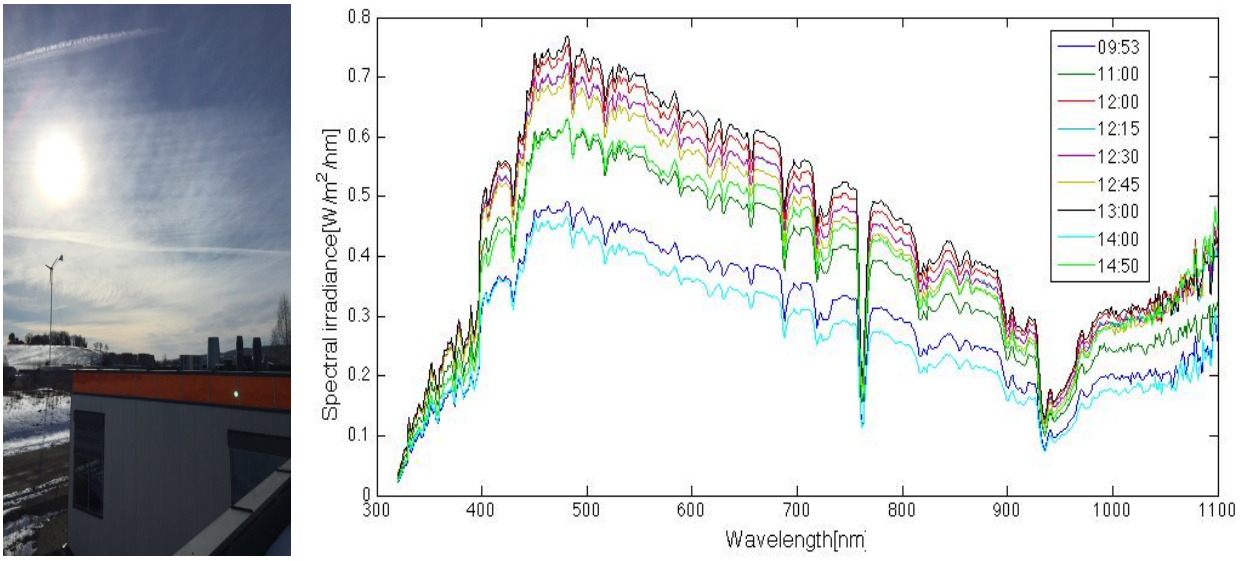

Graph 37: Light conditions (left) and solar spectra (right) on the 18.03.16. Spectral irradiance measurements were performed between 09:53 and 14:50. A total of 1769 horizontal measurements were conducted in this period.

Three of the measurement sequences were performed in partly sunny conditions. The light conditions on the 09.03.16, 14.03.16 and 18.03.16 are presented on left side of Figure 35, 36 and 37, respectively. The light conditions on the 18.03.16 were similar to clear sky conditions, but it varied during the day and the cirrus clouds, shown in in the left of Figure 37, covered the Sun in some periods.

The spectral irradiance measurements for the 09.03.16, 14.03.16 and 18.03.16 are presented on the right side in Figure 35, 36 and 37, respectively. These three measurement sequences all consist of a large number of measurements, all conducted before, during and after noon. The solar spectrum on the 09.03.16 and the 14.03.16 are both peaking around 7.5 W/m^2nm, which may be a result of similar light conditions. The solar spectrum on the 18.03.16 peaks at a spectral irradiance value close to 1.0 W/m^2nm. This high value is most likely due to periods with clear sky.

It started to snow at the end of the measuring sequence on the 10.03.16. The snow did not accumulate on the diffuser, and the snow had consequently minimal effect on the last measurements. The suspended snow particles may also have attenuated portions of the incoming light, but the effects on the measurements are assumed to be negligible.

4.2.3.3 Clear sky

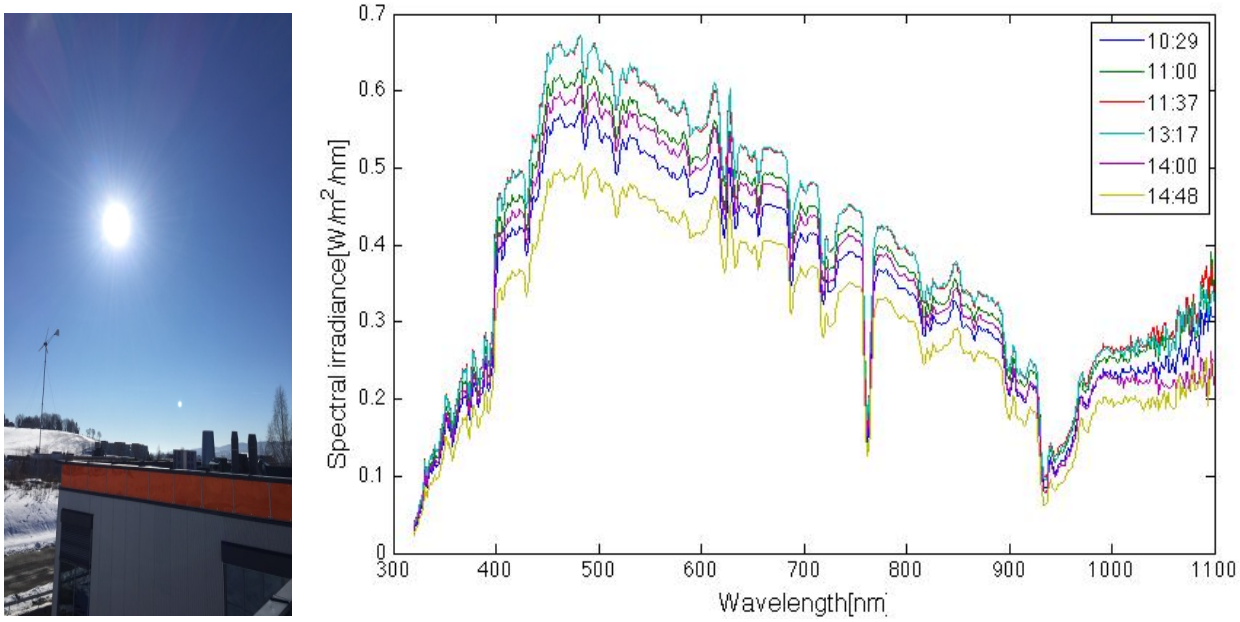

Figure 38: Light conditions (left) and solar spectra (right) on the 16.03.16. Spectral irradiance measurements were performed in two sequences: The first between 10:29 and 11:37, and the second between 13:17 and 14:48. A total of 953 horizontal measurements were conducted during the two periods.

At Kjeller, the only clear sky measurement sequence was conducted on the 16.03.16. The light conditions on the 16.03.16 are presented on the left in Figure 38. The light conditions shown were constant throughout the day. The solar spectra on the 16.03.16 are illustrated on the right in Figure 38. Due to a measurement error, the spectral irradiance between 11:37 and 13:17 was not measured. Hence why the spectra in Figure 38 is peaking at a value under 0.7 W/m^2nm, and not a higher value, as would be expected when compared to measurements from 18.03.16.

4.2.3.4 Average photon energy

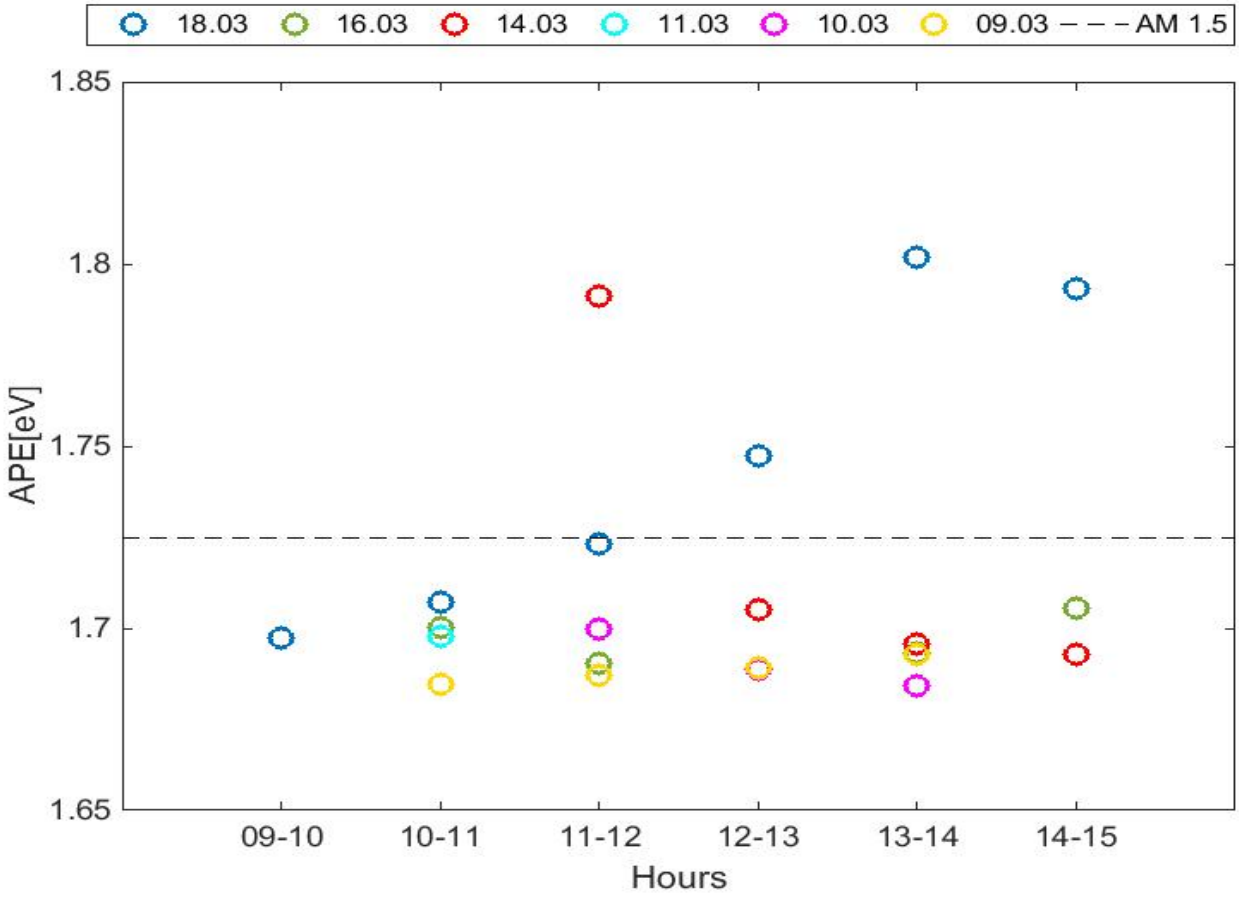

Figure 39: The average photon energy of the solar spectra measured in March. The figure illustrates the change in APE during the hours of the day. The dotted line symbolizes the APE of the AM 1.5 solar spectrum. The presented APE values are mean values based on the measurements conducted during each hour.

Figure 39 shows the variation in APE during the different days. APE calculated by using Eq.(3). Recall that the number of measurements varies from day to day, and it is consequently difficult to observe the change in APE for some days. The APE for the 11.03.16 is an example of this, with APE only being based on spectral measurements collected between 10:22 and 10:25. This APE value, symbolized as a cyan colored circle, is fairly close to the APE of the AM 1.5 spectrum. On the contrary, measurements conducted on the 18.03.16 clearly show how the APE varies during the day. The APE on the 18.03.16 increases during the day. Hence, the blue richness of the spectrum increases, which may be a result of increased cloud coverage and elevation angle increasing until noon. The opposite occurs on the 14.03.16. The APE between 11:00 and 12:00 represents a blue rich spectrum, but between 14:00 and 15:00 the APE drops down to a value lower than 1.725 eV. The decrease in APE is expected from reduced cloud coverage and decreasing elevation angles. Clouds absorb long waved radiation effectively and increase the transmission of short waved radiation. Consequently, the APE decreases when the cloud coverage is reduced. The other measurement sequences do not experience the same drastic change in the APE, and have values lower than the APE corresponding to the AM 1.5 spectrum.

4.2.3.5 Uncertainties and measurement errors

As stated earlier, the measurement sequences on the 11.03.16 and 16.03.16 were disrupted due to technical difficulties. The reason for the disruption is not known. The physical properties of the measurement setup at Kjeller may have resulted in inconsistent measurements. The instrument's position was for example changed for each measurement sequence, which increased the measurement uncertainty.

4.2.4 Comparison with the AM 1.5 solar spectrum

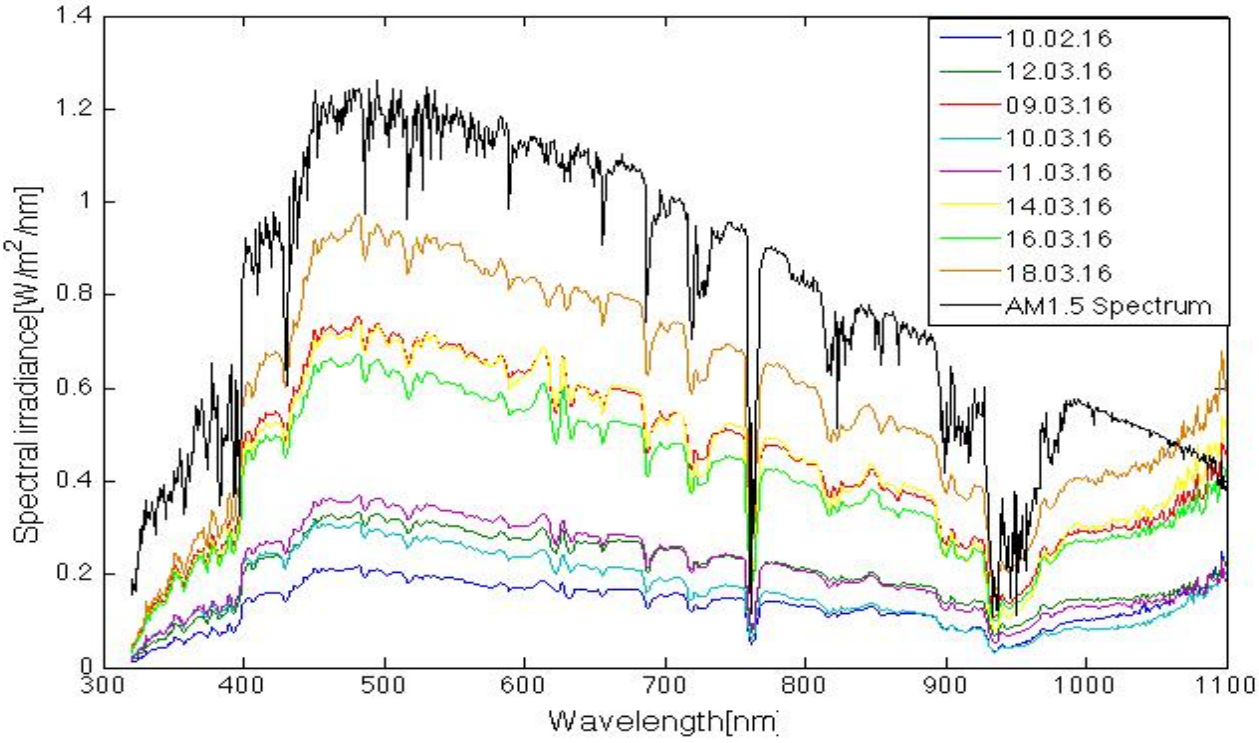

Figure 40: Measured solar spectra at Kjeller and in Grimstad vs the AM 1.5 solar spectrum. The solar spectra presented are the ones with the highest spectral irradiance from each sequence.

Figure 40 shows the AM 1.5 solar spectrum vs the maximum irradiance solar spectra from each measurement day. A full month separate the measurements conducted at Kjeller and Grimstad, but it is still interesting to see how the measured spectra differ from the solar spectrum utilized at STC. This implies that the majority of the solar spectra presented are either occurring around noon or at times with less clouds. By observing Figure 40 it appears that the spectrum measured on the 18.03.16 has peak spectral irradiance close to the level of the AM 1.5 spectrum.

Although the measurements are made with different degrees of cloud coverage, Figure 40 clearly illustrates how the spectral irradiance increases between February and March. It is clear that the measured spectral irradiance is lower in February compared to the measured spectral in March. This is true for both clear and cloudy days, and corresponds naturally with the Sun's increasing elevation angle. Solar spectra

measured on the 10.02.16 and 10.03.16 were both measured in diffuse light conditions, and it appears that the spectral irradiance was higher on the 10.03.16.

4.2.5 Modelling the solar spectrum

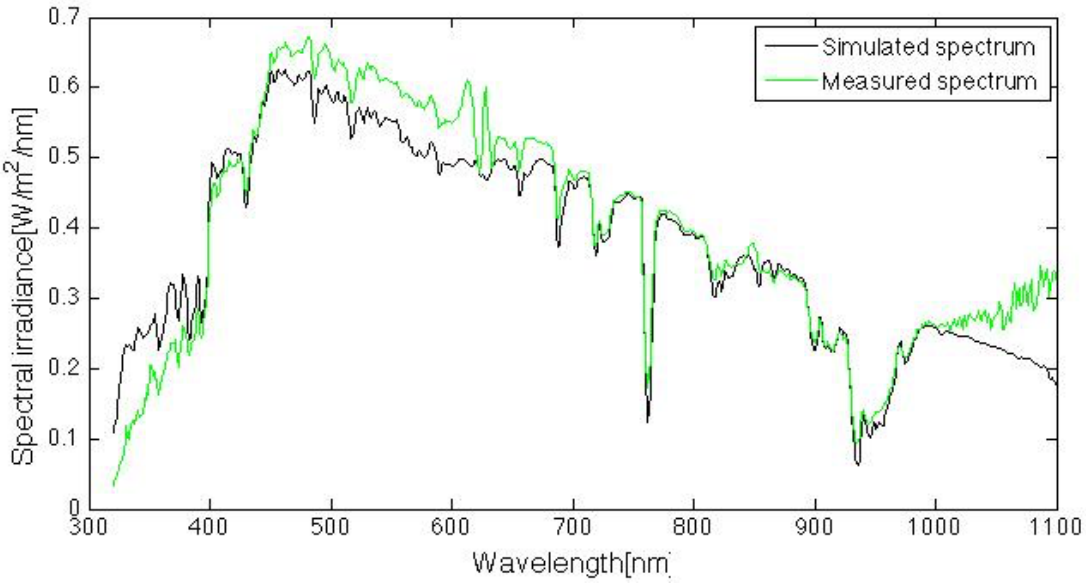

Figure 41: The simulated and measured solar spectrum on the 16.03.16 at 13:17.

The comparison between the measured- and modelled solar spectrum is presented in Figure 41. The first step of modelling the spectrum involved establishing a model that generated a solar spectrum similar to the one measured on the 16.03.16. This specific solar spectrum was chosen because it was measured on a clear day, and SMARTS only models clear sky spectra. The computer program SMARTS was used to model the clear sky solar spectra in both Grimstad and at Kjeller.

The clear sky solar spectrum measured at noon in Grimstad was the first spectrum that was compared with different modelled spectra produced with SMARTS. At that time, little atmospheric data was collected and technical difficulties with the User Interface slowed down the modelling process. This resulted in significant large deviations between the modelled and measured spectrum. The comparisons were performed with clear sky measurements from Kjeller, and it was decided that only spectral measurements from Kjeller were to be used in the modelling due to smaller observable deviations between modelled and measured values. After acquiring more knowledge about the FORTRAN code, and collecting a large amount of information concerning the atmospheric composition at different locations in Norway, the modelling of the solar spectrum on the 16.03.16 was performed with greater accuracy. The comparison still showed significant deviations in different wavelength regions.

The fact that SMARTS is not able to model all sky spectra, resulted in no further modelling. The introduction of clouds in the modelled atmosphere requires extensive detailed data about the different cloud types, making the modelling process more complex [42].

4.2.5.1 Comparison between simulated and measured solar spectrum

There are three wavelength intervals in which the modelled spectrum shows large deviation in comparison with the measured spectrum: 320-395 nm, 450-685 nm and 1000-1100 nm. The deviation in the 320-395 nm interval is due to the model overestimating the spectral irradiance in this portion of the spectrum. The reason for this overestimation is most likely due to a difference in the absorption of the gases in the modeled atmosphere. As shown in Table 4 Appendix B, there are several gases which absorb in this wavelength interval: O_3, H_2O_2, NO_2, HONO, HNO_3, and HCHO. Based on these gases only O_3, HNO_3 and NO_2 are available to manipulate in SMARTS. Ozone levels have been measured at the University of Oslo between 1979 and 1989, and during 2014 [52]. Mean ozone levels for the two periods 1979-1989 and 2014, are approximately 400 DU and 350 DU, respectively. The up-to-date ozone map of the Arctic region simulated by NASA Ozone Watch (http://ozonewatch.gsfc.nasa.gov), shows ozone levels close to 350 DU in South-East Norway. A value of 0.350 atm-cm was consequently implemented in the SMARTS model. No data was found concerning the atmospheric concentration of HNO_3 and NO_2 in the atmosphere near Kjeller, and was hence not implemented in the model.

Measurement errors may also have led to the deviation in the 320-395 nm interval. Further investigation of other measurements shows the same behavior, implying that the spectroradiometer is not functioning properly at this wavelength band. The production company suggested that there might be something wrong with the fiber optic cable, which would affect measurements at the highest and shortest wavelengths.

The deviation in the second region, 450-685 nm, might also be a result of inaccurate gas absorption in the modeled atmosphere. As shown in Table 5 Appendix B, atmospheric gases corresponding to O_3, NO_2, NO_3, O_2, H_2O are all absorbing light in this wavelength interval. The concentration of H_2O is based on the relative humidity, which was 82 % on the 16.03.16 at Kjeller. As mentioned above, an ozone level of 0.350 atm-cm was used in the model. The concentration of O_2 is not possible to adjust in SMARTS. NO_2 and NO_3 concentrations in the vicinity of Kjeller have not been found. Due to an absence of gas concentration measurement data, the standard gas composition corresponding to the reference atmosphere Sub-Arctic Winter was implemented in the model.

The deviation in the third wavelength interval is due to the possible calibration error of the spectroradiometer. The same deviation has been observed with other modeled spectra. It appears as if the calibration error between 1000 nm and 1100 nm results in abnormally high spectral irradiance.

A proper model of the solar spectrum at a specific time and place requires input values measured at that exact time and place. The majority of the input values were based on up-to-date values measured close to the location of the measuring station at Kjeller. Turbidity is an important input factor which had not been measured in the vicinity of Kjeller. Turbidity measurements have been performed at Birkenes, located in southern Norway, close to the coast. The turbidity value implemented in SMARTS was manipulated to achieve low deviation, but it was done well within limits based on measurements performed at Birkenes [53]. Turbidity corresponding to an Angstrom Coefficient of 0.69 resulted in the smallest observable

deviation. The atmospheric composition of aerosols at Kjeller and Birkenes is most likely different from each other, and the turbidity implemented in the model might not be representative for Kjeller.

4.2.6 Spectral effects

The spectral effects, based on all the measured solar spectra, are presented as the spectral factor. The spectral factor for every measurement sequence was calculated by using Eq.(12) section 2.5.1. The correlation between spectral factor and average photon energy is also analyzed.

$$SF = \frac{\int E(\lambda)SR(\lambda)d\lambda \cdot \int E_{AM1.5}(\lambda)d\lambda}{\int E_{AM1.5}(\lambda)SR(\lambda)d\lambda \cdot \int E(\lambda)d\lambda} \quad (12)$$

4.2.6.1 Spectral factor

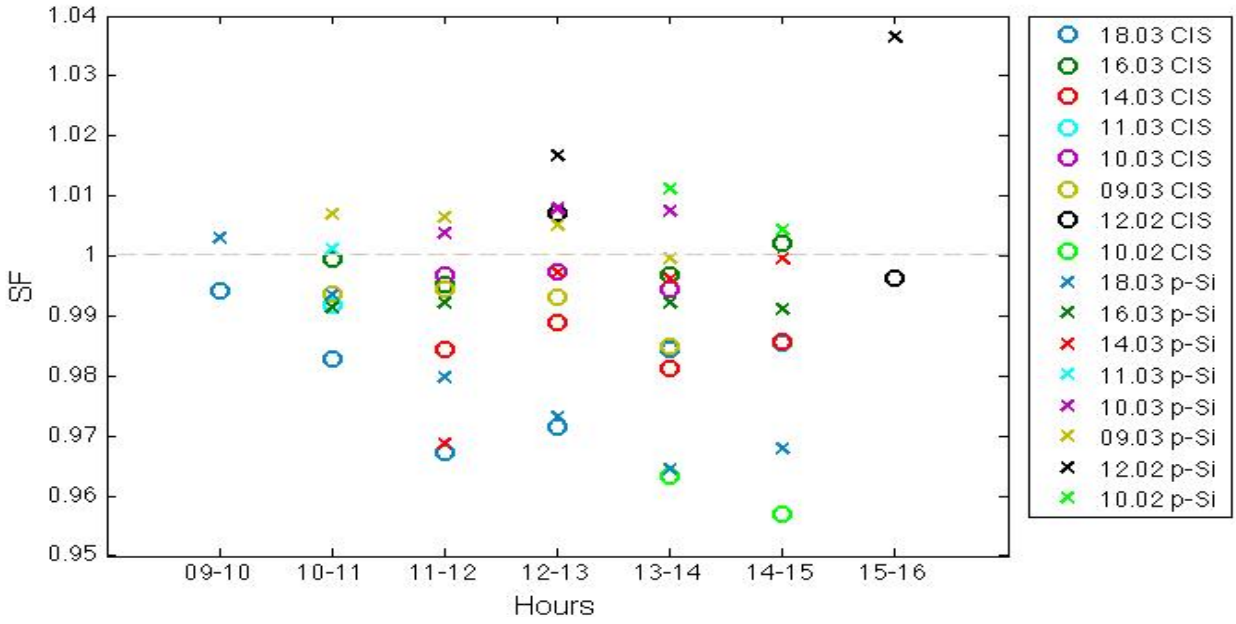

Figure 42: The daily variation in spectral factor for every measurement sequence. The circles symbolize the spectral factor based on the spectral response of the CIS module. The crosses symbolize the spectral factor based on the spectral response of the p-Si module. The presented spectral factor values are mean values based on measurements conducted during each hour.

Figure 22 shows how the spectral factor, for both the CIS- and the p-Si module, varies during the measurement days. By observing Figure 42, it appears that the spectral factor is at most times higher for the p-Si module compared with the CIS module. The highest spectral gain is achieved for the p-Si module on the 12.02.16 between 15:00 and 16:00, with a SF equal to 1.065.

The largest difference in SF for the CIS- and p-Si module occurred on the 10.02.16, with a difference of 4.5 percentage points in the period 13:00-15:00. During these two hours, the p-Si module performs better under the measured spectra in comparison with the performance under the AM 1.5 spectrum, with SF

values of 1.011 and 1.004. The opposite is true for the CIS module which has SF values of 0.963 and 0.957.

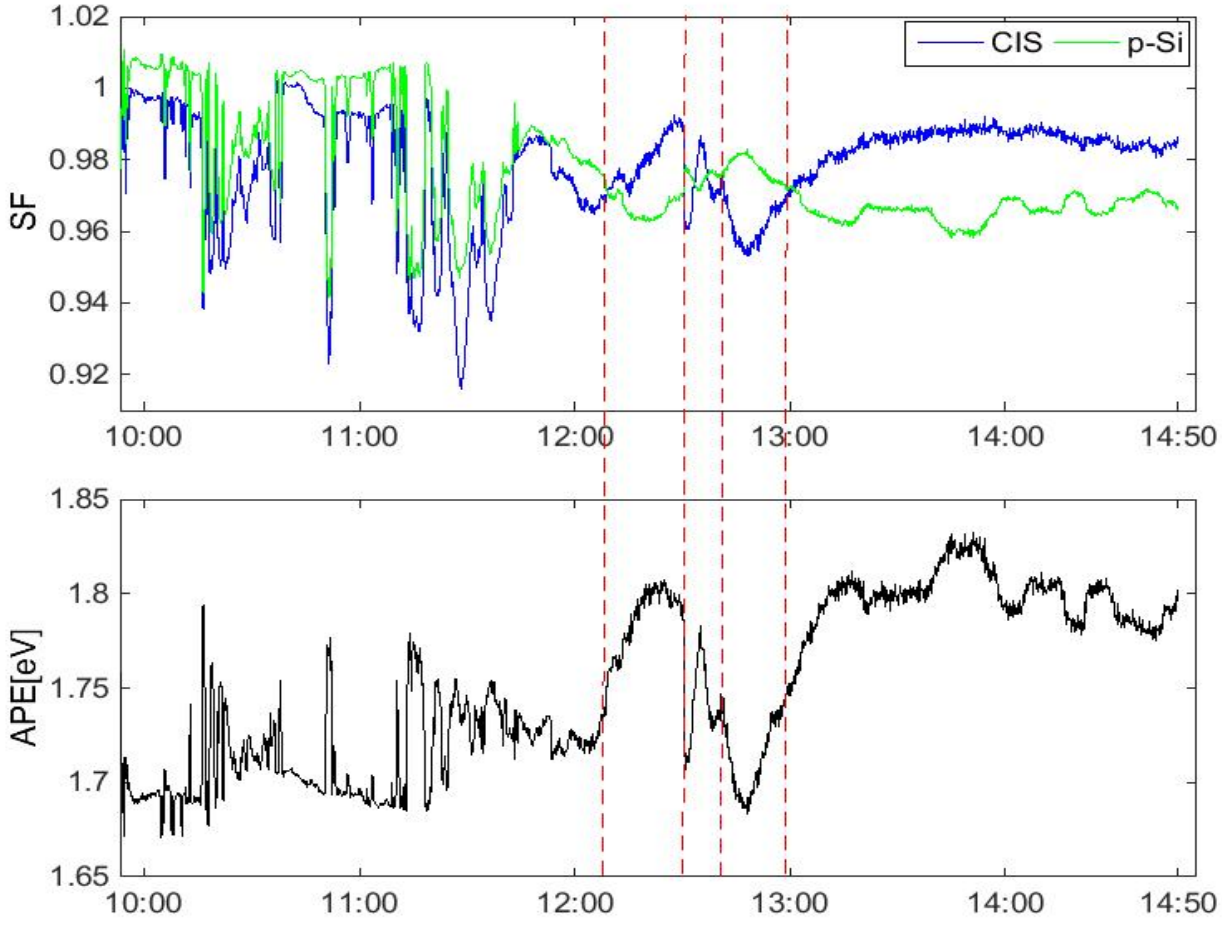

Figure 43: The combined figures show the correlation between APE and SF. The upper graph shows how the spectral factor for both the CIS- and p-Si module varies during the 18.03.16. The lower graph shows the average photon energy during the 18.03.16. The red lines indicate some of the regions when the SF of the modules decreases or increases.

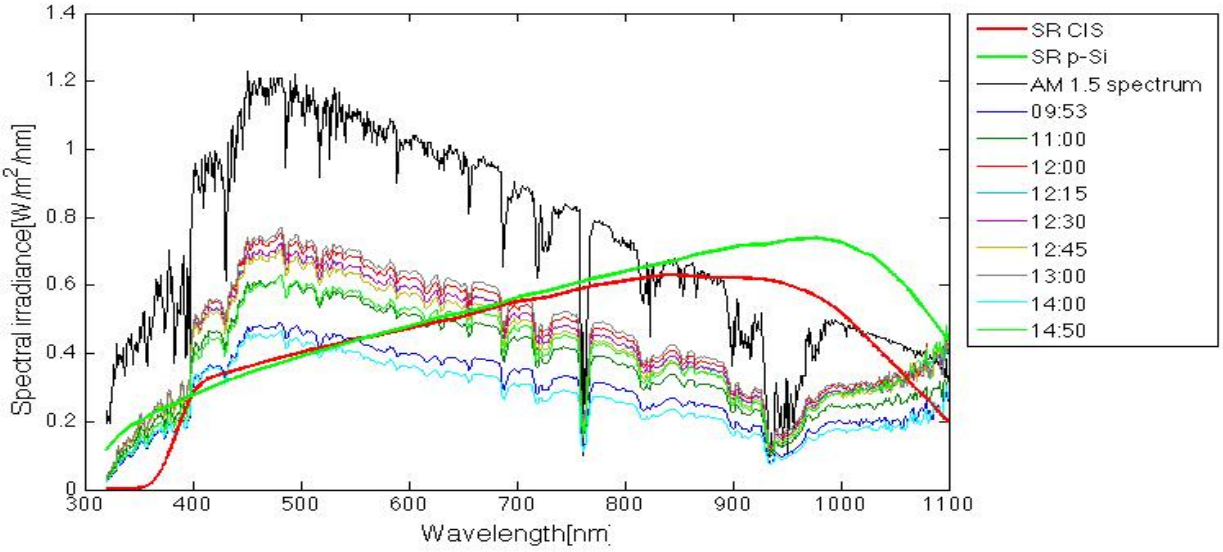

Figure 44: The spectral response of the CIS- and p-Si module compared with solar spectra on the 18.03.16 and the AM 1.5 spectrum.

Another important factor, which might explain the difference in spectral factor, is the correlation between spectral factor and average photon energy. Figure 43 shows the correlation between SF and APE during 18.03.16, which was the measurement day with the highest APE values and largest variations. As shown earlier in in Figure 42, for some periods of the day the SF for the CIS is higher than the SF of p-Si. By focusing on the SF and APE after 12:00, it appears that the SF for the CIS module increases in accordance with APE. The SF for the p-Si is on the contrary increasing when APE decreases. It also appears that APE values below 1.725 eV results in a higher SF for the p-Si module, and vice versa for the CIS module.

Figure 44 presents the different spectral responses of the two photovoltaic technologies. The spectral responses are plotted together with solar spectra on the 18.03.16 and the AM 1.5 spectrum. Between 400 nm and 800 nm, the spectral response is more or less the same. At wavelengths shorter than 400 nm and larger than 800 nm the spectral response of the p-Si module is higher than the CIS module. This results in the p-Si being able to exploit more of the incoming solar energy in these wavelength regions. This is for example illustrated in Figure 44, between 1000 nm and 1100 nm. In this specific region the spectral irradiance on the 18.03.16 and in the AM 1.5 spectrum is low enough to be exploited by the p-Si module, but not by the CIS module. This may explain the behavior shown in Figure 43.

This also supports the large variation in spectral factor values from measurements conducted in February. APE values from 10.02.16 and in the afternoon on the 12.02.16 were all below 1.725 eV, and the spectral factors for the p-Si module were constantly higher than for the CIS module. Consequently, the CIS module may perform better under a blue rich spectrum compared to the p-Si module, which may perform better under a red rich spectrum.

4.2.6.2 Uncertainty

The spectral response of the p-Si module is not based on the IBC module. The spectral response is based on values extracted from the EQE curve of a Trina Solar p-Si module [54]. The response curve was

created by interpolation between the values extracted by the program Plot Digitizer. The low resolution of the EQE plot resulted in an inaccurate interpolation, and the spectral response is consequently not completely correct. The same program was used to extract values from the plotted EQE curve of the CIS module and produce the spectral response.

4.2.7 Overall discussion

The spectral irradiance distributions and APE values presented for the different days in February and March are highly correlated with the air mass. The air mass decreased during the total measurement period, which in general resulted in higher spectral irradiance values and higher APE values. This correlation between air mass and the spectral irradiance distribution is also observed by other authors [17, 19].

The spectral factor calculated for the two modules in different solar spectra implies that the p-Si module performs better in red rich spectra, and the CIS module performs better in blue rich spectra. Similar results concerning the correlation between low APE and p-Si performance have been presented in previous work [55-57]. The performance of the CIS module under a blue rich spectrum has been analyzed by other authors, but the results varies. Tadeusz *et al.*(2003) [27] stated that the CIS showed a 2 % increase in efficiency over the autumn and winter period, and suggested that this may be due to the CIS performing better at high air mass, and hence low APE. Kenny *et al.*(2006) [55] presents calculated spectral factors for a CIS module that increases with a decrease in air mass. Different CIS modules with different spectral responses may be the reason why these results differ. As mentioned earlier, the spectral response implemented in this thesis was not directly obtained from the datasheet and spectral factor values may therefore be inaccurate. The difference in spectral factor for the CIS- and p-Si module is still relatively large and should be an important factor in the procedure of planning future photovoltaics installations in the Nordics.

If there is a calibration error in the 1000-1100 nm region, the calculated average photon energy will be affected. The abnormally high intensities after 1000 nm result in lower average photon energy. This is due to the fact that photons in this long waved region have less energy compared with the incoming photons at shorter wavelengths. The calculated APE values based on the measured spectra may consequently be lower than actual values. The comparison of the APE of the standard spectrum and that of measured spectra may therefore not be accurate.

The possible calibration error may also affect the spectral factor of both modules. The unnatural spectral irradiance levels after 1000 nm, results in the p-Si module seemingly exploiting more of the received solar energy. This is observable in Figure 44. The p-Si module would not have this advantage if the spectral irradiance distribution measured on the 18.03.16 followed the same absorption pattern as the AM 1.5 spectrum. Spectral irradiance levels close to or higher than AM 1.5 levels may favor the p-Si module. Measurements conducted in February and March did not reach the levels of the AM 1.5 spectrum. It is consequently difficult to analyze the effects of the calibration error, which implies that the spectral factors presented in Figure 42 may not be accurate.

The spectroradiometer could have been sent to the producers in USA for a recalibration. Spectroradiometer has to be recalibrated after a certain period, and a recalibration would probably have

been the best way to see if the measurement error was due to improper calibration. This would on the contrary have taken too much time, and the results of this thesis might have been reduced due the absence of spectral irradiance measurements. The spectroradiometer was therefore not recalibrated.

Another possibility would be to neglect all spectral irradiance measurements after 1000 nm. This would give a better comparison between the standard and measured spectra. The main concern is that the spectral factor would be affected by excluding even more of the total spectrum. The spectral response of the CIS- and p-Si solar module are both limited at wavelengths higher than 1100 nm, and shortening the total wavelength interval even more would make the calculated spectral factor less accurate.

A key aspect of this thesis was to analyze the spectral irradiance conditions in the Nordic countries. Solar spectra have only been measured at Kjeller and Grimstad, and only in the months of February and March. Measuring spectral irradiance at several places in the Nordics over significantly longer periods would give a good base to determine the spectral irradiance conditions. This was not possible to achieve, mostly because of a short timeframe. It would still have been possible to measure the solar spectra for a more days, but other factors limited the number of measurements. Establishing a proper measuring station at Kjeller was a limiting factor. The physical specifications of the spectroradiometer limited the number days available to perform measurements.

5 Further work

The most important aspect in bringing this work further is to extend, and improve the spectrally resolved irradiation measurements in Norway. This is currently work in progress at both Kjeller and UiA. The measurement station at Kjeller is still in the startup phase, and improving the measurement site is important in order to achieve longer and more complete measurement sequences. The most important improvement would be to recalibrate the spectroradiometer. The possible calibration error affects all calculations based on spectral irradiance measurements, and the recalibration will expectantly improve the accuracy of the results presented in this thesis. Measurements performed with the PSR-1100F should also be compared to that of other spectroradiometer in order to determine any deviations. A long fiber optic should be acquired and installed in order place the spectroradiometer inside, and thereby minimizing the risk of the technical difficulties experienced in this experiment. The tripod-diffuser-setup would consequently be positioned at the same spot for longer periods, improving the overall measurement quality. Further improvements of the measuring site should involve the installation of a horizontally positioned pyranometer to measure global irradiance at Kjeller. This installment will aid in the characterization of the irradiance conditions at Kjeller and makes it possible to analyze the correlation between observable light conditions, spectral irradiance distributions and irradiance levels. It would also be interesting to analyze how the spectral irradiance distribution varies between sunrise and sunset, as measurements in this thesis were only conducted around noon. In order to characterize the irradiance conditions in Norway, global irradiance measurements for several locations in the Nordics should be analyzed and compared with the measurements from Ås. Due to little research on the spectral irradiance distribution in the Nordics, it is suggested that yearly measurements should be performed in different locations in the Nordics to observe the effects of seasonal variation, climate and latitude.

The modelling of the solar spectrum was limited due to the probable calibration error and nonexistent data concerning the aerosol- and gaseous composition of the atmosphere at Kjeller. It is therefore suggested that collaboration between the Solar Energy Department and NILU should be started with the focus of measuring the atmospheric composition of aerosols and gases at Kjeller. Another key aspect is that SMARTS only models the clear sky spectral irradiance distribution. A study should therefore be made with the focus of modeling the solar spectrum in cloudy conditions by implementing the model SEDES1 or other models.

The measurements collected in this thesis were used to analyze the effects on performance for the same type of modules that are installed on the south facing wall of the Solar Department Building. The input parameters used in the different calculations have only been extracted from datasheets or other research material. It is hence suggested that characterization measurements are performed for both modules in order to obtain accurate electrical specifications. Performance measurements at different light intensities and spectral distributions should also be conducted and compared with the calculated results.

The next step in this process would be to investigate the actual losses due to spectral effects and varying light intensities for the wall-mounted modules. For this to be achieved, additional measurements have to be performed. There are several factors that are neglected in this thesis and factors like temperature, shading, degradation and reflection are important to take into account. The additional instruments needed to perform this will consist of a vertically positioned pyranometer to measure the incoming irradiance in

the plane of the modules and an instrument measuring the ambient and module temperature. For better accuracy, this experiment will also require spectral irradiance measurements in the vertical plane. There are also a couple of trees located close to the modules that should be removed in order to decrease shading.

6 Conclusion

The effects on performance for CIS- and p-Si modules installed at Kjeller have been calculated with respect to varying irradiance levels and spectral irradiance distributions. Global irradiance measurements from the measurement station FAGKLIM at Ås and spectral irradiance measurements conducted at Kjeller and in Grimstad have been collected and analyzed in order to characterize the irradiance conditions in the Nordics. The horizontal global irradiance data consists of time-resolved solar irradiance measured between the years 2011 and 2015. Horizontal spectral irradiance measurements were performed with the use of a spectroradiometer. The measurements performed at the University of Agder in Grimstad consist of measurement sequences conducted during two days in February. An important outcome if this work has been the establishment of a new measurement site at Kjeller, at which spectral irradiance measurements were conducted for several days in March.

The comparison between measured and modelled solar spectra showed significant deviations in the long wavelength range. This deviation was due to a possible calibration error in the spectroradiometer. Uncertainties in the modelling were introduced by the lack of measurement data concerning the atmospheric composition and cloudy conditions at Kjeller. Consequently, no long term modelled solar spectra were produced. A range of atmospheric and climatic data was collected in order to establish an accurate for the spectrally resolved irradiation conditions, using the SMARTS modelling software. As of today, the model is not capable of simulating cloudy conditions and is hence not a replacement for continuous measurements. It can however be a very useful tool for comparisons with spectroradiometric measurements, to study potential deviations and the effects of atmospheric components on the spectrum. Further development of SMARTS or SEDES1 modelling could give a viable alternative to measurements.

The relative energy contribution at Ås was calculated for several irradiance levels, with the highest relative energy contribution taking place at 400-500 W/m^2, contributing with 14 % of the yearly irradiation. Irradiance levels ranging between 800-1100 W/m^2 only contributes with 4 % of the yearly irradiation. In comparison with the STC efficiency of each module the CIS and p-Si module both achieve higher efficiencies between light intensities 500-1000 W/m^2. The average efficiencies of the CIS- and p-Si module at light intensities 400-500 W/m^2 are 13.37 % and 15.88 %, respectively. The p-Si module is consequently more efficient at irradiance levels that contribute with the highest portion of the yearly solar irradiation.

The majority of the measured spectral irradiance distributions were characterized by low average photon energies. This red richness of the solar spectra was expected due to an overall high air mass. The p-Si module showed greater performance under the measured solar spectra than that of the CIS module. By further analyzing the correlation between average photon energy and the spectral factor, it is suggested that the p-Si module performs better in red rich spectra compared to the CIS module which appears to perform better in blue rich spectra.

7 References

1. Pachauri, R.K., et al., *Climate Change 2014: Synthesis Report. Contribution of Working Groups I, II and III to the Fifth Assessment Report of the Intergovernmental Panel on Climate Change.* 2014.
2. IEA, *A Snapshot of Global PV 1992-2015*. 2016.
3. Multiconsult. *Markedet for solceller*. 2016; Available from: http://www.fornybar.no/solenergi/produksjon-og-marked#sol3.1
4. IEA, *PVPS annual report 2015*. 2016.
5. Šúri, M., et al., *Potential of solar electricity generation in the European Union member states and candidate countries.* Solar Energy, 2007. **81**(10): p. 1295-1305.
6. Dupré, O., R. Vaillon, and M.A. Green, *"Physics of the temperature coefficients of solar cells".* Solar Energy Materials and Solar Cells, 2015. **140**: p. 92-100.
7. A.M. Stoneham, C.R.A.C.a.P.W.T., *Degradation of solar cells.* 1978. **2**.
8. Reich, N., et al. *Weak light performance and spectral response of different solar cell types*. in *Proc. 20th European Photovoltaic Solar Energy Conf., Barcelona, Spain*. 2005.
9. IEA, *Analysis of Long-Term Performance of PV Systems.* 2014.
10. Stamenic, L., E. Smiley, and K. Karim, *Low light conditions modelling for building integrated photovoltaic (BIPV) systems.* Solar Energy, 2004. **77**(1): p. 37-45.
11. Nakada, Y., et al., *Influence of clearness index and air mass on sunlight and outdoor performance of photovoltaic modules.* Current Applied Physics, 2010. **10**(2): p. S261-S264.
12. Aguado, E. and J.E. Burt, *Understanding weather and climate*. 5. ed. 2010, New York u.a.: Prentice Hall. XX, 586 S.
13. NASA. *Solar radiation*. 2016.
14. Standard, A., *G173-03.* Standard tables for reference solar spectral irradiances: direct normal and hemispherical on, 2008. **37**.

15. NASA. *The Atmosphere's Energy Budget*. 2009; Available from: http://earthobservatory.nasa.gov/Features/EnergyBalance/page6.php.

16. *How Does Weather Work?* 2016; Available from: http://www.barometricpressureheadache.com/how-does-weather-work/.

17. Nofuentes, G., et al., *Solar spectral and module temperature influence on the outdoor performance of thin film PV modules deployed on a sunny inland site.* International Journal of Photoenergy, 2013. **2013**.

18. Nann, S. and C. Riordan, *Solar spectral irradiance under clear and cloudy skies: Measurements and a semiempirical model.* Journal of Applied Meteorology, 1991. **30**(4): p. 447-462.

19. Nann, S. and C. Riordan. *Solar spectral irradiance under overcast skies [solar cell performance effects]*. in *Photovoltaic Specialists Conference, 1990., Conference Record of the Twenty First IEEE*. 1990. IEEE.

20. Muneer, T. and F. Fairooz, *Quality control of solar radiation and sunshine measurements–lessons learnt from processing worldwide databases.* Building Services Engineering Research and Technology, 2002. **23**(3): p. 151-166.

21. Ø. Byrkjedal, A.L., S. Lileo, *Resource mapping of solar energy.* 2013.

22. William E. Schneider, R.Y., *Spectroradiometry Methods.* 1998.

23. Huld, T., R. Müller, and A. Gambardella, *A new solar radiation database for estimating PV performance in Europe and Africa.* Solar Energy, 2012. **86**(6): p. 1803-1815.

24. Mertens, K., *Photovoltaics: Fundamentals, Technology and Practice*. 2013: John Wiley & Sons.

25. *Quantum efficiency*. 2013; Available from: http://pveducation.org/pvcdrom/solar-cell-operation/quantum-efficiency.

26. *Spectral response*. 2013; Available from: http://www.pveducation.org/pvcdrom/characterisation/spectral-response.

27. Zdanowicz, T., T. Rodziewicz, and M.Z. Waclawek. *Effect of air mass factor on the performance of different type of PV modules*. in *Photovoltaic Energy Conversion, 2003. Proceedings of 3rd World Conference on*. 2003. IEEE.

28. Reich, N., et al., *Crystalline silicon cell performance at low light intensities.* Solar Energy Materials and Solar Cells, 2009. **93**(9): p. 1471-1481.

29. McMahon, T., T. Basso, and S. Rummel. *Cell shunt resistance and photovoltaic module performance*. in *Photovoltaic Specialists Conference, 1996., Conference Record of the Twenty Fifth IEEE*. 1996. IEEE.

30. Randall, J. and J. Jacot, *Is AM1. 5 applicable in practice? Modelling eight photovoltaic materials with respect to light intensity and two spectra.* Renewable Energy, 2003. **28**(12): p. 1851-1864.

31. Janke, S., et al. *Technology Comparison of Different Types of Solar Cells and Modules regarding Weak Light and Yield Performance*. in *Proc. of the 28th European Photovoltaic Solar Energy Conference*. 2013.

32. Bücher, K., *Site dependence of the energy collection of PV modules.* Solar Energy Materials and Solar Cells, 1997. **47**(1): p. 85-94.

33. Evolution, S.; Available from: http://spectralevolution.com/lightweight_portable_battery_operated_spectrometer.html.

34. Norgeskart. *Location of measurement site at Kjeller*. Available from: https://www.norgeskart.no/#4/165940/6868945/-land/+terreng.

35. Norgeskart, *Location of measurement site in Grimstad.*

36. Imenes, A., et al. *Development of a test station for accurate in situ IV curve measurements of photovoltaic modules in southern Norway*. in *Photovoltaic Specialists Conference (PVSC), 2011 37th IEEE*. 2011. IEEE.

37. Norgeskart. *Location of measurement site at Ås*. 2016; Available from: https://www.norgeskart.no/?sok=Ås#4/295665/6894410/-land/+terreng/+hits.

38. NMBU. *Om FAGKLIM*. 2015; Available from: https://www.nmbu.no/om/fakulteter/miljotek/institutter/imt/laboratorier/fagklim/om-fagklim.

39. NMBU. *Stråling og energi*. 2014; Available from: https://www.nmbu.no/om/fakulteter/miljotek/institutter/imt/laboratorier/fagklim/maleinstrumenter/straling#GLOB.

40. Wolff Mareile, Thue-Hansen V. and Grimenes A.A., *Meteorologiske data for Ås.* NORGES MILJØ OG BIOVITENSKAPLIGE UNIVERSITET.

41. Gueymard, C.A., *Parameterized transmittance model for direct beam and circumsolar spectral irradiance.* Solar Energy, 2001. **71**(5): p. 325-346.

42. Myers, D.R., *Solar radiation: practical modeling for renewable energy applications*. 2013: CRC Press.

43. Myers, D.R. and C.A. Gueymard. *Description and availability of the SMARTS spectral model for photovoltaic applications*. in *Optical Science and Technology, the SPIE 49th Annual Meeting*. 2004. International Society for Optics and Photonics.

44. Berk, A., et al. *MODTRAN 5: a reformulated atmospheric band model with auxiliary species and practical multiple scattering options: update*. in *Defense and Security*. 2005. International Society for Optics and Photonics.

45. Gueymard, C., *SMARTS2: a simple model of the atmospheric radiative transfer of sunshine: algorithms and performance assessment*. 1995: Florida Solar Energy Center Cocoa, FL.

46. *SMARTS User Interface Manual.* 2008.

47. The MathWorks Inc., N., MA,, *MATLAB R2014b.* 2014.

48. FSF, *Plot Digitizer.* 2015.

49. PVsyst.

50. Haug, H., et al., *PC1Dmod 6.1–state-of-the-art models in a well-known interface for improved simulation of Si solar cells.* Solar Energy Materials and Solar Cells, 2015. **142**: p. 47-53.

51. Huld, T., et al., *Mapping the performance of PV modules, effects of module type and data averaging.* Solar Energy, 2010. **84**(2): p. 324-338.

52. Svendby, T.M., et al., *Monitoring of the atmospheric ozone layer and natural ultraviolet radiation: Annual report 2014.* 2015.

53. Myhre, C.L., et al., *Monitoring of greenhouse gases and aerosols at Svalbard and Birkenes in 2014-Annual report.* 2016.

54. Green, M.A., et al., *Solar cell efficiency tables (Version 47).* 2015. **24**(1): p. 3-11.

55. Kenny, R.P., et al., *Performance of thin film PV modules.* Thin solid films, 2006. **511**: p. 663-672.

56. Ishii, T., et al., *A simplified methodology for estimating solar spectral influence on photovoltaic energy yield using average photon energy.* Energy Science & Engineering, 2013. **1**(1): p. 18-26.

57. Parretta, A., A. Sarno, and L.R. Vicari, *Effects of solar irradiation conditions on the outdoor performance of photovoltaic modules.* Optics Communications, 1998. **153**(1): p. 153-163.

58. Sokolik, I., *Absorption by atmospheric gases in the IR, visible and UV spectral regions* 2009.

Appendix A

Electrical- and mechanical specifications for the p-Si- and CIS module.

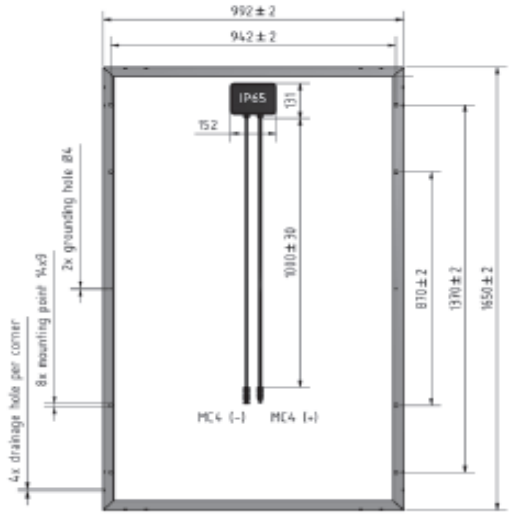

Progression of the power warranty

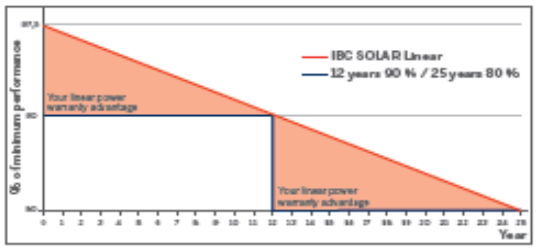

TECHNICAL DATA

IBC PolySol	250 CS	255 CS	260 CS
STC Power Pmax (Wp)	250	255	260
STC Nominal Voltage Umpp (V)	30.4	30.9	31.1
STC Nominal Current Impp (A)	8.23	8.25	8.37
STC Open circuit voltage Uoc (V)	37.6	37.8	38.1
STC Short circuit current Isc (A)	8.81	8.83	8.98
800W/m² NOCT AM 1.5 Power Pmax (Wp)	183.07	186.77	190.64
800W/m² NOCT AM 1.5 Nominal Voltage Umpp (V)	27.78	27.96	28.16
800W/m² NOCT AM 1.5 Open Circuit Voltage Uoc (V)	35.05	35.57	36.04
800W/m² NOCT AM 1.5 Short Circuit Current Isc (A)	6.92	6.96	7.00
Rel. efficiency reduction @ 200 W/m² (%)	3.9	4.23	4.29
Tempcoeff Isc (%/°C)	+0.064	+0.064	+0.064
Tempcoeff Uoc (mV/°C)	−117.7	−120.7	−121.7
Tempcoeff Pmpp (%/°C)	−0.43	−0.43	−0.43
Module Efficiency (%)	15.3	15.6	15.9
NOCT (°C)	48	48	48
Max. System Voltage (V)	1000	1000	1000
Max. Reverse Current Ir (A)	20	20	20
Current value String fuse (A)	15	15	15
Fuse protection from parallel strings	4	4	4
Height (mm)	45	45	45
Weight (kg)	20.5	20.5	20.5
Article number	2203800007	2203800005	2203800006 2203800008

2014-08-01

Figure 45: Electrical- and mechanical specifications for the IBC PolySol 260 CS.

Mechanical Characteristics

Dimensions (L x W x H)*3	1,257 x 977 x 35 mm (49.5 x 38.5 x 1.4 inch)
Weight	20 kg (44.1 lbs)
Module operating temperature	-40 °C to 85 °C
Application class on IEC61730	Class A
Fire safety class on IEC61730	Class C
Safety class on IEC61140	II
Snow load (to the front of the module)*4	2,400 Pa (IEC61646) / 1,600 Pa design load (UL1703)
Wind load (to the back of the module)	2,400 Pa (IEC61646) / 1,600 Pa design load (UL1703)
Cell type	CIS substrate glass (cadmium free)
Front cover	Clear tempered glass, 3.2 mm
Encapsulant	EVA
Back sheet	Weatherproof plastic film (color: black & silver)
Frame	Anodized aluminum alloy (color: black)
Edge sealant	Butyl rubber
Junction box	Protection rating: IP67 (with bypass diode)
Adhesive	Silicone
Output cables (Conductor)	2.5 mm^2 / AWG14 (halogen free)
Cable lengths (symmetrical)	1,200 mm (47.2 inch)
Connectors	MC4 compatible

Electrical Characteristics

Electrical Performance at Standard Test Conditions (STC)*1

		SF165-S
Nominal Power	Pmax	165 W
Power tolerance		+5 W / 0 W
Open circuit voltage	Voc	110.0 V
Short circuit current	Isc	2.20 A
Voltage at nominal power	Vmpp	85.5 V
Current at nominal power	Impp	1.93 A

Figure 46: Electrical- and mechanical specifications for SF165-S.

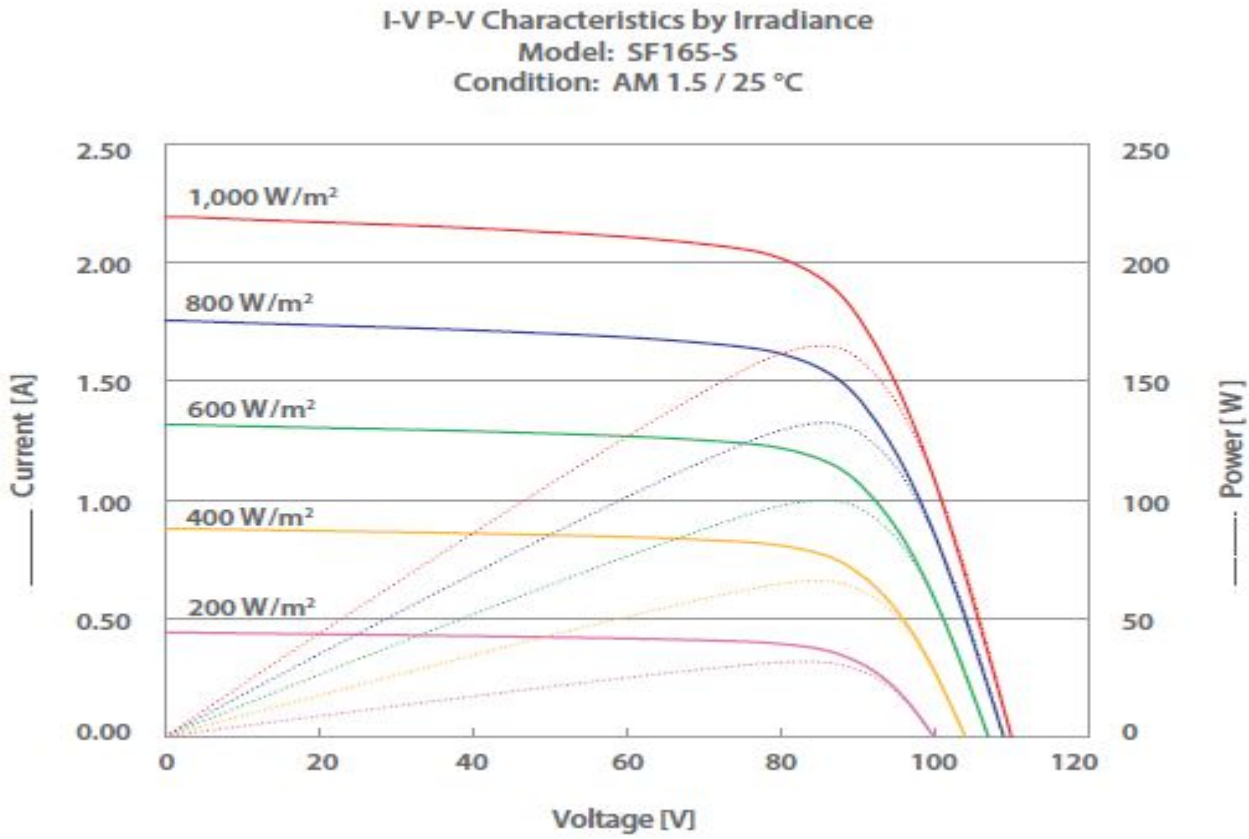

Figure 47: Performance of the SF165-S at different light intensities.

Appendix B

Gaseous absorption in the atmosphere

Table 4: Gaseous absorption in the ultraviolet- and visible spectrum [58].

Gas	Absorption wavelengths (μm)
N_2	< 0.1
O_2	< 0.245
O_3	0.17-0.35 0.45-0.75
H_2O	< 0.21 0.6-0.72
H_2O_2 hydrogen peroxide	< 0.35
NO_2 nitrogen oxide	< 0.6*
N_2O	< 0.24
NO_3 nitrate radical	0.41-0.67
HONO nitrous acid	< 0.4
HNO_3 nitric acid	< 0.33
CH_3Br methyl bromide	< 0.26
$CFCl_3$ (CFC11)	< 0.23
HCHO formaldehyde	0.25-0.36

Table 5: Gaseous absorption in the visible and near infrared spectrum [58].

Gas	Center ν (cm^{-1}) ($\lambda(\mu m)$)	Band interval (cm^{-1})
H_2O	3703 (2.7)	2500-4500
	5348 (1.87)	4800-6200
	7246 (1.38)	6400-7600
	9090 (1.1)	8200-9400
	10638 (0.94)	10100-11300
	12195 (0.82)	11700-12700
	13888 (0.72)	13400-14600
	visible	15000-22600
CO_2	2526 (4.3)	2000-2400
	3703 (2.7)	3400-3850
	5000 (2.0)	4700-5200
	6250 (1.6)	6100-6450
	7143 (1.4)	6850-7000
O_3	2110 (4.74)	2000-2300
	3030 (3.3)	3000-3100
	visible	10600-22600
O_2	6329 (1.58)	6300-6350
	7874 (1.27)	7700-8050
	9433 (1.06)	9350-9400
	13158 (0.76)	12850-13200
	14493 (0.69)	14300-14600
	15873 (0.63)	14750-15900
N_2O	2222 (4.5)	2100-2300
	2463 (4.06)	2100-2800
	3484 (2.87)	3300-3500
CH_4	3030 (3.3)	2500-3200
	4420 (2.20)	4000-4600
	6005 (1.66)	5850-6100
CO	2141 (4.67)	2000-2300
	4273 (2.34)	4150-4350
NO_2	visible	14400-50000

Appendix C

Output files from DARWin SP

```
Comment:
Version: 2.2
File Name: C:\Users\tobiasab\Google Drive\MATLAB\Spectral irradiance
Instrument: PSR-1100_SN1544447
Detectors: 512,0,0
Measurement: DIRECT_ENERGY
Date: 03/16/2016,03/16/2016
Time: 10:29:21.36,10:30:11.87
Temperature (C): 20.01,20.42
Battery Voltage: 8.41,8.41
Averages: 10,10
Integration: 17,17
Dark Mode: AUTO,AUTO
Foreoptic: InLine {IRRADIANCE}, InLine {IRRADIANCE}
Radiometric Calibration: IRRADIANCE
Units: W/m^2/nm
Wavelength Range: 320,1100
Latitude: n/a
Longitude: n/a
Altitude: n/a
GPS Time: n/a
Satellites: n/a
Calibrated Reference Correction File: none
Channels: 781
Columns [2]:
Data:
Wvl      Irrad. (Target)
 320.0    2.662898E-002
 321.0    3.154916E-002
 322.0    3.633004E-002
 323.0    3.854565E-002
 324.0    3.878760E-002
 325.0    4.859396E-002
 326.0    5.632689E-002
 327.0    5.981470E-002
 328.0    5.856757E-002
 329.0    6.929808E-002
 330.0    8.675938E-002
 331.0    1.030086E-001
 332.0    8.932865E-002
 333.0    8.457310E-002
 334.0    9.109535E-002
 335.0    1.015424E-001
 336.0    1.072810E-001
 337.0    1.079734E-001
 338.0    1.037927E-001
 339.0    1.119070E-001
 340.0    1.184731E-001
 341.0    1.189917E-001
 342.0    1.129480E-001
 343.0    1.135024E-001
 344.0    1.166091E-001
 345.0    1.159035E-001
 346.0    1.326330E-001
 347.0    1.414477E-001
 348.0    1.337523E-001
 349.0    1.475163E-001
 350.0    1.634678E-001
 351.0    1.751005E-001
 352.0    1.755110E-001
 353.0    1.667897E-001
 354.0    1.594757E-001
 355.0    1.676278E-001
 356.0    1.566763E-001
 357.0    1.437578E-001
 358.0    1.393831E-001
 359.0    1.495070E-001
 360.0    1.608466E-001
 361.0    1.680192E-001
 362.0    1.661545E-001
 363.0    1.746654E-001
 364.0    1.886118E-001
```

Figure 48: Example of an SED output file from DARWin SP, showing a portion of the measurement data and other relevant data.

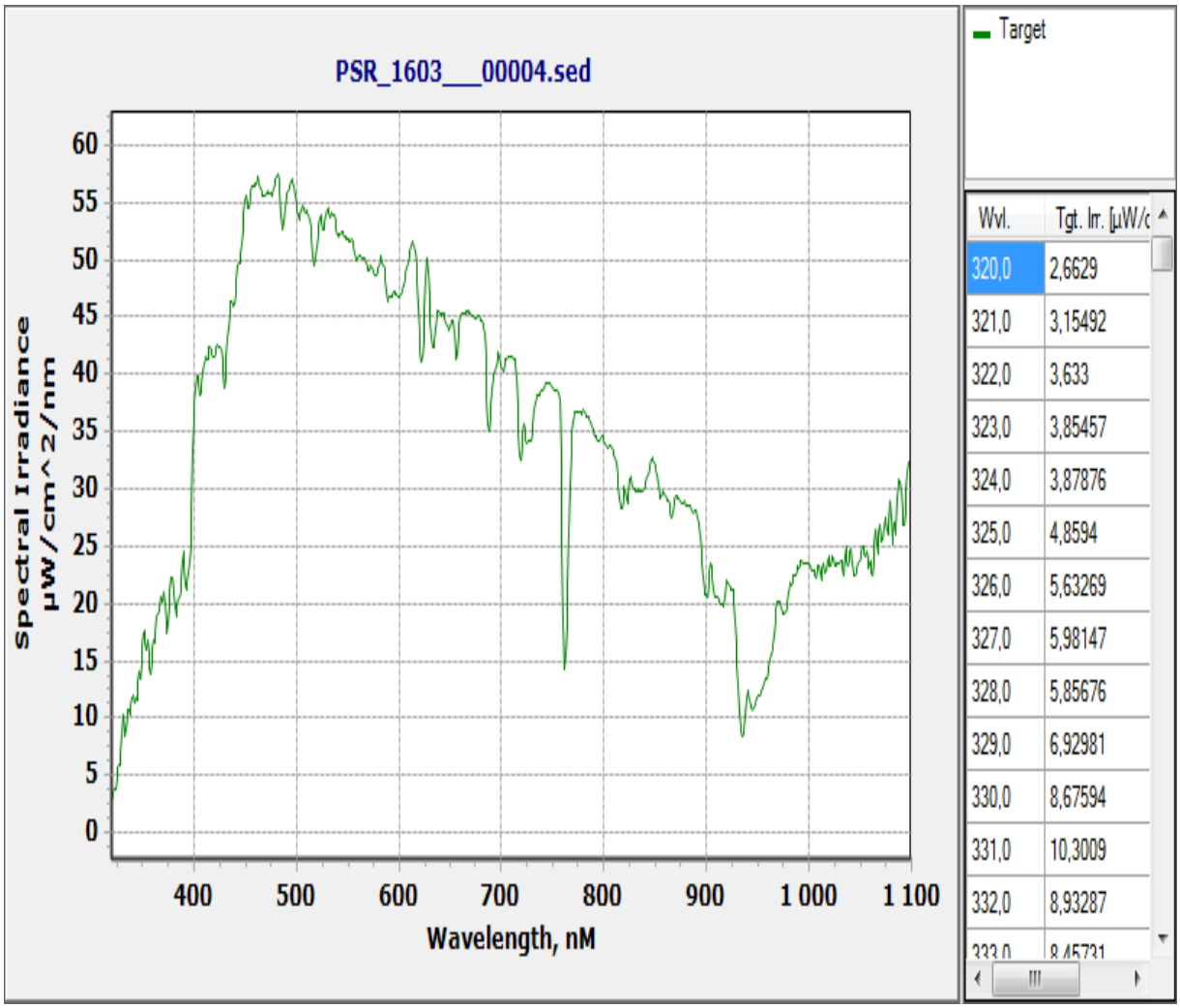

Figure 49: Example of a RAW output file from DARWin SP, which shows the plotted values of the SED output file.

Appendix D

Input and output files from SMARTS

```
'Kjeller 16.03 kl 13:17'
1
1019.2 0.108 0
0
3.3 82 'Summer' 3.3
2
0
1 0.35
1
400
0
'S&F_RURAL'
1
0.68
28
0
300 1200 1 1366
2
300 1200 1
1
4
0
1
0 320 1100 1 3
0
0
1
27.75 0
```

Figure 50: SMARTS input file. Each number or text string defines each parameter card.

```
******************   SMARTS, version 2.9.5   *******************

 Simple Model of the Atmospheric Radiative Transfer of Sunshine
      Chris A. Gueymard, Solar Consulting Services
                  December 2005

    This model is documented in FSEC Report PF-270-95
 and in a Solar Energy paper, vol. 71, No.5, 325-346 (2001)

 NOTE: These references describe v. 2.8 or earlier!!!
 See the User's Manual for details on the considerable
 changes that followed...

*********************************************************************

   Reference for this run: Kjeller 16.03 kl 13:17

---------------------------------------------------------------------

* ATMOSPHERE : USER         AEROSOL TYPE: S&F_RURAL

* INPUTS:
     Pressure (mb) = 1019.200   Ground Altitude (km) =   0.1080
     Height above ground (km) =   0.0000
     Relative Humidity (%) = 82.000   Precipitable Water (cm) =  1.1156
     Ozone (atm-cm) = 0.3500 or 350.0 Dobson Units
   AEROSOLS:  Optical Depth at 500 nm = 1.6567      Optical depth at 550 nm = 1.4688
      Angstrom's Beta = 0.6900       Schuepp's B = 0.7195
     Meteorological Range (km) =    3.8   Visibility (km) =    2.9
     Alpha1 = 0.8881  Alpha2 = 1.2637   Mean Angstrom's Alpha = 1.0759
     Season = SPRING/SUMMER

* TEMPERATURES:
     Instantaneous at site's altitude = 276.4 K
     Daily average (reference) at site's altitude = 276.4 K
     Stratospheric Ozone and NO2 (effective) = 224.7 K


The following spectral variables will be output to file: kjeller1603_ang069_oz035

 * Global_horizn_irradiance


      Spectral ZONAL albedo data: FINE_SNOW
      with a reflection process: NON_LAMBERTIAN          |


=====================================================================================================
=====================================================================================================

* SOLAR POSITION (deg.):
    Zenith Angle (apparent) = 62.250  Azimuth (from North) =    0.00

      RELATIVE OPTICAL MASSES:
  - Rayleigh =  2.141
  - Water Vapor =  2.147
  - Ozone =  2.132
  - NO2 =  2.136
  - Aerosols =  2.146


 CO2 Mixing Ratio (ppmv):  400.0


 Total column abundances (atm-cm) for all gases except H2O, and for normal/standard conditions:

    BrO        CH2O        CH4       ClNO3          CO         CO2        HNO2        HNO3         NH3

0.2500E-05 0.3000E-03 0.1485E+01 0.1200E-03 0.8957E-01 0.3230E+03 0.1000E-03 0.3674E-03 0.1779E-03


     NO         NO2         NO3          N2         N2O          O2          O3          O4         SO2

0.3170E-03 0.2068E-03 0.5000E-04 0.3848E+06 0.2451E+00 0.1688E+06 0.3500E+00 0.1688E+06 0.1118E-03



*  *  *  *  *  *  *  *  *  *  *  *  *  *  *  *  *  *  *  *  *  *  *  *  *  *  *  *  *  *  *  *  *

** SPECTRUM:
   Total (0-100 µm) Extraterrestrial Irradiance used here = 1366.00 W/m2
  (i.e., 1.0000 times the selected solar constant, 1366.00 W/m2, due to the actual Sun-Earth distance.)
   Source for selected solar spectrum: Gueymard_2003


Wavelength Range =  300.0 to 1200.0 nm;  Number of Wavelengths =  1002

*** BROADBAND IRRADIANCES (W/m2):

* DIRECT BEAM AT NORMAL INCIDENCE:
  Extraterrestrial = 1057.75   Terrestrial =   81.08   Atmospheric Transmittance = 0.0767

* FOR THE HORIZONTAL PLANE:
  Direct Beam =   37.75   Diffuse = 268.76   Global =  306.51   Clearness index, KT = 0.2244
  Diffuse irradiance origination details:
   Sky diffuse = 205.80   Back-scattered diffuse =  62.95
```

Figure 51: SMARTS output file, showing both specific input value and specific output data.

SMOOTHED RESULTS TO SIMULATE A 3.00 nm FWHM INSTRUMENT AND A WAVELENGTH STEP OF 1.0 nm,
Shape selected: Triangular

WVLGTH	ET_SPCTRUM	BEAM_NORMAL	BEAM_NORM+	GLOB_HORIZ	GLOBL_TILT
320.0	0.7608E+00	0.3474E-03	0.3474E-03	0.1097E+00	0.1097E+00
321.0	0.7530E+00	0.3783E-03	0.3783E-03	0.1171E+00	0.1171E+00
322.0	0.7417E+00	0.4065E-03	0.4065E-03	0.1228E+00	0.1228E+00
323.0	0.7359E+00	0.4420E-03	0.4420E-03	0.1302E+00	0.1302E+00
324.0	0.7850E+00	0.5140E-03	0.5140E-03	0.1474E+00	0.1474E+00
325.0	0.8585E+00	0.6041E-03	0.6041E-03	0.1684E+00	0.1684E+00
326.0	0.9362E+00	0.7003E-03	0.7003E-03	0.1903E+00	0.1903E+00
327.0	0.9772E+00	0.7745E-03	0.7745E-03	0.2047E+00	0.2047E+00
328.0	0.1004E+01	0.8430E-03	0.8430E-03	0.2165E+00	0.2165E+00
329.0	0.1021E+01	0.9076E-03	0.9076E-03	0.2263E+00	0.2263E+00
330.0	0.1034E+01	0.9639E-03	0.9639E-03	0.2334E+00	0.2334E+00
331.0	0.1018E+01	0.9929E-03	0.9929E-03	0.2336E+00	0.2336E+00
332.0	0.9942E+00	0.1016E-02	0.1016E-02	0.2319E+00	0.2319E+00
333.0	0.9759E+00	0.1046E-02	0.1046E-02	0.2320E+00	0.2320E+00
334.0	0.9631E+00	0.1079E-02	0.1079E-02	0.2339E+00	0.2339E+00
335.0	0.9401E+00	0.1097E-02	0.1097E-02	0.2325E+00	0.2325E+00
336.0	0.9068E+00	0.1100E-02	0.1100E-02	0.2271E+00	0.2271E+00
337.0	0.8964E+00	0.1130E-02	0.1130E-02	0.2258E+00	0.2258E+00
338.0	0.9239E+00	0.1210E-02	0.1210E-02	0.2341E+00	0.2341E+00
339.0	0.9637E+00	0.1309E-02	0.1309E-02	0.2464E+00	0.2464E+00
340.0	0.9945E+00	0.1399E-02	0.1399E-02	0.2559E+00	0.2559E+00
341.0	0.9999E+00	0.1457E-02	0.1457E-02	0.2586E+00	0.2586E+00
342.0	0.9869E+00	0.1485E-02	0.1485E-02	0.2558E+00	0.2558E+00
343.0	0.9645E+00	0.1499E-02	0.1499E-02	0.2513E+00	0.2513E+00
344.0	0.9307E+00	0.1492E-02	0.1492E-02	0.2432E+00	0.2432E+00
345.0	0.9284E+00	0.1540E-02	0.1540E-02	0.2437E+00	0.2437E+00
346.0	0.9314E+00	0.1598E-02	0.1598E-02	0.2451E+00	0.2451E+00
347.0	0.9438E+00	0.1670E-02	0.1670E-02	0.2490E+00	0.2490E+00
348.0	0.9469E+00	0.1729E-02	0.1729E-02	0.2495E+00	0.2495E+00
349.0	0.9631E+00	0.1813E-02	0.1813E-02	0.2527E+00	0.2527E+00
350.0	0.9908E+00	0.1920E-02	0.1920E-02	0.2581E+00	0.2581E+00
351.0	0.1006E+01	0.2002E-02	0.2002E-02	0.2606E+00	0.2606E+00
352.0	0.1020E+01	0.2088E-02	0.2088E-02	0.2634E+00	0.2634E+00
353.0	0.1042E+01	0.2196E-02	0.2196E-02	0.2688E+00	0.2688E+00
354.0	0.1074E+01	0.2324E-02	0.2324E-02	0.2766E+00	0.2766E+00
355.0	0.1062E+01	0.2355E-02	0.2355E-02	0.2735E+00	0.2735E+00
356.0	0.9930E+00	0.2257E-02	0.2257E-02	0.2559E+00	0.2559E+00
357.0	0.9032E+00	0.2107E-02	0.2107E-02	0.2327E+00	0.2327E+00
358.0	0.8752E+00	0.2102E-02	0.2102E-02	0.2253E+00	0.2253E+00
359.0	0.9048E+00	0.2231E-02	0.2231E-02	0.2327E+00	0.2327E+00
360.0	0.9614E+00	0.2428E-02	0.2428E-02	0.2474E+00	0.2474E+00
361.0	0.9830E+00	0.2547E-02	0.2547E-02	0.2535E+00	0.2535E+00
362.0	0.1006E+01	0.2681E-02	0.2681E-02	0.2604E+00	0.2604E+00
363.0	0.1032E+01	0.2831E-02	0.2831E-02	0.2682E+00	0.2682E+00
364.0	0.1092E+01	0.3077E-02	0.3077E-02	0.2847E+00	0.2847E+00
365.0	0.1152E+01	0.3331E-02	0.3331E-02	0.3011E+00	0.3011E+00
366.0	0.1208E+01	0.3576E-02	0.3576E-02	0.3162E+00	0.3162E+00
367.0	0.1224E+01	0.3707E-02	0.3707E-02	0.3207E+00	0.3207E+00
368.0	0.1224E+01	0.3793E-02	0.3793E-02	0.3209E+00	0.3209E+00
369.0	0.1218E+01	0.3869E-02	0.3869E-02	0.3198E+00	0.3198E+00
370.0	0.1212E+01	0.3941E-02	0.3941E-02	0.3187E+00	0.3187E+00
371.0	0.1177E+01	0.3914E-02	0.3914E-02	0.3101E+00	0.3101E+00

Figure 52: SMARTS output file showing spectral irradiance data for a every wavelength.

Appendix E

PSR-1100F spectroradiometer specifications

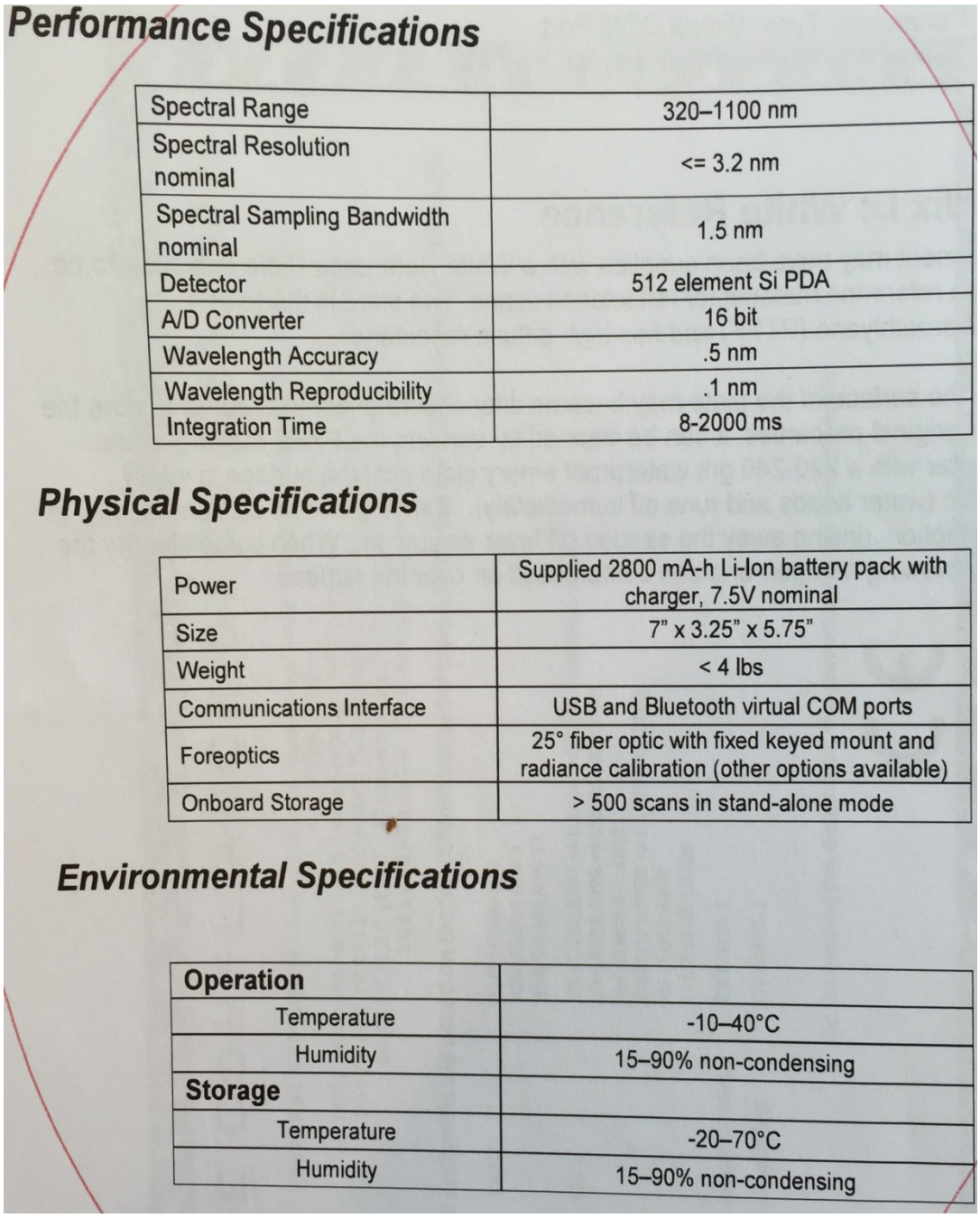

Performance Specifications

Spectral Range	320–1100 nm
Spectral Resolution nominal	<= 3.2 nm
Spectral Sampling Bandwidth nominal	1.5 nm
Detector	512 element Si PDA
A/D Converter	16 bit
Wavelength Accuracy	.5 nm
Wavelength Reproducibility	.1 nm
Integration Time	8-2000 ms

Physical Specifications

Power	Supplied 2800 mA-h Li-Ion battery pack with charger, 7.5V nominal
Size	7" x 3.25" x 5.75"
Weight	< 4 lbs
Communications Interface	USB and Bluetooth virtual COM ports
Foreoptics	25° fiber optic with fixed keyed mount and radiance calibration (other options available)
Onboard Storage	> 500 scans in stand-alone mode

Environmental Specifications

Operation	
Temperature	-10–40°C
Humidity	15–90% non-condensing
Storage	
Temperature	-20–70°C
Humidity	15–90% non-condensing

Figure 53: Performance-, physical- and environmental specifications of the PSR-1100F.

Norges miljø- og biovitenskapelig universitet
Noregs miljø- og biovitskapelege universitet
Norwegian University of Life Sciences

Postboks 5003
NO-1432 Ås
Norway